



The Effect of Experimental and Modeling Parameters on Combined
EEG/MEG Source Analysis and Transcranial Electric Stimulation
Optimization of Somatosensory and Epilepsy Activity

Dissertation



Marios Antonakakis

April 2021



**The Effect of Experimental and Modeling Parameters on
Combined EEG/MEG Source Analysis and Transcranial Electric
Stimulation Optimization of Somatosensory and Epilepsy Activity**

Dissertation
Zur Erlangung des akademischen Grades
Doktor-Ingenieur (Dr.-Ing.)

vorgelegt der Fakultät für Informatik und Automatisierung
Technische Universität Ilmenau

von: Marios Antonakakis
geboren am: 10.11.1990 in Heraklion, Crete, Greece

Gutachter:

1. Univ. Prof. Dr.-Ing. habil. Jens Haueisen
2. Prof. Dr. rer. nat. Carsten Hermann Wolters (Betreuer/Doktorvater)
3. Univ. Prof. Dr. Michalis Zervakis

Tag der Einreichung: 14/10/2020

Tag der wissenschaftlichen Aussprache: 07/04/2021

Abstract

In this thesis, new experimental and modeling parameters are introduced to investigate effects on combined electroencephalography (EEG) and magnetoencephalography (MEG) source analysis and transcranial electric stimulation (TES) optimization of somatosensory evoked and epileptic activity. A pipeline is described for the combination of the complementary content of EEG and MEG in source analysis. Simultaneous data are measured, including (1) somatosensory evoked potentials (SEP) and fields (SEF) elicited by different stimulation types for group-based sensitivity investigations and (2) spontaneous EEG and MEG measures for presurgical epilepsy diagnosis. Detailed and individualized finite element head volume conductor models are used in the solution of the forward problem of source analysis. For this purpose, a quasi-automatic image processing procedure is introduced, combining T1-weighted and T2-weighted MRIs for the construction of skin, skull compacta, skull spongiosa, cerebrospinal fluid, gray and white matter tissue compartments. In this procedure, the cranial burr holes and skull thickness are also calculated. For realistic modeling of the conductive properties of brain (e.g. white matter pathways), diffusion tensor imaging is used. Skull conductivity parameter is individually calibrated due to its high inter-subject variability and its significant influence on the sensitivity of EEG and MEG source reconstructions. For calibration, a comprehensive set of skull conductivities and SEP/SEF data based on electric-wrist stimulation are used. In this work, it is presented how a combination of different stimulation types, head models and measurement modalities (EEG, MEG or combined EEG/MEG – EMEG) influence the source reconstruction of SEP/SEF response at 20 ms post-stimulus (P20/N20) and the targeting in multi-channel TES optimization. Inter-subject variability of skull conductivity and thickness over age are investigated non-invasively. Finally, EMEG source analysis with realistic head models that include skull burr holes are evaluated for the presurgical diagnosis of a drug-resistant epilepsy patient. Optimized TES with head models of different detail is investigated as an alternative of surgery to suppress epileptic seizures.

Results show that MEG stabilizes the P20/N20 location and EEG contributes to the determination of the source orientation. The complementarity of both modalities in EMEG can be utilized on the basis of detailed and individualized head models. Subsequently, optimized TES electrode montages are reported to be mainly affected by the P20/N20 orientation component of different stimulation types. For head modeling, it is presented that the inter-subject variability of conductivity and thickness of skull is large and it should be taken into account in source analysis and TES. In this regard, subjects' age and skull thickness are significantly related to the skull conductivity. For presurgical epilepsy evaluation, EMEG source analysis with calibrated and anisotropic head models indicates a focal cortical dysplasia (FCD) at the very onset of the epileptic spike peak. Simplified head models, use of single modality or time points close to the spike peak cause non-negligible

influences on the determination of the FCD. Finally, changes on the head modeling reflect considerable influences on the optimized TES and the flow of the injected direct currents towards the FCD.

The pipeline proposed in this work is combined with pattern recognition approaches in a two-phase manner for single EEG/MEG or combined EMEG source reconstruction of epileptic activity. The results indicate that EMEG source reconstructions with clustered epileptic activity are located in the vicinity of two FCDs.

Zusammenfassung

In dieser Arbeit werden neue experimentelle und Modellierungsparameter vorgestellt, um die Auswirkungen auf die kombinierte Elektroenzephalographie (EEG) und Magnetoenzephalographie (MEG)-Quellenanalyse und die Optimierung der somatosensorisch evozierten und epileptischen Aktivität durch transkranielle elektrische Stimulation (TES) zu untersuchen. Für die Kombination der komplementären Inhalte von EEG und MEG in der Quellenanalyse wird eine Pipeline beschrieben. Es werden simultane Daten gemessen, darunter (1) somatosensorisch evozierte Potentiale (SEP) und Felder (SEF), die durch verschiedene Stimulationstypen für gruppenbasierte Sensitivitätsuntersuchungen evoziert werden, und (2) Spontan-EEG- und MEG-Messungen für die prächirurgische Epilepsiediagnose. Detaillierte und individualisierte Finite-Elemente-Kopf-Volumenleiter-Modelle werden bei der Lösung des Vorwärtsproblems der Quellenanalyse verwendet. Zu diesem Zweck wird ein quasi-automatisches Bildverarbeitungsverfahren eingeführt, das T1- und T2-gewichtete MRIs für die Konstruktion von Haut, Schädelkompakta, Schädelpongiosa, Liquor, Gewebekompartimenten der grauen und weißen Substanz kombiniert. Bei diesem Verfahren werden auch die kranialen Fräslöcher und die Schädelstärke berechnet. Für die realistische Modellierung der leitfähigen Eigenschaften des Gehirns (z.B. Wege der weißen Substanz) wird die Diffusions-Tensor-Bildgebung verwendet. Der Leitfähigkeitsparameter des Schädels wird aufgrund seiner hohen Variabilität zwischen den Subjekten und seines signifikanten Einflusses auf die Empfindlichkeit von EEG- und MEG-Quellenrekonstruktionen individuell kalibriert. Zur Kalibrierung wird ein umfassender Satz von Schädelleitfähigkeiten und SEP/SEF-Daten verwendet, die auf der Stimulation des elektrischen Handgelenks basieren. In dieser Arbeit wird dargestellt, wie eine Kombination verschiedener Stimulationsarten, Kopfmodelle und Messmodalitäten (EEG, MEG oder kombiniertes EEG/MEG – EMEG) die Quellenrekonstruktion der SEP/SEF-Antwort bei 20 ms nach dem Stimulus (P20/N20) und das Targeting bei der Mehrkanal-TES-Optimierung beeinflussen. Die Inter-Subjekt-Variabilität der Schädelleitfähigkeit und -stärke über das Alter wird nicht-invasiv untersucht. Schließlich werden EMEG-Quellenanalysen mit realistischen Kopfmodellen, die Schädelbohrungen enthalten, für die präoperative Diagnose eines Patienten mit medikamentenresistenter Epilepsie ausgewertet. Optimierte TES mit unterschiedlich detaillierten Kopfmodellen wird als Alternative zur Operation zur Unterdrückung epileptischer Anfälle untersucht.

Die Ergebnisse zeigen, dass das MEG die P20/N20-Lage stabilisiert und das EEG zur Bestimmung der Quellorientierung beiträgt. Die Komplementarität beider Modalitäten im EMEG kann auf der Grundlage detaillierter und individualisierter Kopfmodelle genutzt werden. In der Folge wird berichtet, dass optimierte TES-Elektrodenmontagen hauptsächlich durch die P20/N20-Orientierungskomponente verschiedener Stimulationstypen beeinflusst werden. Für diese Modelle wird dargestellt, dass die Variabilität der Leitfähigkeit und Stärke des Schädels zwischen den Subjekten gross ist und bei der Quellenanalyse und TES

berücksichtigt werden sollte. In diesem Zusammenhang sind das Alter und die Schädelstärke der Probanden signifikant mit der Schädelleitfähigkeit verbunden. Für die prächirurgische Epilepsie-Evaluation zeigt die EMEG-Quellenanalyse mit kalibrierten und anisotropen Kopfmodellen eine fokale kortikale Dysplasie (FCD) genau zu Beginn des epileptischen Spike-Peaks an. Vereinfachte Kopfmodelle, die Verwendung einer einzigen Modalität oder Zeitpunkte nahe dem Spike-Peak verursachen nicht zu vernachlässigende Einflüsse auf die Bestimmung der FCD.

Die in dieser Arbeit vorgeschlagene Pipeline wird mit Mustererkennungsansätzen auf zweiphasige Weise für eine einzelne EEG/MEG- oder kombinierte EMEG-Quellenrekonstruktion der epileptischen Aktivität kombiniert. Die Ergebnisse zeigen, dass EMEG-Quellenrekonstruktionen mit gebündelter epileptischer Aktivität in der Nähe von zwei FCDs liegen.

Acknowledgment

I would like to show my gratitude to people who supported me during my PhD studies, particularly:

- My thesis supervisor Prof. Dr. rer. nat. Carsten Wolters who motivated me to come to Germany giving me the great opportunity to do my studies in an interdisciplinary environment, advised me valuably (for scientific and not-scientific aspects) and guided me in a professional manner.
- Prof. Dr.-Ing. Jens Haueisen for accepting me as a PhD student and his scientific support.
- Prof. Dr.-Ing. Christo Pantev and Prof. Dr. Joachim Gross for giving me a safe place at the Institute for Biomagnetism and Biosignalanalysis in Münster and for sharing their scientific knowledge.
- My colleagues in the working group “Stimulation, Imaging and Modeling of NEURONal networks in the human brain” for their precious support, scientific discussions and for their friendly attitude.
- Maria Carla Piastra, Frank Neugebauer and Asad Khan for proofreading the thesis.
- Andreas Wollbrink for helping me with the setups of the experiments and the technical issues. Karin, Hildegard and Ute for their help with the EEG, MEG, MRI measurements.
- Our project cooperation partners Dr. med. Stefan Rampp, Dr. Robert Oostenveld, Dr. med. Gabriel Möddel for a productive collaboration and valuable scientific information exchange.
- All my colleagues at IBB for a friendly working environment.
- Paavo Leppänen, the coordinator of the ChildBrain project, and the participant p.i.s who made possible this project and all my ChildBrain colleagues for their nice attitude during the ChildBrain project.
- My wife, Maria, for her significant support all the time, the decision to follow me into this journey and for proofreading the thesis as well as my family for their support.

Finally, I am grateful to thank Prof. Dr. rer. nat. Carsten Wolters for the funding of this PhD (Projects: ChildBrain of Horizon2020 Marie Skłodowska-Curie and the Priority Program 1665 (project WO1425/5-1) of German Research Foundation (DFG)). Special thanks also to the “Alexander Onassis” Foundation for accepting me as scholar and supporting my PhD studies.

Contents

List of Figures	v
List of Tables	vii
Nomenclature	ix
1 Introduction	1
1.1 Motivation	1
1.2 Contribution	2
1.3 Structure	3
2 Fundamentals	5
2.1 Anatomy and Physiology of the Brain	5
2.2 Human Somatosensory System	6
2.2.1 Basic Anatomy	6
2.2.2 The P20/N20 Component	8
2.2.3 Stimulation Types of the P20/N20 Component	8
2.3 Epilepsy	9
2.3.1 Epilepsy as a Disorder	9
2.3.2 Focal Epilepsy	9
2.3.3 Focal Epilepsy Treatments	9
2.4 Source Analysis of Brain Activity	11
2.4.1 Electroencephalography and Magnetoencephalography	11
2.4.2 EEG and MEG Forward Problem	13
2.4.3 EEG and MEG Forward Solution	15
2.4.4 EEG and MEG Inverse Problem	16
2.4.5 EEG and MEG Inverse Solution	16
2.4.6 Combined EEG/MEG Source Analysis	19
2.4.7 Cortical Extent in Focal Epilepsy with Sub-Averaging	19
2.4.8 Realistic Head Volume Conductor Modeling	20
2.4.8.1 Skull	20
2.4.8.2 Related to Skull Conductivity Measures	22
2.4.8.3 Cerebrospinal fluid	23
2.4.8.4 Gray and White Matter	23
2.5 Magnetic Resonance Imaging	24
2.6 Transcranial Electric Stimulation	25
2.6.1 Basis of TES	25
2.6.2 TES Forward Problem	26
3 Experimental and Modeling Effects on the Source Analysis of Somatosensory P20/N20 Component	27
3.1 Material and Methods	27
3.1.1 Participants and Ethics Statement	27
3.1.2 EEG and MEG Acquisition	28
3.1.3 Somatosensory Evoked Potentials and Fields	28

3.1.4	MRI Sequences	29
3.1.5	Processing of Somatosensory Evoked Responses	30
3.1.6	Processing of Image Data	30
3.1.7	Calibrated Realistic Head Volume Conductor Models	32
3.1.7.1	Head Tissue Conductivities	33
3.1.7.2	The Effective Medium Approach for Brain Anisotropy	33
3.1.7.3	Two-level Individual Skull Conductivity Calibration	34
3.1.8	Source Spaces	35
3.1.9	EEG and MEG Forward Solutions	36
3.1.10	EEG and MEG Inverse Solutions	36
3.1.11	Multi-channel TES Targeting and Optimization	37
3.1.11.1	Constrained Maximum Intensity	37
3.2	Results	39
3.2.1	Experimental and Modeling Pipeline	39
3.2.2	Individual Skull Conductivity Calibrations	40
3.2.3	Effect of Modality, Head Modeling and Stimulation Type on the Reconstruction of the P20/N20 Component	41
3.2.4	Effect of Stimulation Type on Individually Optimized TES	47
3.3	Discussion	51
3.3.1	Effects of Head Modeling and Modality on the P20/N20 Reconstruction	53
3.3.2	Effects of Stimulation Type on the P20/N20 Reconstruction	56
3.3.3	Effects of Stimulation Type on the P20/N20 TES Targeting and Optimization	58
3.3.4	Study Limitations	59
4	Inter-Subject Variability of Skull Conductivity and Thickness with Age Influences	61
4.1	Material and Methods	61
4.1.1	Participants and Data Acquisition	61
4.1.1.1	Participants and Ethics Statement	61
4.1.1.2	Experiment and EEG/MEG/MRI Acquisition	61
4.1.2	Preprocessing of EEG/MEG	61
4.1.3	Head Model Preparation	62
4.1.4	Definition of Measures	62
4.1.4.1	Measures for Skull Conductivity Calibration	62
4.1.4.2	P20/N20 Surface Distance	63
4.1.4.3	Skull Thickness	65
4.1.4.4	Source Depth	66
4.1.5	Statistical Analysis	66
4.2	Results	67
4.2.1	Inter-Subject Variability in the Defined Measures	67
4.2.1.1	Variability in the Measures for Skull Conductivity Calibration	67
4.2.1.2	Variability in Measures and Gender Differences	69
4.2.2	Statistical Results	71
4.3	Discussion	73

5	EMEG Source Analysis and TES Modeling of an Epilepsy Patient with Cranial Burr Holes	81
5.1	Patient and Methods	81
5.1.1	Ethics Statement and Patient	81
5.1.2	EEG/MEG Acquisition and Preprocessing	83
5.1.3	Spike Detection	84
5.1.4	Image Data Collection and Processing	84
5.1.5	Realistic Head Volume Conductor Models	86
5.1.6	Source Reconstruction of Epileptic Activity with Sub-Averaging	87
5.1.7	Alternating Direction Method of Multipliers	88
5.2	Results and Discussion	89
5.2.1	Effects of EMEG Source Analysis on the Detection of the Focal Cortical Dysplasia	89
5.2.1.1	Source Analysis Comparisons	89
5.2.1.2	Co-localization of Source Analysis and MRI	92
5.2.2	Influence of Head Modeling on Source Reconstruction	93
5.2.3	Source Localization Comparisons	96
5.2.4	Optimized Multi-Channel TES in Focal Epilepsy	97
5.2.4.1	Head Modeling Effects on the Optimized TES	97
6	EMEG Source Analysis of Epileptic Activity with Calibrated Head Modeling and Pattern Recognition	103
6.1	Patient and Methods	103
6.1.1	Patient & Ethics Statement	103
6.1.2	Preprocessing of the Data	103
6.1.3	Clustering of Epileptic Spikes	103
6.1.4	Source Analysis	104
6.2	Results	105
6.2.1	Two-phase Clustering Approach	105
6.2.1.1	Combined EMEG Source Reconstruction	106
6.3	Conclusions	107
6.4	Author's Contribution	108
7	Conclusions and Outlook	109
	Bibliography	113
	Scientific Contributions	123
	Erklärung	127

List of Figures

2.1	The basic brain structure	6
2.2	The basic structure of the human somatosensory system	7
2.3	The ideally overlapped zones in epilepsy	10
2.4	EEG and MEG sensor configurations	11
3.1	The stimulation types	29
3.2	Segmentation pipeline with T1w and T2w MRIs for the creation of a six-compartment head model	31
3.3	Six compartment anisotropic realistic head model and source space	32
3.4	The main ingredients for the skull conductivity calibration procedure	35
3.5	Summary of the experimental and modeling pipeline	39
3.6	Calibrated head models	41
3.7	EW stimulation: Effect of modality and head model on P20/N20 reconstruction	42
3.8	Somatosensory evoked fields (SEF) and potentials (SEP) for the three types of stimulation	43
3.9	Effect of individual head modeling with focus on skull conductivity calibration on P20/N20 reconstruction	44
3.10	Effect of stimulation type on P20/N20 reconstruction	45
3.11	Optimized TES montages for the different stimulation types	48
3.12	Two-patch TES montages for the different stimulation types	49
3.13	The distribution of the current density fields using multi-channel TES on the inflated cortex and in the target area	50
3.14	The distribution of the current density fields using two-patch TES on the inflated cortex and in the target area	51
3.15	TES quality indices.	52
3.16	The averaged optimized currents on the TES electrodes per stimulation type	53
3.17	CMI performance based on the half-max radius:	54
4.1	Calibrated head model with white matter anisotropy	63
4.2	Visualization of the measures of Section 4.1.4 for one of the subjects	64
4.3	Source reconstruction of the P20/N20 component using combined SEP and SEF	68
4.4	Skull conductivity calibration curves for the twenty subjects	69
4.5	Descriptive statistics and inter-subject variabilities	70
4.6	Interaction of skull conductivity with age and skull thickness	72
5.1	Results of non-invasive presurgical workup and planning of the invasive EEG study	82
5.2	Grand-averaged MEG and EEG spikes	85
5.3	Patient's image data	86
5.4	Measurement modality source reconstruction comparisons	91
5.5	Indication of a cortical malformation based on source reconstruction result:	93
5.6	Head modeling effects on source reconstruction	94
5.7	Comparison of difference inverse methods	97

5.8	An alternative treatment option for the epilepsy patient with TES	98
5.9	Effects on the optimized TES montage due to head modeling	99
5.10	Effects on the TES current density due to head modeling	101
5.11	Effects on the TES current orientation and amplitude due to head modeling	102
6.1	Weights Distribution for Feature Vector	104
6.2	Evaluation of K-means clustering	105
6.3	Subaveraged EEG/MEG based on clustering	106
6.4	sLORETA combined EMEG source reconstruction for 2 nd EEG & 2 nd MEG cluster	107
6.5	sLORETA EMEG reconstruction leads to FCDs detection	107

List of Tables

3.1	Overview of the head models for every subject using in this chapter	40
3.2	The λ values for the different stimulation types	47
4.1	Gender-based mean and standard deviation across all the participants of the P20/N20 source analysis	69
4.2	Gender-wise mean and standard deviation of the thicknesses for outer and inner compacta and spongiosa skull compartments in the ROI	71
4.3	Interaction of age with the measures from Section 4.1.4	72
4.4	Interaction of the calibrated skull conductivity with all the cranial compartment thicknesses and the surface distance with the source depth.	74
5.1	Source analysis effect due to changes in the measurement modality for the most detailed 6CAH_Cal head model	90
5.2	Source analysis quality	92
5.3	Effect of head modeling on the evaluation of the epileptic activity	95

Nomenclature

ADMM	alternating direction method of multipliers
AMG-CG	Algebraic MultiGrid preconditioned Conjugate Gradient
ANOVA	Analysis of variance
BEM	Bounded element method
BT	Braille-Tactile
CI	Confidence of interval
CMI	Constrained Maximum Intensity
CSF	Cerebrospinal fluid
CT	Computed tomography
DT-MRI	Diffusion tensor MRI
DTI	Diffusion tensor imaging
EEG	Electroencephalography
EIT	Electrical impedance tomography
eLORETA	Exact low-resolution brain electromagnetic tomography
EMEG	Combined Electroencephalography/Magnetoencephalography
EW	Electric-Wrist
FCD	Focal cortical dysplasia
FDG-PET	Fluorodeoxyglucose positron emission tomography
FDM	Finite difference method
FDR	False discovery rate
FEM	Finite element method
FLAIR	Fluid-attenuated inversion recovery
fMRI	functional magnetic resonance imaging
GM	Gray matter
GOF	Goodness of fit
IED	Interictal epileptic discharges
LORETA	Laplacian weighted minimum norm
MEG	Magnetoencephalography
MNE	Minimum norm estimate
MRI	Magnetic resonance imaging
OPM	Optically pumped magnetometer
P14	The somatosensory evoked potential measured at around 14 ms after the stimulus for median nerve stimulation.
P20/N20	The somatosensory evoked potential measured at 20 ms post-stimulus.
PET	Positron emission tomography
PT	Pneumato-Tactile
ROI	Region of interest
RV	Residual variance
SC	Skull compacta
SDS	Single dipole scans
SEF	Somatosensory evoked fields
SEP	Somatosensory evoked potentials
SI	Primary somatosensory cortex
SII	Secondary somatosensory cortex
sLORETA	Standardized low resolution brain electromagnetic tomography

SNR	Signal-to-noise-ratio
SOA	Stimulus onset asynchrony
SPECT	Single-photon emission computed tomography
SS	Skull spongiosa
T1w MRI	T1-weighted magnetic resonance imaging
T2w MRI	T2-weighted magnetic resonance imaging
TES	Transcranial electric stimulation
TMS	Transcranial magnetic stimulation
WM	White Matter
WMNE	Weighted Minimum norm estimate

1 Introduction

1.1 Motivation

Electro- (EEG) and magnetoencephalography (MEG) source analysis of evoked response components as well as transcranial electric stimulation (TES) are influenced by a variety of modeling and experimental parameters. Some of them are well-known, while others are often considered to be less important or even negligible [1, 2]. Such parameters are, for example the measurement modality, i.e., EEG, MEG or combined EEG/MEG (EMEG) and the dielectric properties of the geometrical human head model used for the solution of the forward problem within the inverse source reconstruction procedure [3, 4, 5]. Moreover, experimental parameters can vary depending on the interest of the examiner and the complexity of the brain region of interest [6]. The human somatosensory system, a well controllable and deeply investigated brain network [6], is involved in this thesis. Special focus will be on the reconstruction of the somatosensory evoked potentials (SEP) and fields (SEF) component 20 ms post-stimulus, the P20/N20. This component has been characterized as largely exogenous and stable with good signal-to-noise ratio (SNR) in both EEG and MEG [6]. However, it is still unclear in which degree the dipole reconstruction of this component is affected by the fundamental parameters head modeling, measurement modality and stimulation type. Not yet answered remains also whether the use of different stimulation types can influence the optimization of currents in multi-channel TES (optimized TES) and the position of anodes and cathodes when using P20/N20 component as target.

It should be emphasized that the conductivity parameters of head modeling often rely on standard conductivities from the literature, while it is known that there is considerable inter-subject variability in their values [7, 8, 9]. In contrast to the magnetic modalities (MEG, TMS), for EEG source analysis [10, 11] and TES [12], skull conductivity has been shown to be the most influential of the head tissue conductivity parameters [12, 13, 14]. The use of EMEG with magnetic resonance imaging (MRI) is proposed in this thesis to individually estimate skull conductivity and relative of it parameters in healthy human subjects with the ultimate goal to investigate their inter-subject variability. The used modalities EMEG and MRI are available in most MEG-laboratories and the proposed procedure, due to its non-invasiveness, can be easily applied in neuroscientific research involving healthy human subjects and/or patients who suffer, for example, from focal epilepsy.

Epilepsy is a common neurological disease that affects more than 50 million patients from whom 30 % suffer from focal epilepsy [15]. For those patients who do not respond to two or three adequate antiepileptic drugs, epilepsy surgery is the most effective treatment option [15]. In these cases, invasive EEG studies with implanted electrodes are conducted but the success of an invasive EEG crucially depends on a valid hypothesis [16]. Non-

invasive methods such as source reconstruction of the irritative or seizure onset zone are likely to improve outcome by guiding correct placement of invasive electrodes [17]. EMEG source analysis has been proposed to be more precise than each EEG or MEG modality alone [18]. However, it is still unclear how the modeling of cranial holes created by previous operations and the tissue conductivity assignments could affect localization accuracy. Another important aspect on this accuracy is the selection of time-point relative to the spike peak. Furthermore, even if the presurgical evaluation indicates the irritative zone successfully [18], resection may not be feasible due to an overlap of this zone with eloquent cortical regions. For these cases, individually optimized TES could serve as promising treatment alternative for suppressing epileptic seizures [19, 20].

1.2 Contribution

One of the main contributions of this thesis is a sensitivity group study with five healthy subjects paving the way for P20/N20 source analysis and TES optimization for three stimulation types, namely Electric-Wrist (EW) stimulation of the right median nerve, Braille-Tactile (BT) and Pneumato-Tactile (PT) stimulation of the right index finger. The differences in source reconstructions due to these experimental conditions are compared to the differences due to measurement modality (EMEG or single modality EEG or MEG) and to the choice of the head model for the solution of the forward problem. The effects of forward modeling accuracy on the inverse reconstructions are also investigated using head models with either standard three (skin, skull and brain) isotropic tissue compartments or six (skin, skull compacta, skull spongiosa, cerebrospinal fluid (CSF), gray and white matter) compartments with brain (gray and white matter) anisotropic conductivity and individually estimated skull conductivity. To the best of the author's knowledge, this is the first EEG/MEG source analysis group study that introduces effects on the reconstruction of P20/N20 component due to the use of three different experimental conditions and modalities as well as individual high-resolution head volume conductor models with standard or individually calibrated skull conductivity. In this thesis, a pipeline that creates individual and high resolution (1 mm) head models was important in order to perform all group-level or single-case studies. In this regard, a new quasi-automatic segmentation procedure is introduced for the construction of individual six (or less) compartment head models combining T1-weighted (T1w) and T2-weighted (T2w) MRIs as well as computed tomography (CT).

Another contribution is the proposal of a two-level skull-conductivity calibration procedure that combines EEG and MEG modalities with MRI. It exploits the merits of the first transient component in the primary somatosensory cortex, the P20/N20 component, offering a stable calibration of the realistic head volume conductor model. It is used in the first study to investigate the influence of standard literature or calibrated skull conductivity on P20/N20 source reconstructions. This procedure is also applied on twenty healthy participants for investigating inter-subject variability of skull conductivity over the adult-age.

For this comparison, a new non-invasive method about the thickness estimation of the cranial and cancelous bone based on MRI was also developed. Additionally, a procedure for the definition of the measure, scalp surface distance between the potential peak and the potential trough, was created. This measure maximally resembles the measured SEP/SEF topography at 20 ms post-stimulus and reduces the influence of data noise on the peak-to-peak detection. To the best of the author's knowledge, this is the first EEG/MEG source analysis group study for the investigation of inter-subject variability of skull conductivity and thickness using modalities that are available in an MEG laboratory.

A final contribution is the use of EMEG source analysis for the localization of irritative zone in a patient with supposedly non-lesional left frontal lobe epilepsy. The patient had undergone a non-conclusive invasive video EEG workup with four depth electrodes in the left frontal region. As a result of the previous invasive EEG, the patient had four cranial burr holes overlying the left frontal region. These cranial burr holes are considered in finite element head modeling to investigate the effect on source reconstruction of the epileptic activity. As EEG and MEG are sensitive to different aspects of a given source, all results are compared showing that EMEG offers a more informative localization than each modality alone. Localization results were compared at two different time-points: middle of the rising flank of the spike and very onset of the spike. At the latter time point, it was highlighted that source reconstruction delivers more meaningful information. Source reconstructions with subsets of averaged spikes using single dipole scan and current density approaches are evaluated in order to estimate a centroid and an extend of the epileptogenic zone. Due to the difficulty on applying surgery in the present epilepsy case, the use of optimized TES is proposed as an alternative therapy for the suppression of epileptic seizures. For this purpose, head modeling effects on the simulated electric fields and optimized TES electrode montages are investigated.

1.3 Structure

In **Chapter 2**, the reader is introduced to the fundamental and theoretical knowledge of the topics covered in this thesis. The chapter starts with the basics of human brain anatomy and functionality with emphasis on the human somatosensory system and epilepsy. An explanation about EEG/MEG source analysis follows, including the forward and inverse solution of EEG and MEG as well as a description about the most influential head modeling parameters in source analysis. This chapter continuous with a description about MRI and finishes with the introduction of theoretical and mathematical background of TES.

Chapter 3 focuses on the description of the experimental and modeling pipeline developed in this thesis. It starts with the description of experimental and recording procedure. Then, the quasi-automatic segmentation procedure in this pipeline is described. Afterward, a two-level calibration procedure is explained for the estimation of skull conductivity. Finite Element Method (FEM) with the St. Venant approach and inverse solution

with single dipole scans (SDS) are then described. An optimization algorithm for distributing currents on multi-channel TES is presented. The influence of experimental and head modeling parameters on the dipole reconstruction of P20/N20 component and optimized TES electrode montages are described and interpreted in the result and discussion sections, respectively.

Chapter 4 is about the inter-subject variability of skull conductivity and thickness. Improvements in the image processing pipeline described in Section 3.1.6 are introduced. A new methodology for the estimation of skull thickness as well as measures relative to skull conductivity are described. Subsequently, the statistical analysis for the evaluation of relationships and differences is introduced. Finally, results for inter-subject variability of the measures and relative on them statistics are explained and discussed.

Chapter 5 presents a focal epilepsy case study, in which the potential of EMEG source analysis to reconstruct signals from a deep sulci-valley cortical region at the spike onset is investigated. It starts with the clinical history of the epilepsy patient including a description about the EEG/MEG/MRI/CT measurements. Subsequently, a description follows for the modeling procedure of patient-specific realistic head models with calibrated skull conductivity and white matter anisotropy. Literature based conductivity values and different number of tissue compartments are also evaluated. In this procedure, methodological aspects are described especially for the modeling of skull burr holes created after the implantation of invasive electrodes. Then, the effect of head modeling on the accurate determination of the epileptogenic zone is investigated. Finally, optimized TES electrode montages, influences of head modeling on them and the corresponding simulated injected currents are investigated.

Chapter 6 shows a study with EMEG source analysis and calibrated finite element head models in combination with pattern recognition approaches for the presurgical evaluation of interical spikes of a multi-focal epilepsy case.

Chapter 7 includes thesis's conclusions and outlook.

2 Fundamentals

2.1 Anatomy and Physiology of the Brain

The brain is considered as one of the most complex and multi-parametric biological system that manages the central and peripheral functionalities of the human being. It is located in the human head, which contains several soft and hard tissue layers in-between for protecting the brain from likely environmental hazards.

The study of the brain has already started from early centuries [21]. Heophilus of Chalcedon distinguished cerebellum from cerebrum and gave a clear description of the ventricles [22]. Later studies that were conducted by Cajal and Golgi led to the consensus that brain contains cells that are broadly categorized into nerve cells, or neurons, and supporting glial cells, or glia [21]. The neurons are responsible for the transmission of the nerve impulses and glia have a supporting character to this transmission. The main structure of a neuron consists of an axon, a dendrite and a soma. The elaborate arborization of dendrites allows signals to travel from one neuron to others and the axon enables the passing of those signals to other neurons. The soma is the main cell body, which contains the necessary cell structures for protein synthesis and energy production.

The main parts of the brain are the cerebrum, the cerebellum, the brainstem and the limbic system.

- The biggest and most relevant part of the brain is the cerebrum. The cerebrum is divided into two hemispheres and each one of them consists of four lobes: the frontal lobe, parietal lobe, temporal lobe and occipital lobe (Figure 2.1a). The first sign for dividing cerebrum into specialized regions was provided by Paul Broca in the 18th century. In a brain lesion study, he defined the so-called Broca area when discovering lesions in a specific cerebral region over the left frontal lobe of patients who could not speak [23].
- The cerebellum is located in the back portion of the skull below the temporal and occipital lobes and behind the brainstem (Figure 2.1a, red tissue). Gray matter tissue uniformly covers the white matter. However, still, deep gray matter nuclei also exist inside the white matter. The cerebellum is involved in motor control, the coordination of motor movements, and balance [23].
- The last cortical structure of the present brain division is the brainstem (Figure 2.1a, blue tissue). It connects the brain to other parts of the body and regulates crucial functions such as heart rate, blood pressure, body temperature, breathing, hunger and thirst.

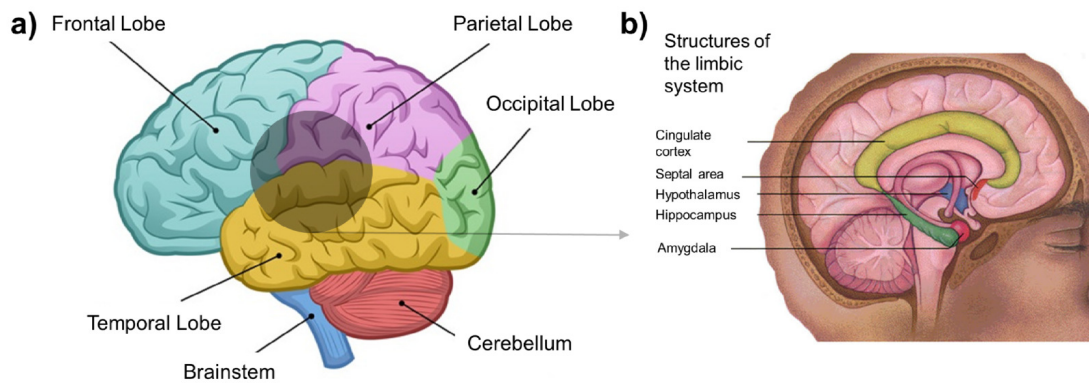


Figure 2.1: The brain structure: **a)** The basic structure of the brain, **b)** the limbic system. (adapted from wikicommons).

- The limbic system is a set of evolutionarily basic subcortical brain structures located on top of the brainstem and buried under the cerebrum (Figure 2.1b). The limbic system consists of structures and nerve fibers located deep within the cerebrum and it connects the hypothalamus with other areas of the frontal and temporal lobes, including the amygdala and hippocampus. It also contains the thalamus, which is a mass of gray matter and mainly functions as a relay center for sensory signals from the spinal cord to the cerebrum and vice versa.

2.2 Human Somatosensory System

2.2.1 Basic Anatomy

The human somatosensory system is a deeply investigated brain network belonging to the cerebrum of the brain and mediating the fifth sense through a range of sensations (touch, pressure, vibration, limb position, heat, cold, itch), and pain properties. These properties are transduced by receptors within the skin, muscles, or joints and conveyed to a variety of central nervous system targets [21]. It provides a substantial excitatory input for research and clinical trials [6] and is localized in the parietal lobe. The main pathway structure of it is divided into two parallel subsystems: the dorsal column-lemniscal (mechanoreception and proprioception) (Figure 2.2a, track in black) and the spinothalamic (thermoreception, nociception and visceroreception), (Figure 2.2a, track in red) [24]. The peripheral terminals of the dorsal column-lemniscal pathway are corpuscular nerve endings in the skin, joint capsule, and muscle. Free nerve endings in the skin, bone, joint capsule, tendon, muscle, and many visceral organs structure the spinothalamic pathway system. Fibers from the column lemniscus are connected to the ventral posterior lateral nucleus and from the spinothalamic to the ventral posterior medial nucleus. Both nuclei are part of the ventral posterior complex (Figure 2.2b: structure of thalamus). Then, fibers from the ventroposterior thalamus which

in turn projects to the primary somatosensory cortex (SI) in the postcentral gyrus and the secondary somatosensory cortex (SII) in the parietal operculum gyrus. The SI is divided into four regions (Figure 2.2b, areas 1, 2, 3a and 3b) and their functionality is described as follows: The area 3a responds to a proprioceptive stimulus, the areas 3b and 1 respond to cutaneous stimulus and area 2 processes the tactile and proprioceptive stimulus. The SII receives convergent projections from the primary somatic sensory cortex and in turn sends to limbic structures such as the amygdala and hippocampus [24].

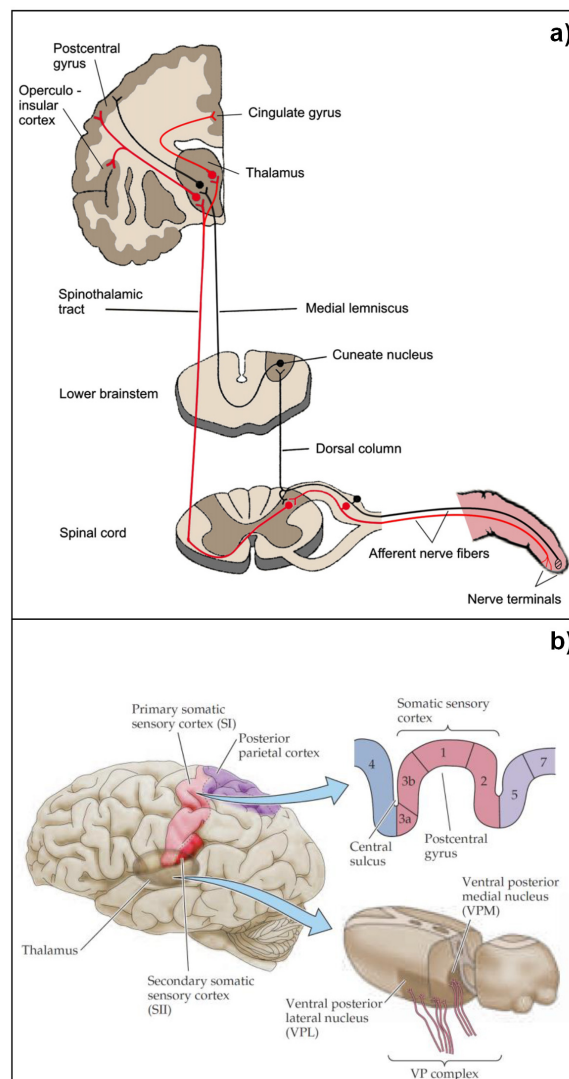


Figure 2.2: The structure of the human somatosensory system: a) The somatosensory pathways from the receptors to the primary somatosensory cortex via the afferent fibers. The dorsal column-lemniscal pathway is indicated with red color and the spinothalamic with black (adapted from [24]). b) The cortical (Primary and secondary somatosensory cortex) and subcortical structure (Thalamus) of the human somatosensory system (adapted from [21]).

2.2.2 The P20/N20 Component

For the characterization the functionality of the somatosensory network, the dorsal column-lemniscal pathway is preferred due to the lower electrical threshold on the fiber stimulation compared to the spinothalamic pathway [24]. Those fibers are preferentially activated applying a peripheral stimulus. Then action potentials (or signal) will travel from the afferent nerves of dorsal column-lemniscal up to the ventral posterior lateral nucleus and in turn projects to the SI (Figure 2.2a, track in black). The first response recorded by EEG/MEG is located in the ventroposterior thalamus at 14 ms after the stimulus onset. The first transient response is located in the area 3b at 20 ms post-stimulus. The response at 20 ms post-stimulus is called the P20/N20 component, for which the term “P” refers to a positivity and the “N” to a negativity of the EEG over the frontocentral and parietooccipital lobes, respectively. According to the sensory “homunculus” [24, 25], it has a mainly tangentially-oriented dipolar source origins on the postcentral wall of the central sulcus in SI contralateral to the side of stimulation. Invasive recordings support this dipole model in humans and monkeys [26]. The advantage of knowing the exact cortical position of the P20/N20 component makes SI a candidate brain network for the investigation the behavior of experimental and modeling source analysis parameters. Another advantage is not involving cognitive responses created by SII, which are often challenging to interpret. Thus, the P20/N20 component is especially appropriate for sensitivity investigations of EEG and MEG source analysis as well as estimations of human skull conductivity as performed in this thesis.

2.2.3 Stimulation Types of the P20/N20 Component

The P20/N20 component is most often produced by applying electrical or mechanical peripheral somatosensory stimulus. Commonly, electric stimulation of the median nerve is applied at the wrist [6, 26, 27]. The EW (Electric-Wrist) stimulation enables high SNR and elicits robust somatosensory evoked response data with sharp waveforms because each stimulus synchronously activates a large number of nerve fibers and a high stimulation frequency can be applied. However, electric stimulation is somewhat unnatural and directly activates both deep and superficial receptors, bypassing the peripheral receptors [25]. Additionally, a drawback of EW stimulation is the discomfort that subjects experience, especially during extended periods of stimulation. Therefore, a more physiologically natural excitation using mechanical tactile stimuli has been proposed and applied at the more sensitive (compared to the wrist) fingers [25, 28, 29, 30]. One possible technique is to use Pneumato-Tactile (PT) stimulation using a balloon diaphragm driven by bursts of compressed air. This has been used in several studies showing similar SI responses compared to the electric stimulation, however with a weaker and blurred response [25, 29]. An alternative tactile stimulation type, the so-called Braille-Tactile (BT) stimulation, was compared with electric finger stimulation in [30], resulting in significantly smaller BT source

activation when compared to the electric one. In this thesis, EW stimulation of the right median nerve as well as BT and PT stimulation of the right index finger are used. These experimental parameters were used for sensitivity investigations as presented in Chapter 3.

2.3 Epilepsy

2.3.1 Epilepsy as a Disorder

Epilepsy is a chronic disorder of the brain that affects 1 % of people worldwide and 2 % in EU, classifying it as one of the most common brain disorders [31, 32]. Every year, more than 5 million new cases are diagnosed with expectations to increase further [31]. Epilepsy is characterized by the involuntary recurrent occurrence of synchronous discharges in cerebral cortical neurons, called epileptic seizures [33]. The diagnosis of epilepsy requires at least two unprovoked seizures because approximately 10 % of the general population have at least one seizure during the lifetime. Nowadays, it is known that epileptic seizures are due to abnormal, synchronous and excessive electrical activity [34].

2.3.2 Focal Epilepsy

The primary categories of epilepsy are the grand mal, the petit mal, and the focal epilepsy [17]. In this thesis, the focus is on focal epilepsy. This type of epilepsy can occur in any local part of brain as well as deeper structures of the brain stem. Most often, focal seizures arise because of organic lesions due to a brain injury, brain infection, or functional abnormalities such as a tumor region. The electric activity of these seizures spreads to areas close to the vicinity of foci. This cortical region could be on the scale of a few millimeters or centimeters. The semiology of these seizures varies depending on the brain region in which the synchronous discharges are created.

2.3.3 Focal Epilepsy Treatments

Anti-epileptic drugs are the first treatment in line, helping about 60 % of the patients to become seizure free after the initial dose. Additional medication can increase the number of recovered epilepsy patients only up to 70 % [15].

For the remaining 30 % of patients with uncontrolled seizures, epilepsy surgery should be considered as the most promising treatment option [35, 36]. The principle of epilepsy surgery is to localize and resect the epileptogenic zone, i.e., the area of cortex which is capable of generating epileptic seizures [17]. In order to proceed to surgery, the epileptogenic zone has to be localized with sufficient accuracy. As there is no means to depict the epileptogenic zone directly, several surrogates have to be assessed, as described by [17]. This zone is a theoretical concept and a set of other theoretical and practical zones

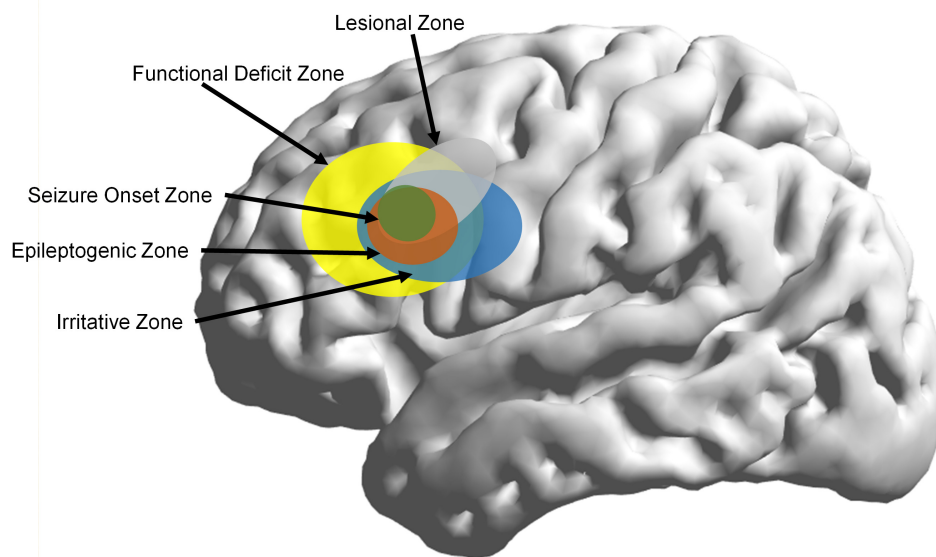


Figure 2.3: The epilepsy zones: A sketch with the overlapped zones in epilepsy.

(Figure 2.3) have to be detected with nowadays standard workups. These workups include a high-resolution magnetic resonance imaging (MRI) with specifications optimized to detect typical epileptogenic lesions (“lesional zone”) such as focal cortical dysplasia (FCD), heterotopia, or epileptogenic tumor [37], long-term video-EEG for recording of habitual seizures and interictal epileptiform EEG potentials, and neuropsychological testing. Seizure semiology is interpreted based on neuroanatomical knowledge (“symptomatogenic zone”). The ictal EEG is used to localize the “seizure onset zone”, the interictal EEG for localization of the “irritative zone”, neuropsychological data to determine the “functional deficit zone” [17]. This may be complemented by positron emission tomography [38], or ictal single-photon emission computed tomography (SPECT) for further specification of the “functional deficit” and “ictal onset” zones, respectively. Besides visual analysis of the raw EEG, source analysis of interictal spikes recorded on EEG or MEG has been increasingly used for more precise localization of the irritative zone in patients without or with multiple structural lesions or regions with unclear lesional status. Source reconstruction is especially essential whenever invasive EEG studies with implanted electrodes are considered, as the success of invasive EEG crucially depends on a valid focus hypothesis for optimal planning and guidance of electrode placement [39]. Recently, source analysis of ictal EEG patterns has also been established [40, 41]. The mapping of the eloquent cortex is also vital, especially in frontal lobe epilepsy, due to the possibility of an overlap with the epileptogenic zone that makes surgery a non-applicable procedure [19]. This happens in approximately 19 million patients, for whom, transcranial electric stimulation is emerging as a non-invasive therapeutic intervention for suppressing seizures [19, 20]. Therefore, the precise determination of epilepsy zones as well as eloquent cortex in presurgical epilepsy

of EEG and MEG is usually lower than fMRI and their sensitivity is getting weaker for sources far away from the sensors (e.g., sources in subcortical regions) [6].

Although EEG and MEG measure electrophysiological activity of the same underlying brain source, the recorded signals are different [4]. MEG is sensitive to the quasi-tangentially oriented sources while EEG can detect both quasi-radial and quasi-tangential sources [1, 4, 42]. The MEG is less sensitive to deeper sources compared to EEG, not only due to the distance from the source to the measurement sensors (MEG and EEG share the same drawback), but also because deeper sources are more radially oriented. On the other hand, SNR of the MEG signal is higher than EEG signal for more superficial sources because the quasi-radial biological noise contaminates the MEG signals to a smaller degree than the EEG signals [43]. Furthermore, the signal topographies of EEG and MEG are almost orthogonal to each other. The distance between the poles of the EEG topographies is in practice greater than for MEG because the low skull conductivity smears out the EEG. Thereby, combined recordings of EEG and MEG are likely to improve source analysis as they complement each other concerning the source types and orientations detected by both modalities [4, 44].

The human somatosensory system is one of the most commonly used networks for the investigation of EEG and MEG sensitivity differences in source analysis [2, 6]. For example, the reported EEG and MEG scalp topographies of the measured somatosensory responses in [27] were orthogonal as well as the corresponding EEG and MEG dipole source at the Brodman area 3b. Later studies also considered the source reconstruction of the P20/N20 component as the epicenter for investigating differences on the EEG/MEG sensitivity profiles due to its mainly tangential orientation and superficial location [3, 4, 30]. For example, conducting a source analysis with either individual EEG/MEG or EMEG for different conductivity profiles, the studies [3, 4] showed that EMEG exploits the complementary information of the individual modalities, resulting in P20/N20 source reconstructions that outperform the single modality ones. In this thesis, as presented in Chapter 3, a comparison using somatosensory evoked responses of five healthy subjects reveals that EEG and MEG are complementing and not competing modalities.

In focal epilepsy, it has been shown that EEG and MEG can detect different interictal spikes indicating that the simultaneous acquisition of EEG and MEG yield complementary diagnosis [45, 46]. Iwasaki et al. [45] reported that MEG detects spikes on 19 % of patients (8/43 patients), EEG on 2 % of patients (1/43 patients) and both EEG/MEG detect spikes on 72 % of patients (31/43 patients). A year later, Knake et al. [46] also showed that visible spikes with EEG are only on 3 % of patients (2/67 patients), 13 % of patients (9/67 patients) with MEG and 75 % of patients (50/67 patients) with both modalities. Recently complementarity between EEG and MEG has also been observed during source analysis [47, 48]. Aydin et al. [47] showed in a single epilepsy case that EMEG outperforms single EEG or MEG source analysis using calibrated and realistic head modeling, comparing the results with stereo EEG recordings. On the other hand, using simplified head models,

Ebersole and Wagner [48] report a series of 297 consecutive patients, identifying different types of spikes in a range from 0 up to 10. Of all spike types, 8 % were detected in MEG alone, 36 % were seen in EEG alone, and a 56 % of spike types was present in both EEG and MEG. These results make clear that the different sensitivity profile of EEG and MEG could bring source localization closer to the epilepsy foci. Such a complementary result is presented in this thesis (Chapter 5).

2.4.2 EEG and MEG Forward Problem

The forward problem of EEG and MEG is solved by iterative simulations of electric potentials at the head surface and magnetic fields at a small distance to the head surface for a given current source in the brain. The basis for these simulations is the geometrical model of the human head [2, 49].

The Maxwell's equations form the basis of electromagnetism and thus the forward problem of bioelectromagnetism:

$$\nabla \times \mathbf{E} = -\frac{\partial \mathbf{B}}{\partial t} \quad (2.1)$$

$$\nabla \times \mathbf{H} = \mathbf{J} + \frac{\partial \mathbf{D}}{\partial t} \quad (2.2)$$

$$\nabla \cdot \mathbf{B} = 0 \quad (2.3)$$

$$\nabla \cdot \mathbf{D} = \rho \quad (2.4)$$

with \mathbf{E} : Electric field (volt per meter (V/m)), \mathbf{H} : Magnetic field strength (ampere per meter (A/m)), \mathbf{B} : Magnetic flux density ($T = kg/(s^2A)$), \mathbf{D} : Electric displacement field (C/m^2), \mathbf{J} : Current density (A/m^2), ρ : Volume charge density (C/m^3). The corresponding units are $V =$ volt, $m =$ meter, $A =$ ampere, $T =$ tesla, $kg =$ kilogram, $s =$ second, $C =$ coulomb.

The material equations listed below supplement Maxwell equations:

$$\mathbf{D} = \epsilon \mathbf{E} \quad (2.5)$$

$$\mathbf{B} = \mu \mathbf{H} \quad (2.6)$$

$$\mathbf{J} = \sigma \mathbf{E} \quad (2.7)$$

where ϵ (F/m) is the permittivity, μ (H/m) is the permeability, σ (S/m) is the conductivity.

The properties at the interfaces of different media are given by the boundary conditions:

$$\mathbf{n} \times (\mathbf{E}_2 - \mathbf{E}_1) = 0 \quad (2.8)$$

$$\mathbf{n} \times (\mathbf{H}_2 - \mathbf{H}_1) = 0 \quad (2.9)$$

$$(\mathbf{D}_2 - \mathbf{D}_1) \cdot \mathbf{n} = \rho_s \quad (2.10)$$

$$(\mathbf{J}_2 - \mathbf{J}_1) \cdot \mathbf{n} = -\frac{\partial \rho_s}{\partial t} \quad (2.11)$$

with ρ_s representing the surface charge density at the interface and \mathbf{n} being the outward normal direction from the material 1 to 2. The equations 2.8, 2.9 indicate the continuity in the tangential direction and 2.10, 2.11 represent the discontinuity in the medium.

In the low frequency regime of EEG and MEG forward problem (below 1000 Hz), the quasi-static approximation of Maxwell's equations can be used. This approximation refers to treating the electrical and magnetic fields as in steady-state for any time instant, which means that the secondary effects of the time variation are neglected [50]. Thus, the Maxwell's equations reduce to:

$$\nabla \times \mathbf{E} = 0 \quad (2.12)$$

$$\nabla \times \mathbf{H} = \mathbf{J} \quad (2.13)$$

$$\nabla \cdot \mathbf{B} = 0 \quad (2.14)$$

$$\nabla \cdot \mathbf{D} = \rho \quad (2.15)$$

The electric field can thus be represented by a potential (ϕ):

$$\mathbf{E} = -\nabla \phi \quad (2.16)$$

In case of the EEG/MEG forward problem, the total current density \mathbf{J} can be assumed to be composed of conduction current density $\sigma \mathbf{E}$ and the so-called primary current \mathbf{J}_p (representing brain neural activity)

$$\mathbf{J} = \sigma \mathbf{E} + \mathbf{J}_p \quad (2.17)$$

and 2.17 becomes the Poisson equation for the electric potential on a head domain Ω :

$$\nabla \cdot (\sigma \nabla \phi) = -\nabla \cdot \mathbf{J}_p \quad (2.18)$$

with homogeneous Neumann boundary condition on the head surface $\Gamma = \partial\Omega$

$$\mathbf{n} \cdot (\sigma \cdot \nabla \phi) = 0 \quad (2.19)$$

The Poisson equation for the magnetic field can be obtained by substituting the magnetic flux density (\mathbf{B}), which is equal to $\mu \mathbf{H}$, with the curl of the magnetic potential (\mathbf{A}) in

equation 2.13:

$$\nabla^2 \mathbf{A} = -\mu \mathbf{J} \quad (2.20)$$

This leads to the representation:

$$\mathbf{A}(\mathbf{x}) = \frac{\mu}{4\pi} \int_{\Omega} \frac{\mathbf{J}_p(x') - \sigma(x') \nabla \phi(x')}{|x - x'|} d\mathbf{x}' \quad (2.21)$$

A well-used assumption that is used in EEG/MEG forward problem is to represent the source with the mathematical point dipole. The mathematical point dipole can be represented as:

$$\mathbf{J}_p(\mathbf{x}) = \mathbf{m}_0 \delta(\mathbf{x} - \mathbf{x}_0) \quad (2.22)$$

with \mathbf{m}_0 is the dipole moment, \mathbf{x}_0 is the dipole position and δ is the Dirac delta function. Using Stokes theorem, the magnetic flux Ψ measured by using a magnetometer with surface area S and circumference l can be written as:

$$\Psi = \int_S \mathbf{B} dS = \oint_l \mathbf{A}(\mathbf{x}) d\mathbf{x} \quad (2.23)$$

$$\Psi = \underbrace{\frac{\mu}{4\pi} \oint_l \int_{\Omega} \frac{\mathbf{J}_p(\mathbf{y})}{|\mathbf{x} - \mathbf{y}|} d\mathbf{y} \cdot d\mathbf{x}}_{\text{primary magnetic flux}} + \underbrace{\frac{\mu}{4\pi} \oint_l \int_{\Omega} \frac{-\sigma(\mathbf{y}) \nabla \phi(\mathbf{y})}{|\mathbf{x} - \mathbf{y}|} d\mathbf{y} \cdot d\mathbf{x}}_{\text{secondary magnetic flux}} \quad (2.24)$$

2.4.3 EEG and MEG Forward Solution

The EEG/MEG forward solution can be proven to be unique and exists for single and distributed dipole sources [51, 52]. Although analytical solutions exist for certain geometries as in the case of multi-sphere models [52], for realistic head models numerical techniques are needed. The most widely used techniques are either the bounded element methods (BEM) [52], the finite element methods (FEM) [51] or the finite difference methods (FDM) [53]. In the present thesis, FEM was used because of its high flexibility to accurately model the electromagnetic field propagation in geometrically challenging inhomogeneous and anisotropic head volume conductors such as the human head [5, 54].

An important decision for performing FEM in reasonable amount of time is to choose a proper method to treat the singularity introduced by the mathematical dipole. Proposed approaches are “partial integration direct potential” approach, “subtraction” approach, “Venant direct” approach [52] as well as “H(*div*)” approach [55]. In this thesis, the Venant direct approach was used due to its high accuracy and computational efficiency as shown in [51, 56]. When using FEM, an increased number of elements is needed for modeling all the complex geometries of the modeled volume but the computational costs can be reduced significantly due to the use of sparse matrices [57]. The use of efficient solvers like parallel algebraic multigrid preconditioned conjugate gradient method [58] and especially fast FEM transfer matrix approaches [57], make possible to solve the EEG/MEG forward problem for many

head models with millions of elements as shown in this thesis. These calculations were in a reasonable amount of time on ordinary computers.

In FEM, three-dimensional elements such as hexahedra or tetrahedra are used to model the head volume. The advantage of hexahedra is that it is easier and faster to obtain the mesh out of the labeled MRI. For hexahedral meshes, the voxels in the labeled MRI volume can be directly converted to mesh elements. In contrast to tetrahedral meshes, this direct conversion is not possible and further elaboration of the segmented model is necessary to create tissue compartments that are not intersect each other. Usage of hexahedral meshes was shown to result in not smooth and less-realistic edges, which is known as staircase effect. This effect is mitigated by shifting the nodes to the material interfaces [59]. This approach was evaluated in EEG source analysis with multi-layer sphere models, showing major error reductions compared to regular hexahedral approaches [51].

2.4.4 EEG and MEG Inverse Problem

Up to now many efforts have been made to reconstruct the spatio-temporal dynamics of primary currents measured with EEG/MEG. This reconstruction refers the EEG/MEG inverse problem. The inverse solution requires repetitive simulations of the electromagnetic fields on a head model for a source distribution (solution of forward problem). The goal is to reconstruct the primary currents. However, the EEG/MEG inverse problem is ill-posed due to an infinite number of source configurations that can produce the same EEG/MEG measurements (non-uniqueness) [60]. To tackle this non-uniqueness, a set of prior assumptions to the inverse solution about the type of sources are made by setting anatomical/neurophysiological constraints or a fixed number of underlying sources.

The general formulation of the inverse solution for the reconstruction of the measured EEG and MEG activity is given by following linear equations:

$$\mathbf{Y}_{EEG} = \mathbf{L}_{EEG} \mathbf{j} \quad (2.25)$$

$$\mathbf{Y}_{MEG} = \mathbf{L}_{MEG} \mathbf{j} \quad (2.26)$$

Considering a time instant, a set of N_{EEG} (M_{MEG}) number of EEG (MEG) sensors and N_{sp} source space points that represent the mathematical point dipoles, \mathbf{Y}_{EEG} (\mathbf{Y}_{MEG}) is the $N_{EEG} \times 1$ ($M_{MEG} \times 1$) measurement vector, \mathbf{j} is the $3N_{sp} \times 1$ source vector and \mathbf{L}_{EEG} (\mathbf{L}_{MEG}) is the $I_{EEG} \times 3N_{sp}$ ($I_{MEG} \times 3N_{sp}$) the leadfield matrix (forward solution).

2.4.5 EEG and MEG Inverse Solution

A variety of inverse reconstruction algorithms that are based on different a priori assumptions have been developed over the last decades. These algorithms are mainly categorized as equivalent current dipole approaches, current density reconstruction, beamforming approaches and hierarchical Bayesian modeling [60, 61].

In equivalent dipole approaches, a set of dipole sources is used to represent the reconstructed activity inside the brain. For both linear and non-linear equivalent dipole approaches, the investigated activities should satisfy the assumption of focality. The used dipoles usually vary from 1 up to 5 [3]. Each dipole contains three location and three moment parameters and thus only six parameters need to be estimated. To estimate these parameters, one can use the so-called moving dipole in which the calculation is done separately at each time instant. An alternative is to keep the location (rotating dipole) or both location and orientation (fixed dipole) constant for a certain time. Instead of the dipole scan approaches, in classical dipole fit algorithms, the three location parameters are calculated using nonlinear optimization techniques and dipole moments are calculated with a simple linear fit [62, 63]. A well-known problem of these algorithms is that the optimization algorithm might get trapped in a local minima [64].

In this thesis, single dipole scans (SDS) (also known as deviation-, goal function- or residual variance- scans) [3, 49] were used to estimate sources underlying somatosensory evoked responses and recorded epileptic spikes. These signals were shown to arise from relatively focal sources inside the brain [6, 27]. SDS belongs to the category of linear equivalent dipole approaches. This algorithm is performed on a predefined source space grid, which accounts for a more natural approach when used in combination with multi-compartment FEM forward modeling compared to dipole fit algorithms. The apparent drawback of SDS is that computational costs increases dramatically when the underlying activity is assumed with more than two dipoles. The goal of the SDS algorithm is to provide the source space location with minimum residual variance (RV). The RV is the squared deviation of the best fitting dipole to the measurement data. It is calculated for all source space locations which avoids to trap in a local minimum in case of using dipole fits. The RV value is calculated by $RV = \left\| \left(1 - L (L^T L + \lambda^2)^{-1} L^T \right) Y \right\|^2$ in which L represents the corresponding lead field matrix, Y is the measurement matrix depending on the measurement modality (EEG, MEG or EMEG) while λ is the regularization parameter important in case of plausible source reconstructions. Alternative of RV metric is the goodness of fit (GOF) and it is calculated as $GOF = 1 - RV$. To reduce the unknown parameters in SDS, a constraint can be imposed by restricting the source space only in gray matter (as it is performed in this thesis, see Section 3.1.10) or allowing the orientations of the dipoles to be only perpendicular to the surface of the gray matter. The latter constrain is justified by the fact that the EEG and MEG signals are produced by the pyramidal cells that are perpendicular to the cortex surface [1]. Head modeling errors in the gray matter should be considered before imposing these kinds of constraints and this is why the normal-constraint was not used in this thesis. The common problem with all these dipole models is that the number of dipoles has to be determined a priori to avoid spurious results. Recently, new inverse approaches proposed that this number parameter can be estimated by the measured data [60] (and references therein).

Another method in the category of the equivalent current dipoles is the multiple signal

classification which locates multiple asynchronous dipolar sources from the measured data [62]. With this method, the scanning of single-dipole is applied in the given source space. The use of principal component analysis can be used to estimate dipole orientation saving calculation time compared to the initial version of this method [65].

For current density approaches, a source space is first constructed and then one (with normal constraint) or three (without normal constraint) dipoles are calculated per source node. Compared to SDS, the number of dipoles is equal to the number of source space which can be restricted to the gray matter with orientations perpendicular to the cortical surface. An obvious downside of these algorithms is that the number of sources (usually about 10,000) is significantly higher than the number of measurements (usually less than 370) pointing very much to the severely ill-posedness of the inverse problem. Several solutions has been suggested the last years from which the most used or promising approaches are described in the following paragraphs.

One of the simplest and fastest inverse algorithms is the Minimum Norm Estimates (MNE). Among many solutions with low residuals the one with the smallest L2 norm of the overall current density is selected [1]. A significant drawback of this algorithm is that deep sources are punished with high amplitudes and superficial sources are favored which causes depth localization bias [60]. To alleviate the depth bias in MNE, an additional term is introduced to the MNE formulation (Weighted-MNE or WMNE) [66].

Another typical current density approach is the low-resolution electromagnetic tomography (LORETA). It calculates the solution which minimizes the laplacian of the weighted sources and thus favors spatially smooth results [67]. In an updated version of LORETA, standardized LORETA (sLORETA) [68], the minimum norm reconstructions are normalized by the posterior covariance and the output is a statistical map. It produces a fast solution as the MNE. For different noise levels, sLORETA gives the best solution compared to the MNE reconstruction in terms of localization error [60]. However, reconstructions with sLORETA are shown to be artificially dispersed (the extent is overestimated) and the source reconstructions are not accurate for sources in a very close distance [60]. Another version of LORETA, the exact LORETA (eLORETA) [69], is a method is similar to sLORETA, but it estimates current densities unlike statistical maps. The clear advantage of this method over sLORETA is the ability to punish less significant sources with low amplitudes but it comes with higher computational costs.

One of the most promising inverse methods is beamforming. The basic idea of beamforming is the application of spatial filtering on the measured data to distinguish signals arriving from a region of interest and suppress those originating elsewhere. The most typical categories of beamformers are the linearly constrained minimum variance approach in the time domain [70] and the dynamic imaging coherent of current sources [71] in the frequency domain.

The last and emerging framework with up-and-coming inverse solutions is the Hierarchical Bayesian approaches. In these methods uncertainties are allowed in the prior model

and the data itself is used to approximate the model by using hyperparameters that are introduced with a priori distributions in a hierarchical way [60].

2.4.6 Combined EEG/MEG Source Analysis

EEG and MEG are two measurement modalities that complement each other concerning the measured brain activity as described in recent findings (see Section 2.4.1). These findings motivate many researchers to move a step forward with the evaluation of simultaneous use of EEG and MEG for measuring and analyzing electrophysiological activity [3, 4, 44, 48]. However, EEG and MEG measure signals of different quantity and thus the corresponding units of those signals are different. To perform a combined source analysis both modalities need to be transferred to a common space. One method is to normalize the leadfield matrices using their norms [2]. An SNR based transformation [3] is used in the present thesis. In this approach, the data are whitened according to the noise level of each channel so that unitless measures for EEG and MEG are obtained. Afterward the equations 2.25 and 2.26 are combined to obtain the EMEG formulation. Before this combination, the EEG and MEG leadfield matrices and measurements are stacked in a row wise form after normalization with SNR to make them unit-free [3].

2.4.7 Cortical Extent in Focal Epilepsy with Sub-Averaging

Each individual spike recorded with EEG, MEG, or both represents an interictal event characterized by simultaneous (“hypersynchronous”) discharge of a larger number of neurons within a localized patch of cortex. It carries spatiotemporal information, with a supposedly very focal onset, and a rapid spread to neighboring areas. This has two important implications for source reconstruction: First, the most valuable spatial information should be expected at the spike onset, where the SNR is low. The rising flank of the spike and spike peak, although offering a much better SNR, are likely to represent activity spread to neighboring cortex areas, thus losing information about the area-of-onset. Second, all activity at each time-point is likely to be extended to other cortical regions. This information about the extent of activity is lost when using single dipole scanning approaches. SNR can be improved by averaging a large number of individual spikes, assuming that they all arise from the same cortical origin and their existence [72]. However, single dipole scanning of an averaged spike means that all information about activity extent is lost [47]. On the other hand, individual single spikes can be used for source reconstruction, resulting in a spike cluster [72]. This carries information about the extent of the active cortex, but the most valuable spatial information at the spike onset is lost due to low SNR. A compromise, improving SNR while keeping information about the extent of the active cortex can be achieved by averaging subsets of individual spikes (“sub-averaging”), and calculating both a center of gravity and surrounding spread spheres for a cluster of averaged spikes. In a recent study [47], it was shown that this approach offers accurate information about

the center of gravity and the extent of the epileptogenic zone when correlating it to the results of invasive EEG. This study was, however, limited to the use of only dipole scanning approaches. In this thesis, WMNE and sLORETA are additionally examined to see whether current density approaches can show meaningful information

2.4.8 Realistic Head Volume Conductor Modeling

A realistic head volume conductor model is important for modeling both geometrical and dielectric properties of the head. These properties need to be accurately estimated for precise forward and inverse solution. This poses a challenging task due to the high number of differently conductive head tissues and the inter- and intra-individual differences in conductivities of some of the essential head tissues such as the human skull [13, 73]. Simplifications and homogenizations need to be made to the available imaging data, usually MRI, for constructing a suitable head volume conductor model. On the one hand, the achievable detailedness of the model depends only on the degree to which different tissues can be distinguished in the image data. On the other hand, more precise models require more effort and time for segmentation and more sophisticated mathematical methods and are therefore generally more labor-intensive and computationally expensive [13, 44].

Conventional approaches with MRI data segment the head into scalp, skull and brain, resulting in a realistically-shaped three compartment isotropic head model [2, 3, 4]. More detailed approaches segment the brain further into cerebrospinal fluid, gray and white matter, and/or skull into two compartments [11, 53]. Moreover, brain anisotropy can be incorporated by using diffusion tensor imaging (DTI) data [53, 74, 75], resulting in six compartment anisotropic head models [5, 44]. In the next subsection, a description of the most important tissue compartments investigated in this thesis is given.

2.4.8.1 Skull

The skull accounts for one of the most sensitive compartments for EEG and MEG forward modeling. The main skull structure contains the compacta (compact bone) layers and spongiosa layer, which is sandwiched in the middle, and it includes air-filled cavities such as the paranasal sinuses and the mastoid cells. The skull structure of infants differs significantly from adults, and in these cases, the fontanels should also be included into the model [76, 77]. It should be noted that the skull might have different conductivities throughout its whole structure [78]. However, the modeling of a three-layered skull (compacta-spongiosa-compacta) with likely defects (e.g. skull holes) and estimation of individual conductivity is more critical than the geometrical accurate modeling of the skull tissue [79]. For example, as shown in [80], skull defects can cause important attenuation in the electric fields. Hence, modeling of air cavities for highly accurate skull is avoided and only skull compacta and spongiosa is extracted by using CT or T2w MRI [11, 44]. Although CT offers a high accuracy on the skull reconstruction and used in clinical application (e.g. depth

electrode implantation in the human head), it is mainly avoided to use in healthy subjects due to the ionizing radiation to the subject's soft tissues (e.g, brain). The advancements in MRI technology, nowadays, enabled researchers to model the anatomy of the skull more accurately and most advanced studies to use T2w images with high resolution (1 mm), whereby it is possible to differentiate skull spongiosa and compacta [79].

Skull conductivity is approximately one order of lower magnitude than other known tissues as scalp or brain tissues [13]. Several studies investigated the impact of skull conductivity uncertainties on electric potential distributions [14, 77]. Small changes on skull conductivity can cause substantial attenuations on the modeled electric fields, resulting in localization errors in the centimeter range and orientation changes of more than 25° [10, 44]. For the somatosensory P20/N20 component, Vorwerk et al. [13] investigated how uncertainties inherent to the experimentally determined conductivity values of the different compartments influence the results of EEG source analysis. Skull conductivity uncertainty was found to have the biggest influence on forward ([13], Table 2) and inverse source analysis ([13], Fig. 7 – 9). Uncertainties in the skull conductivity can lead to changes in source localization of up to 2 cm ([13], Fig. 7A and 9). These changes could also cause amplitudes that are four times higher and unrealistic orientations of the modeled current density for TES [12, 81].

Various measurement approaches such as electrical impedance tomography (EIT) [82, 83], magnetic resonance EIT (MREIT) [84], magneto acoustic tomography (MAT) [85], and directly applied current (DAC) [8, 9] have already been studied to determine skull conductivity. While these approaches need further specialized equipment and/or expertise (EIT, MREIT and MAT) and/or are invasive (DAC), in this thesis, combined modalities EEG and MEG as well as MRI for the individual estimation of skull conductivity in healthy human subjects with the aim of investigating its inter-subject variability.

Estimating skull conductivity with EMEG and MRI has already been proposed in three-compartment head modeling studies [3, 4, 83] and in first case studies with more realistic head models [44, 86]. In all of these studies, a so-called “bulk skull conductivity” parameter was estimated in a calibration procedure that included source analysis of somatosensory evoked responses P20/N20 component. Although other studies proposed to estimate skull conductivity based on only SEP data [14, 76], additional SEF data stabilize the estimation [86]. This is due to the complementarity of EEG and MEG data [4, 42] and the insensitivity of MEG localizations to skull conductivity [2, 73, 76].

Gonçalves et al. [83] found a strong agreement between the results of an EIT procedure and the SEP/SEF method, even though they are quite different, both in theoretical and technical terms, indicating the stability of the SEP/SEF based calibration. EIT uses Ohm's law between the measured voltages and the injected currents [82]. Both methods function under in vivo conditions and in low frequency ranges [7].

A common feature of aforementioned methods is that they are relying on an accurate and realistic head model with individual compartments [5, 7]. In this regard, most of the

above SEP/SEF calibration studies were based on the modeling of homogenized compartments such as single-layer skull. In the present thesis, the skull is modeled as a three-layer structure and the inter-subject variability of its conductivity is investigated. A fixed ratio between skull compacta and spongiosa is also used in order to reduce the number of degrees of freedom during the skull conductivity calibration procedure to one in order to avoid overfitting [29, 86]. Therefore, the definition of the term “bulk skull conductivity” as introduced above is refined to be from now on the calibrated value for skull compacta conductivity in combination with the fixed ratio to the spongiosa.

2.4.8.2 Related to Skull Conductivity Measures

Skull conductivity is strongly and positively correlated to skull thickness as reported in [87] using excised skull samples. It is therefore important that the head model also represents skull thickness accordingly. While accurate skull thickness can best be determined using CT (Lillie et al., 2016), the non-invasive procedure proposed here is based on MRI. Using T1w MRI with a segmentation approach, Gorbenko et al. (2020) accurately segmented soft tissues, but with only 67 % specificity and 83 % sensitivity results were rather limited concerning the skull. This is because the low contrast between cerebrospinal fluid (CSF) and cranial tissue makes it difficult to estimate the inner skull boundary from T1w MRI alone. Therefore, in the present study, T1w and T2w scans are used for an improved MRI-based estimation of skull thickness.

It has also been assumed that skull conductivity may vary due to demographic factors such as age [8, 88], and particularly over infancy [7, 89]. Using direct measurements of the (homogeneous) skull conductivity of skull pieces, temporarily removed during epilepsy surgery, Hoekema et al. [8] observed a weak negative correlation over an adult age group of five patients. Such a negative correlation was furthermore supported by [90] based on EIT measurements on a small number of participants. On the other hand, in CT studies, it was reported that skull thickness in adults varies substantially among individuals and is independent of age [91, 92] but dependent on subject's gender [93]. However, it is not yet clear whether gender can also influence skull conductivity and its inter-individual variation in an adult age group.

The influence of inter- and intra-individual skull conductivity variations has already been highlighted in previous studies [11, 44, 73, 82]. It is clear from these studies that, for a fixed dipolar source in the brain, differences in skull conductivity result in differences in the surface distance between the two poles, the potential peak and trough, of the corresponding EEG forward solution potential topography. The latter means that lower skull conductivity leads to a higher pole distance (see also [94, 95]). However, in practical P20/N20 measurements, the measure of the scalp surface distance between the P20 potential peak and the N20 potential trough well depends on the EEG recording quality, the number of available electrodes and the accuracy in the assumption that the underlying source is a single focal dipolar source.

A fourth investigated measure introduced in this thesis relates to the *source depth*. As in the EEG source analysis studies of [13, 73], source depth is defined here as the distance between source location and the closest point at the inner skull surface; the larger this distance, the deeper the source is considered to be. Since source depth and skull conductivity are closely related to each other [13], it will be valuable to evaluate this additional measure to gain further insight into the inter-subject variability of skull conductivity.

2.4.8.3 Cerebrospinal fluid

Cerebrospinal fluid (CSF) is inside the skull and shows very high conductivity compared to other known compartments such as scalp or brain tissues. Its conductivity was measured in average across 7 subjects to be 1.79 S/m at body temperature for a range of 4.5 months up to 70 years [96]. Recently, no significant inter-individual differences were reported based on multiple regression model among several studies relevant to CSF measurements [7]. Up to now, many EEG/MEG source reconstruction studies use low-parametric three compartment head models with homogenized brain (including CSF), skull and scalp surfaces. However, these models still exclude the significant influence of the highly conductive CSF compartment inside the skull. The stable conductivity of CSF reduces the modeling problem to just segmenting its complicated geometry. The great achievements in structural imaging of the inner tissues of the brain make this segmentation feasible due to the easily recognizable CSF compartment from the skull or the holes (i.e., sinus cavities) based on the highly contrasted grey-scale pixels in T2w MRI that appear white color. In the absence of T2w MRI, the CSF segmentation is based on the matching of the segmented brain and inner skull compartments from T1w MRI because the CSF is not visible in such a type of MRI.

2.4.8.4 Gray and White Matter

The neglect of a distinction between gray matter (GM) and white matter (WM) is another simplification of three compartment models, representing them a single homogeneous compartment together with the CSF with an isotropic conductivity of 0.33 S/m. Recent studies showed that the distinction of white and gray matter conductivities (WM: 0.14 S/m and GM: 0.33 S/m) has a strong impact in EEG, MEG and EMEG source analysis [7, 13, 97]. In addition, a realistic construction of the sources measured with EEG or MEG are known to reside within the gray matter but not in the white matter [5].

Both gray and white matter have anisotropic conductivities. This anisotropy can be very high especially at pyramidal tracts inside the white matter. The gray matter anisotropy is considerably lower in comparison to white matter and its measurement with 3T scanners might be prone to errors especially due to partial volume effects of CSF compartment. Previous studies investigated the impact of anisotropic conductivities on EEG/MEG source

analysis showing that modeling might have a minor effect on the localization of the underlying source. However, it can significantly affect the source orientation and strength [5, 54]. Furthermore, the source orientation component is often considered to also contain important localizational information [98, 99]. Earlier studies used a fixed ratio for parallel and orthogonal directions to the fibers, but now with the advancements in diffusion tensor imaging and after the introduction of the relationship between diffusion and conductivity tensors [74], newer studies use the eigenvalues of diffusion tensors for this purpose [99]. In this thesis, the gray matter anisotropy was included to the head models described in Section 3.1.7.2. However, based on the findings of [44], only white matter anisotropy is included for the rest of studies in the present thesis.

2.5 Magnetic Resonance Imaging

To solve the bioelectromagnetic forward and inverse problem as well as to determine measures as introduced in Section 2.4.8.1, accurate realistic head modeling is important, as explained in Section 2.4.8. In the present thesis, MRI was used to obtain the geometries of different tissue compartments inside the head as well as brain or white matter conductivity anisotropies.

MRI relies on the nuclear magnetic resonance phenomenon for image construction [100]. This phenomenon deals with the absorption or emission of signals at specific relaxation times when magnetizing nuclei of materials, e.g., the human head, with strong fields. These times are based on the relaxation phenomenon upon which nuclei of the material will emit energy when returning to the initial position [100]. Two important timings exist for capturing MRIs. The first is T1 or longitudinal relaxation time, which is the time needed for the protons of nuclei to return to its equilibrium in longitudinal (along the main magnetic field) direction [100]. Based on different T1 times, a T1w can be obtained using short repetition (TR) and echo (TE) times. In T1w MRI tissues can be sorted from brighter to darker as WM (short T1 relaxation time), GM (longer T1) and CSF (longest T1) (see Figure 3.3a, upper row). The second is the T2 or the transverse relaxation time which is the time needed for the spinning moments to become out of phase due to the effects of nearby proton (spin-spin interaction) [100]. Using T2 times, a T2w MRI is captured with longer TR and TE than using T1 times. In these images the tissues from brighter to darker are CSF or skull spongiosa (long T2 relaxation time), GM (shorter T2) and WM (shortest T2) (see Figure 3.3a, bottom row). Specific details about these times are described in Chapter 3.

For obtaining brain or WM conductivity anisotropies, diffusion-tensor MRI (DT-MRI) is necessary. DT-MRI relies on the measuring of the water diffusion of molecules by sending two consecutive gradient pulses. The first pulse is to dephase and the second one to rephase the spins of the protons. This results in almost no attenuation at the received signals if the spins (protons) do not move between the two pulses. However, if the spins move after

the dephasing pulse then the perfect rephasing cannot occur (because the rephasing signal differs with spatial position) and measured signals are attenuated. Based on this idea, if multiple diffusion weighted images with varying directions are measured (see Section 3.1.4), they can be combined to obtain the diffusion tensors (see Figure 3.3b).

2.6 Transcranial Electric Stimulation

2.6.1 Basis of TES

As a brain stimulation technique, transcranial electric stimulation (TES) is applied to non-invasively manipulate the neuronal resting-state membrane potentials [101, 102]. Many hypotheses have been introduced to uncover the underlying mechanisms of TES but the process is still not clear. The effects might be due to an interplay of several different mechanisms, for example, induction of changes in the resting membrane potentials or modification of synaptic microenvironment (e.g. synaptic strength of N-methyl D-aspartate receptor, γ - Aminobutyric acid activity) [101]. TES has become widely useful for modulating neural activity not only in healthy subjects but also in patients with epilepsy [20].

The most common way to apply TES in a cortical region of interest (ROI) is to attach two large patches to the skin, with the active patch (anode) to be located above the presumed target region. However, this placement creates broad cortical current flows, that affect the non-target areas and restricts the control of the current intensity in the target region [103, 104]. Recently, Karsten et al. [105] showed that the variability of the electric stimulation effect was significantly predicted by the reconstructed electric field variability in occipital areas, highlighting the importance of individualizing stimulation protocols. Individually targeted and optimized multi-channel TES montages are thus promising in a sense that focal, directed and/or intensive currents can be induced in the target region, minimizing the excitability effects of the non-target cortical areas [56, 103]. These montages are dependent on the target vector of specific location and orientation based on EEG/MEG source analysis [102, 105, 106] and the current dose safety constraints to the electrodes [107]. In this thesis, investigations are carried out about the importance of individually targeting the P20/N20 component using different stimulation types (Section 2.2.3).

TES is also emerging as a valuable neurotherapeutic intervention for suppressing seizures in focal epilepsy [19, 20]. Recently, it was also reported that the efficacy of TES strongly depends on head modeling simplifications (tissue compartment homogenizations and use of standard skull conductivities) [12, 104, 108]. The latter could possibly account as a strong factor of the reported inconsistent effects in focal epilepsy [20]. Thus, in this thesis, head model simplifications were performed to investigate the influence on the individually targeted and optimized multi-channel TES of a focal epilepsy case.

2.6.2 TES Forward Problem

The TES forward problem is related to the EEG forward problem based on the Helmholtz's principle of reciprocity [56]. According to this principle, in a given head domain Ω , a source at position x_{source} and a sink at position x_{sink} are generating a source that can be represented as a mathematical dipole \mathbf{J}_p with amplitude \mathbf{J}_{pA} as following:

$$\mathbf{J}_p = \mathbf{J}_{pA} \delta(x_{source} - x_o) - \mathbf{J}_{pA} \delta(x_{sink} - x_o) \quad (2.27)$$

Then, on the boundary of the head domain Γ , a current density \mathbf{J} with amplitude \mathbf{J}_A is introduced and removed at locations x_{in} and x_{out}

$$\mathbf{J} = \mathbf{J}_A \delta(x_{in} - x_o) - \mathbf{J}_A \delta(x_{out} - x_o) \quad (2.28)$$

The resulting potential fields are directly related

$$\mathbf{J}_{pA} [\phi_2(x_{source}) - \phi_2(x_{sink})] = \mathbf{J}_A [\phi_1(x_{in}) - \phi_1(x_{out})] \quad (2.29)$$

where ϕ_1 and ϕ_2 are the potential field generated by the volume current source \mathbf{I} and the surface current density \mathbf{J} , respectively.

When the amplitude of the current source \mathbf{J}_{pA} is identical to the amplitude of the current density \mathbf{J}_A , the potential difference $\phi_2(x_{source}) - \phi_2(x_{sink})$ is identical to the potential difference between $\phi_1(x_{in}) - \phi_1(x_{out})$. Otherwise, the ratio is directly given by the ratio of the current source and the surface current density.

Based on the above reciprocity, the quasi static approximation to Maxwell's equations for computing the electric potential is justified [56], and from the equation 2.18 the Laplace equation yields:

$$\nabla \cdot (\sigma \cdot \nabla \phi) = 0 \quad (2.30)$$

with inhomogeneous Neumann boundary condition

$$n \cdot (\sigma \cdot \nabla \phi) = \mathbf{I} \quad \text{on} \quad \Gamma = \partial\Omega \quad (2.31)$$

with σ being the conductivity tensor, \mathbf{I} the applied current pattern at the electrodes with non-zero values only at the electrodes, n being the outward normal vector at the surface Γ and ϕ the electric potential. The inhomogeneous Neumann boundary conditions are at the two given positions, x_{in} and x_{out} considering that an active electrode is at the position x_{in} for injecting the current \mathbf{I} to a ground electrode at the position x_{out} [56].

For a numerical approximation of the equation 2.30, FEM can be used (as explained in Section 2.4.3) with on the basis of realistic head volume conductor modeling and the use of algebraic multigrid preconditioned conjugate gradient solvers as well as FEM transfer matrix approaches [56].

3 Experimental and Modeling Effects on the Source Analysis of Somatosensory P20/N20 Component

In this chapter, an EEG/MEG source analysis group study for the reconstruction of the somatosensory P20/N20 component and the individual TES targeting was performed investigating the reconstruction sensitivity of the following experimental conditions and modeling parameters:

- Three different experimental conditions (EW, BT and PT).
- Three different modalities (EEG, MEG and EMEG).
- Different individual high resolution three-compartment isotropic (3CI) or six-compartment brain anisotropic (6CBA) head volume conductor models with standard or individually calibrated skull conductivity.
- The interplay of some of those parameters were also investigated.

Through this study, the experimental and modeling pipeline used in this thesis is described. Subsequently, after the description of a new quasi automatic pipeline for the generation of head models with different detail and the estimation of calibrated skull conductivity, all influences were putted side-by-side with regard to changes in source location, orientation and strength within source reconstruction. Influences on the individual optimized TES montages were also presented. Results from this chapter were recently published in [97].

All figures presented herein were created with custom MATLAB codes, FSL¹, Paraview², Scirun³ and CURRY 8⁴.

3.1 Material and Methods

3.1.1 Participants and Ethics Statement

Five right-handed subjects (32 ± 8.8 years of age; 2 females) participated in this study. All subjects of the present study signed written consent forms for all measurements that have

¹<http://www.fmrib.ox.ac.uk/fsl>

²<https://www.paraview.org/>

³<http://www.sci.utah.edu/cibc-software/scirun.html>

⁴<https://compumedicsneuroscan.com/products/by-name/curry/>

been approved by the ethics committee of the University of Erlangen, Faculty of Medicine on 20.02.2018 (Ref No 4453 B).

3.1.2 EEG and MEG Acquisition

In this thesis, EEG and MEG recordings were simultaneously acquired in a magnetically shielded room using 80 AgCl sintered ring electrodes (EASYCAP GmbH, Herrsching, Germany, 74 EEG channels plus additional 6 channels to detect eye movements) and a whole head MEG system with 275 axial gradiometers and 29 reference sensors (OMEGA2005, VSM MedTech Ltd., Canada). For the detection of cardiac activity, electrocardiography (ECG) was additionally measured. The MEG reference coils were used to calculate first-order synthetic gradiometers to reduce the interference of magnetic fields originating from distant locations. Prior to the measurements, the electrode positions of the EEG cap were digitized using a Polhemus device (FASTRAK, Polhemus Incorporated, Colchester, Vermont, U.S.A.). Moreover, during the acquisition the head position inside the MEG was tracked via three head localization coils placed on nasion, left and right distal outer ear canal. Before the measurements, the electrode positions of the EEG cap were digitized using a Polhemus device (FASTRAK, Polhemus Incorporated, Colchester, Vermont, U.S.A.). All measurements were done in supine position to reduce head movements and to prevent CSF effects due to a brain shift when combining EEG/MEG and MRI [109].

3.1.3 Somatosensory Evoked Potentials and Fields

Somatosensory evoked potentials (SEP) and fields (SEF) were produced by using three different experimental conditions. Those conditions were adopted by using the stimulators presented in Figure 3.1.

The first consisted of stimulating the median nerve at the right wrist (Figure 3.1a) with monophasic square-wave electrical pulses having a duration of 0.5 ms. The stimulus strength was increased until a clear movement of the thumb was visible. This type of stimulation is abbreviated as EW (Electric-Wrist) stimulation in the rest of the thesis.

The remaining two stimulation types used tactile stimulation of the distal phalanx of the right index finger. Pink noise was presented to subjects' ears to mask the acoustic noise caused by both tactile stimulators. The first tactile stimulator was a piezoelectric driven Braille stimulator (Metec GmbH, Stuttgart, Germany), the central 4 out of 8 individually controllable plastic pins grouped in a 2 × 4 array were elevated with a rise-time of 1 ms (Figure 3.1b, left bottom corner). This experimental condition is abbreviated by BT (Braille-Tactile) stimulation in the rest of the thesis. The last type of stimulation, abbreviated by PT (Pneumato-Tactile) stimulation in the rest of the thesis, used a balloon diaphragm driven by bursts of compressed air that was fixed by a plastic spring clip to the right index finger (Figure 3.1c). The delay between the electrical trigger and the arrival of the pressure pulse at the balloon diaphragm was compensated, as well as the delay

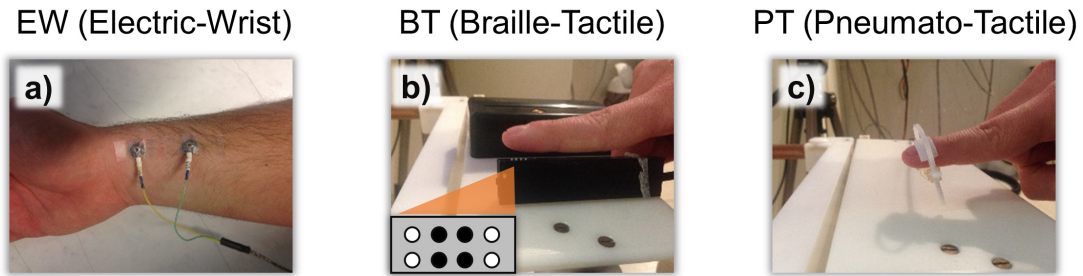


Figure 3.1: The stimulation types: **a)** The EW stimulation type is consisted of two electrodes on the skin of the depicted arm. The distal phalanx of the index finger touches **b)** the BT and **c)** the PT stimulation type. For the BT, the middle four plastic pins (black points in the top view of the stimulator) were used for stimulation of the index finger.

caused by the inertia of the pneumatic stimulation device (half-way displacement of the membrane), which summed up to 52 ms in the present measurements.

The data were acquired with a sampling rate of 1200 Hz and online filtered with a 300 Hz low pass filter. The overall duration of the experiment was 9 minutes, in which 1200 trials were measured for EW and PT and 880 trials for BT. The stimulus onset asynchrony (SOA) varied randomly (350 to 450 ms for EW and PT and 550 to 650 ms for BT) to avoid habituation and to allow clear pre-stimulus intervals for SNR determination.

3.1.4 MRI Sequences

T1-weighted (T1w), T2-weighted (T2w) and diffusion tensor (DT-) MRI scans were acquired with a MAGNETOM Prisma 3T (Release D13, Siemens Medical Solutions, Erlangen, Germany) based on the following setup:

- 3D-T1w fast gradient-echo pulse sequence using water selective excitation to avoid fat shift (TR/TE/FW = 2300/3.51 ms/8°, inversion prepulse with TI= 1.1 s, cubic voxels of 1 mm edge length).
- 3D-T2w turbo spin echo pulse sequence (TR/TE/FA = 3200/408 ms/90°, cubic voxels, 1 mm edge length).
- DT-MRI using an echo planar imaging sequence (TR/TE/FA = 9500/79 ms/90°, cubic voxels, 1.89 mm edge length).
- One volume with diffusion sensitivity $b = 0 \text{ s/mm}^2$ (i.e., flat diffusion gradient) and 20 volumes with $b = 1000 \text{ s/mm}^2$ in different directions, equally distributed on a sphere. An additional volume with flat diffusion gradient, but with reversed spatial encoding gradients was scanned and utilized for susceptibility artifact correction [75].

During T1w MRI measurement, gadolinium markers were placed at the same nasion, left and right distal outer ear canal positions for landmark-based registration of EMEG to MRI.

3.1.5 Processing of Somatosensory Evoked Responses

The raw EMEG recordings were filtered between 20 to 250 Hz applying a digital band pass filter with a Hann window in CURRY 8. A notch filter was used to eliminate interferences caused by 50 Hz power line frequency and its harmonics. Subsequently, the preprocessed recordings were separated into equally large segments of 300 ms (100 ms pre and 200 ms post stimulus onset). After visually rejecting the bad channels, reduction of non-cerebral activity was performed based on a threshold-based semi-automatic procedure which is offered in CURRY 8 followed by visual inspection of the candidate bad trials in each modality. Epochs with SNR higher than the selected threshold were then excluded. The threshold was determined empirically. The SEP/SEF responses were then determined as the average across all trials excluding in average 50 trials per subject and stimulation type.

3.1.6 Processing of Image Data

T1w and T2w MRI were used to construct individual six-compartment (6C: scalp, skull compacta (SC), skull spongiosa (SS), CSF, GM, and WM) head models and three-compartment (3C: scalp, skull, brain) and. The standard low-parametric isotropic 3C volume conductor model is still frequently used in source analysis [2]. It is therefore instructive to compare the results derived based on 6C and 3C head models.

The first module of the quasi-automatic segmentation pipeline started with the segmentation of the T1w MRI into scalp, brain (bm_T1) and the three brain tissues CSF, GW and WM using SPM12⁵ embedded in the FieldTrip toolbox [110]. Subsequently, the T2w MRI was registered to the T1w dataset (T2w_T1wSpace) using a rigid registration approach and mutual information as a cost-function as implemented in FSL. T2w_T1wSpace was then used for the segmentation of SC, CSF (CSF_T2) and brain (bm_T2). SS was segmented based on Otsu thresholding [111] upon the so-called *masked* T2w_T1wSpace images by the 2 mm eroded SC images (i.e. logic operator *AND* between T2w_T1wSpace and the eroded SC).

All the segmented tissues were then imported into a second module for structuring the final segmented model. The first step was to ensure no overlap of GW and WM with the SC mask. Then, CSF was masked (mCSF) using first bm_T2 and CSF_T2 and then GW and WM, also to avoid overlap. Unrealistic holes within the masks were detected and filled using the *imfill* function in MATLAB. A combination of region detection algorithm (*bwconncomp* and *regionprops* in MATLAB) and thresholding was used to avoid unrealistic segmentations

⁵<http://www.fil.ion.ucl.ac.uk/spm/software/spm12/>

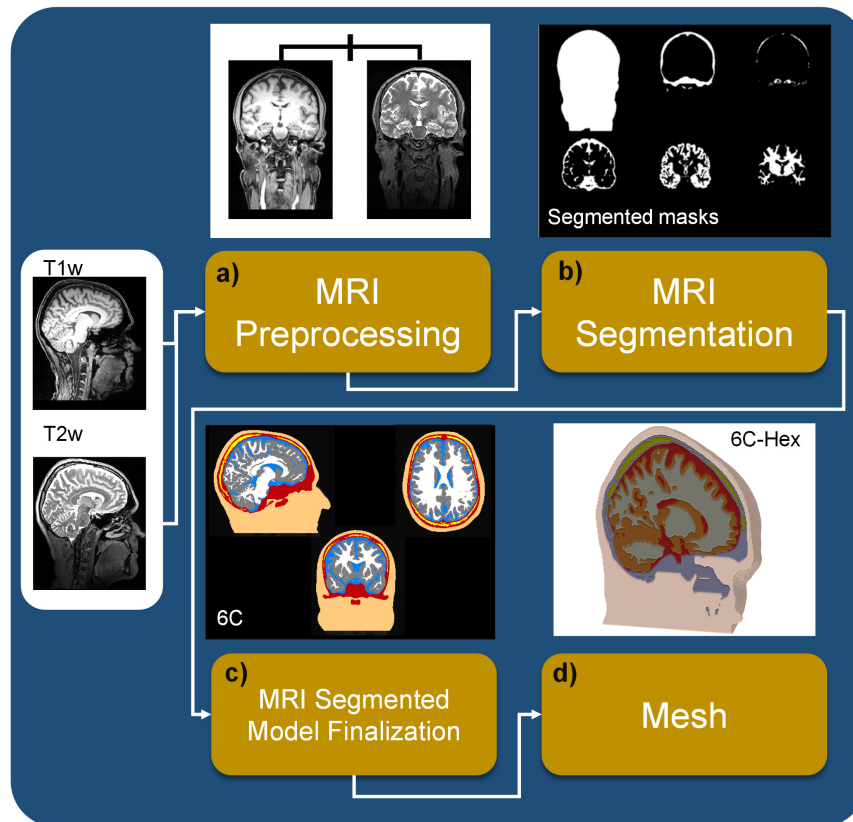


Figure 3.2: Segmentation pipeline with T1w and T2w MRIs for creating a six-compartment head model: The main image processing and visualization modules are **a)** the preprocessing of T1w and T2w MRIs (e.g. registration); **b)** the segmentation of six-compartment (6C) tissues (skin, skull compacta, skull spongiosa, CSF, gray and white matter) follows; **c)** the post-processing of the segmented masks is performed for the final 6C segmented head model; **d)** the generation and visualization of the 6C hexahedral head model (6C-Hex). MRI visualizations were done with FSL toolbox while the surfaces with FieldTrip toolbox.

after the matching of the masks. The final segmentations were visually inspected to ensure there were no errors. To avoid an unnecessary amount of computational work and without losing accuracy, each model was restricted along an axial plane 40 mm below the skull (in average across all subjects), following the recommendations of [80]. Finally, the 3C head model was generated by merging SC and SS into skull and mCSF, GM and WM into the brain compartment. An illustration of the quasi-automatic segmentation pipeline is presented in Figure 3.2.

The DTI data were processed to reduce the eddy current and non-linear susceptibility artifacts using FSL and the subroutine HySCO⁶ from the SPM12 toolbox. Diffusion tensors were then calculated and transformed into WM and GM conductivity tensors by an effective medium approach [74]. These tensors were later included into the head model to account for WM and GM tissue conductivity anisotropy. An explanation about the effective medium

⁶<http://www.diffusiontools.com/documentation/hysco.html>

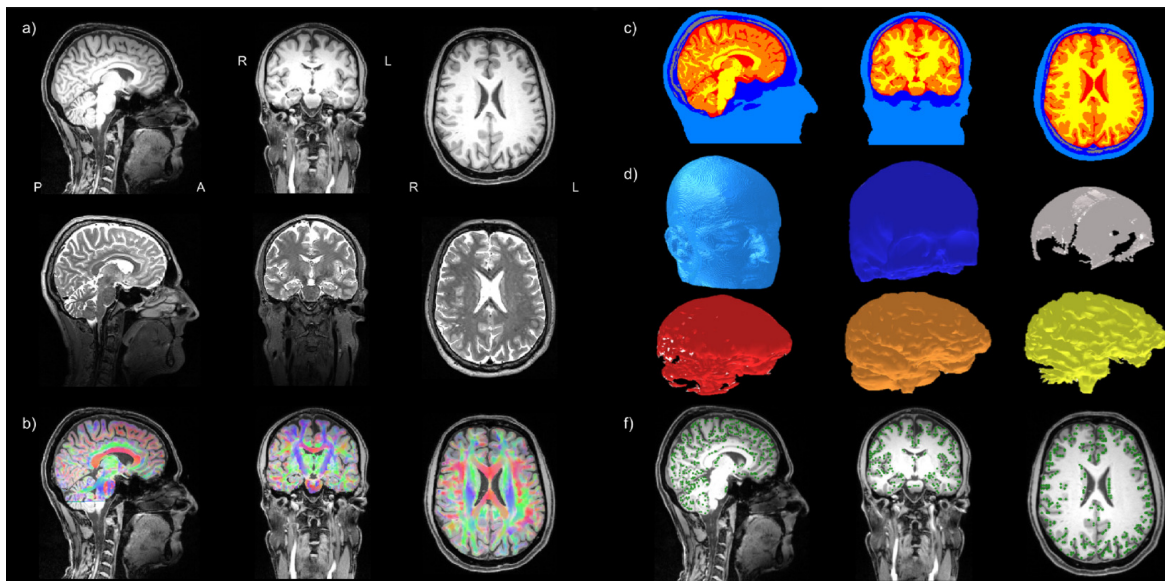


Figure 3.3: Six compartment anisotropic realistic head model and source space: The left subfigure shows sagittal (left column), coronal (middle column) and axial (right column) slices of **a)** T1w (upper row) and T2w (middle row) MRIs and **b)** a color-coded (red for left-right; green for anterior-posterior; blue for superior-inferior) fractional anisotropy map computed from the registered DTI and plotted on the T1w MRI (lower row); **c)** the 6-compartment segmentation result with scalp (light blue); skull compacta (dark blue); skull spongiosa (gray); CSF (red); gray matter (orange) and white matter (yellow); **d)** the geometry-adapted hexahedral FEM mesh for each of the 6 tissue compartments; **f)** the source space nodes (green dots) on T1w MRI. The MRI visualizations were done with FSL toolbox while the surfaces with custom MATLAB codes.

approach follows in the next section.

The resulting segmentation and DTI processing are visualized exemplarily for one of the subjects in Figure 3.3. Sagittal (left column), coronal (middle column) and axial (right column) slices of T1w (upper row) and T2w (lower row) MRIs are shown in Figure 3.3a. Figure 3.3b presents a color-coded fractional anisotropy map that was computed from the registered DTI and plotted on the T1w MRI. Figure 3.3c shows the 6-compartment segmentation result with scalp (light blue), skull compacta (dark blue), skull spongiosa (gray), CSF (red), GM (orange) and WM (yellow).

3.1.7 Calibrated Realistic Head Volume Conductor Models

In this step, using the labeled volumes with 1 mm resolution of Section 3.1.6, geometry-adapted hexahedral finite element (FE) meshes of 1 mm mesh size were constructed for each subject using SimBio-VGRID⁷ [51, 56]. The adaptation was calculated using a node-shift of 0.33 ensuring that the interior angles at element vertices were convex and the Jacobian determinant in the FEM computations remained positive. This approach increased the

⁷<http://vgrid.simbio.de/>

conformance to the real geometries and mitigated the effects of the staircase-like segmented voxel meshes. The results are six-compartment head models with brain tissue anisotropy (6CBA). The resulting geometry-adapted hexahedral FEM meshes for each of the 6 tissue compartments are presented in Figure 3.3d.

In average over the 5 subjects used in this study, these FEM meshes had 3,487,282 nodes and 3,396,950 elements. For the purpose of this study, 3CI head volume conductor models are built.

3.1.7.1 Head Tissue Conductivities

For each subject, the conductivity values were 0.43 S/m for scalp [112], 1.79 S/m for CSF [96] for all head models created in this thesis. The conductivity of the homogenized brain compartment was 0.33 S/m in the 3CI head models [3, 113]. In the 6CBA head models, the procedure is described in the next Section 3.1.7.2 to determine anisotropic conductivity tensors for the compartments GM and WM. As described in Section 3.1.7.3, individual skull conductivity parameters were estimated for the 3CI and 6CBA models resulting in 3CI_Cal and 6CBA_Cal, respectively. Standard head models were generated with literature-based skull conductivity of 0.0041 S/m for 3CI_41 and 0.0041 S/m for the SC and 0.0148 S/m for the SS compartments for the 6CBA_41 head models following [3, 44, 113]. The value 0.0041 S/m is also implemented as standard skull conductivity in commercial source analysis packages (see, e.g., [3]). Thereby, the chosen 6CBA_41 skull conductivities furthermore use a fixed ratio for SC:SS of about 1:3.6 [9].

3.1.7.2 The Effective Medium Approach for Brain Anisotropy

An important step for including brain anisotropy is to convert water diffusion tensors obtained via diffusion tensor imaging to conductivity tensors. Following the studies [5, 74, 99], the effective medium approach was used. This approach assumes a linear relationship between the conductivity σ and the water diffusion tensor DT as shown below

$$\sigma = \frac{\sigma_e}{d_e} \cdot DT \quad (3.1)$$

In this equation the ratio between the effective extracellular conductivity (σ_e) and the diffusivity (d_e) can be considered as a scaling factor sf . The sf was calculated with the assumption that the arithmetic mean of the anisotropic conductivity tensor volume is the same as the tensor volume when the isotropic conductivity is assumed. Thus, sf was estimated with a least squares fit, which ensures that the conductivity tensor volumes in the tissue of interest match the volume of the corresponding tensor with isotropic conductivity as follows

$$\frac{4\pi}{3} (\sigma_{ts}^{iso}) = \frac{\sum_{i=1}^{N_{ts}} \frac{4\pi}{3} \prod_{j=1}^3 \sigma_{\iota}^j}{N_{ts}} \quad (3.2)$$

where σ_{ts}^{iso} is the isotropic conductivity for the tissue compartment ts which is assigned either to WM or GM and N_{ts} is the number of conductivity tensors. By replacing the j^{th} eigenvalue of the i^{th} conductivity tensor σ_i^j with $sf \cdot d_i^j$ (the j^{th} eigenvalue of the i^{th} diffusion tensor) and $\frac{\sum_{i=1}^{N_{ts}} \prod_{j=1}^3 sf \cdot d_i^j}{N_{ts}}$ with d_{ts} , the equation 3.2 is simplified to:

$$\frac{4\pi}{3} (sf \cdot d_i^j)^3 \quad (3.3)$$

Finally sf can be calculated with following equation:

$$sf = \frac{d_{WM}\sigma_{WM}^{ISO} + d_{GM}\sigma_{GM}^{ISO}}{d_{WM}^2 + d_{GM}^2} \quad (3.4)$$

3.1.7.3 Two-level Individual Skull Conductivity Calibration

In this thesis, skull conductivity is individually modeled by extended a calibration procedure that benefits from the different sensitivity profiles of EEG and MEG (algorithm 2 in [44]). While the procedure in [44] only uses a single resolution level, a refine of two resolution levels is proposed, resulting into the following three steps procedure. The EW type was used on the calibration, because of its highest SNR and sharp P20/N20 peak when compared to BT and PT. Figure 3.4(b and c) depict exemplarily the artifact-corrected SEP and SEF scalp topographies of the P20/N20 component for one of the subjects.

Step 1 (source localization): While individual skull conductivity has a considerable influence on the P20/N20 SEP source reconstruction, it hardly influences source analysis of the SEF component at 20 ms post-stimulus [2, 76]. Therefore, using a dipole scan approach [3, 114] throughout the whole source space and a head model with the standard skull conductivity parameters 1.6 mS/m for SC and 5.76 mS/m for SS [9], the SEF data are exploited to accurately localize the peak at 20 ms post-stimulus. The single dipole scan assumes that its generator is focal and single-dipolar [25, 26, 27, 115]. The main goal of the dipole scan is the determination of the source for which the residual variance (RV) between the measured and the simulated SEF data at 20 ms post-stimulus is minimal. Furthermore, the dipole scan is regularized accordingly to suppress the amplification of high-frequency spatial noise into erroneously high radial dipole orientation components within the inversion procedure [3, 49]. This source location is then fixed as the outcome of step 1 and will no longer be modified by the next two steps of our calibration procedure.

Step 2 (coarse resolution calibration): The coarse resolution level uses the predefined set of skull compacta conductivity values $SC = [0.8, 1.6, 2.4, 2.8, 3.3, 4.1, 5.5, 7, 8.3, 16.5, 33]$ mS/m. These values were selected based on [44] including the additional value of 0.8 mS/m [7]. The ratio of SC:SS is fixed to 1:3.6 [9, 79]. Therefore, the skull conductivity calibration includes only one degree of freedom, namely the SC conductivity, to avoid overfitting due to a too high number of degrees of freedom [29, 86]. The following steps compensate for the insensitivity of MEG to quasi-radial source components: For the fixed

source location of step 1 and an SC value out of the above predefined coarse resolution set, the dipole orientation and strength with the lowest RV to the measured SEP and SEF components at 20 ms post-stimulus are determined. The RV to the SEP data as output value is then stored. These steps are repeated for all values of the coarse resolution level, resulting in a coarse resolution calibration curve, for which minimum is then finally selected as the coarse level calibration optimum.

Step 3 (fine resolution calibration): A finer resolution level for SC calibration conductivity is now produced around the coarse level calibration optimum of step 2 and the new RV minimum is determined as in step 2. Thereby, our two-level procedure helps to reach an even lower residual variance to the simultaneously measured SEF and SEP P20/N20 peaks.

3.1.8 Source Spaces

For each subject participated in this thesis (including the present study), a 2 mm resolution source space in the center of the GM compartment without restrictions to source orientations (no normal-constraint) was constructed. This ensured that all sources were located inside GM and sufficiently far away from the neighboring tissue compartments to fulfill the so-called *Venant* condition, i.e., for each source node, the closest finite element node should only belong to elements, which are labeled as GM. It must be fulfilled to avoid numerical problems and unrealistic source modeling for the chosen Venant dipole modeling approach [5, 54]. Figure 3.3f shows the resulting source space on the T1w MRI in the GM compartment which closely follows the folding of the cortex.

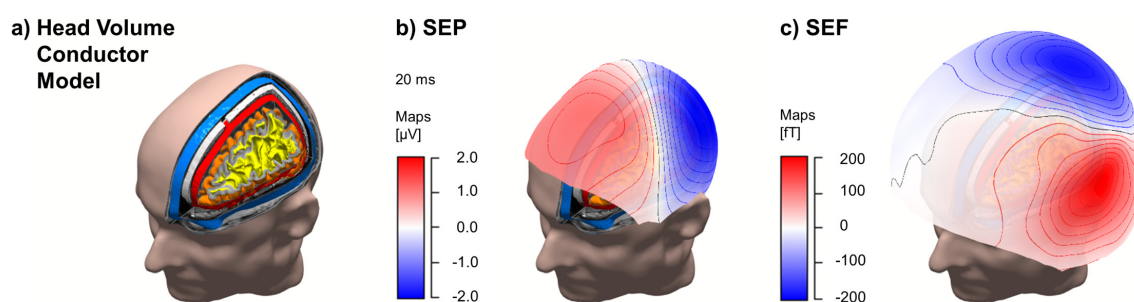


Figure 3.4: The main ingredients for the skull conductivity calibration procedure: a) the individual high-resolution head model with six-compartments (skin (human light skin color); skull compacta (blue) and spongiosa (gray); CSF (red); gray matter (orange) and white matter (yellow)), **b** and **c**) iso-potential and field lines of the bipolar scalp topographies for the SEP and SEF at 20 ms post stimulus (the P20/N20 component) for one of the subjects. The present visualizations were done in CURRY 8.

3.1.9 EEG and MEG Forward Solutions

All forward solutions in this thesis and the present study, including those of Section 3.1.7.3, were calculated using FEM because of its flexibility with regard to complex geometries and tissue anisotropies [14, 116, 117, 118, 119]. For the forward computations, the Venant direct source modeling approach were used due to its high numerical accuracy and high computational efficiency when used in combination with EEG and MEG transfer matrices and an algebraic multigrid preconditioned conjugate gradient (AMG-CG) solver [57]. Standard piecewise trilinear basis functions were furthermore used in an isoparametric FEM framework [51]. An implementation was adopted by the SimBio⁸ software.

As shown by [57], the used FEM forward computations have linear complexity with the number of nodes when using transfer matrices in combination with the AMG-CG solver. AMG-CG was shown to significantly reduce the solution time when compared to simpler solver approaches [58, 121] and to be stable towards modeling of tissue inhomogeneity and anisotropy [122]. Overall, per subject, the whole skull conductivity calibration process and the leadfield calculations for EEG and MEG for 6CBA head modeling needed 15h and 15min on average across all subjects using a standard laptop (Dell, XPS15, 2016), i.e., an overnight computation job per subject.

3.1.10 EEG and MEG Inverse Solutions

Based on the assumption that the generator is focal and single-dipolar [3, 25, 26], the algorithm, single dipole scans (SDS) (see Section 2.4.5), was performed to estimate the P20/N20 sources [3, 49] for each measurement modality (EEG, MEG, EMEG) for all studies of this thesis. The locations were expected being in the primary somatosensory cortex in Brodmann area 3b. Pure MEG dipole scans were regularized in order to suppress the influence of spatially high frequent data noise that might otherwise be amplified into too high radial dipole orientation components [3, 49]. No regularization was applied for single modality EEG or combined EMEG source reconstructions. For EMEG, since both modalities have different units and residual variance is expressed as the sum of the squared difference over all channels, both need to be transferred to common units. Here, the SNR based transformation as suggested by [3] was applied in order to perform EMEG source reconstruction. In this method, the data were whitened according to the noise level (calculated from the pre-stimulus interval) of each channel so that unit-less measures for EEG and MEG were obtained to be used in a combined analysis.

⁸SimBio: https://www.mrt.uni-jena.de/simbio/index.php/Main_Page and its integration into FieldTrip (see [120])

3.1.11 Multi-channel TES Targeting and Optimization

For the optimization of each multi-channel TES montage used in this thesis, the available electrode setup was a neoprene multi-channel array of $M = 39$ possible positions (Starstim TES system, Neuroelectronics, Barcelona, Spain), ordered in 10/10 EEG positioning system. The sensor positions of this cap were digitized with a Polhemus measurement device. The specific device had available eight electrodes for applying TES in the target region-of-interest.

The general goal in TES optimization is to find an optimally targeting electrode montage for the given individual target $e \in \mathbb{R}^{3N_\Omega \times 1}$ on the volume conductor head model (Ω with N_Ω nodes). For this purpose, the superposition principle for a linear combination of all possible current injection patterns from the TES can be the following

$$e = K \cdot s \quad (3.5)$$

where $K = [K_1, \dots, K_{M-1}]$ is the influence matrix and $\mathbf{s} = [s_1, \dots, s_{M-1}]$ is the vector of injected currents. For estimating each element $K_i \in \mathbb{R}^{3N_\Omega \times 1}$ of K , the last electrode serves as a reference (s_{ref}). The final number of pairs of surface electrodes is $M - 1$. Each element K_i is equal to $(\sigma \cdot \nabla \phi_i)$ (Section 2.6.2, equation 2.30) and it is approximated with the Adjoint method [56]. This method utilizes numerical approximations of the potential using AMG-CG solvers (see Section 3.1.9).

Given a set of $M - 1$ possible electrodes in combination with the reference electrode $s_{ref} = -\sum_{i=1}^M s_i$, i.e., $\tilde{\mathbf{s}} = [s_1, \dots, s_{M-1}, s_{ref}]^T$, a safety constrain of a total induction current $s_{Total} = 2$ mA [107] and a subset of K at the target area, K_e , optimization TES algorithms with different side-constrains were used to estimate the final set of optimal currents s_{opt} as described in the following Sections 3.1.11.1 and 5.1.7.

3.1.11.1 Constrained Maximum Intensity

In the present study, the constrained max intensity (CMI) [123] was selected for TES optimization. As an extended version of the maximum intensity approach [103], CMI offers higher flexibility on distributing the injected currents over multiple electrodes compared to the maximum intensity approach which always results into a bipolar optimized electrode montage of a positive (anode) and a negative (cathode). The ability of CMI on distributing current over many electrodes allowed a reduction of the current amplitude at each electrode and thereby could enable an easier realization of the sham condition in real applications. This could be achieved based on an additional regularization with a parameter λ , with which more than one anodes and cathodes could be selected.

CMI is stated as follows

$$s_{opt} = \max_s e^T K_e s - \lambda \|\tilde{s}\|_2 \quad (3.6)$$

$$\text{subject to } \|\tilde{s}\|_1 \leq 2s_{Total} \text{ and } \|\tilde{s}\|_\infty < s_{Limit}$$

where λ controls the current distribution and the term s_{Limit} was added to limit the maximum amount of current injected or extracted by each stimulation electrode and it was equal to 1.5 mA. The parameter λ was estimated based on an iterative procedure in a way that eight electrodes will be used. The iterative procedure involved the application of the CMI algorithm for different λ values. In each iteration, the λ parameter was increased by a factor of ten from zero up to thousand and the CMI algorithm was executed to define the new s_{opt} . The iterative procedures stopped when the number of the optimization electrodes was equal to eight.

A comparison of the CMI approach with the two-patch stimulation approach is applied. The two-patch approach was one of the first attempts for stimulating specific brain regions as introduced first by [101]. Therefore, it is instructive to compare stimulation results derived by the CMI and two-patch stimulation approach. In order to use the two-patch optimization approach, a simulation was applied using two 5 cm x 5 cm sponge-like TES patches with thickness 4 mm and saline-fluid like conductivity of 1.4 S/m [104]. The patches were located around the C3 (anode) and FP2 (cathode) electrode locations which is considered as a standard setup as present in [101]. The two electrode positions were used from the digitized Polhemus TES cap measurement as explained in subsection 3.1.11. The patches were applied with a total injected current of 2 mA.

The comparison of the CMI and two-patch TES approaches is quantified by using the TES quality indices INT (intensity in the non target region ($INT = \frac{\int_{\Omega \setminus \Omega_t} |K_e s| dx}{|\Omega \setminus \Omega_t|}$) and directionality ($DIR = \frac{\int_{\Omega} (K_e s, e) dx}{|\Omega_e|}$) in the target region) as introduced in [104].

Furthermore, the quality of the effect of the stimulation types on TES optimization is quantified based on the metric ‘‘half-max radius’’ [103] that the focality of induced current in the target region. For this metric, it is first needed to define the quantification of electric field magnitude contained within a sphere of increasing radius around the target as follows:

$$F(r) = \frac{\sum_{N_{\Omega} \in \Omega_e} \|e\|}{\sum_{N_{\Omega} \in \Omega} \|e\|} \quad (3.7)$$

where Ω_e is a set of N_{Ω} nodes within the radius r at the target node. Then, the half-max radius was defined as the radius which contained the half of the total electric field

$$r_{0.5} = r | F(r) = 0.5 \quad (3.8)$$

The observation of the $r_{0.5}$ for a specific target intensity could characterize the ability of CMI to yield focal electric fields across a range of subjects.

3.2 Results

3.2.1 Experimental and Modeling Pipeline

The data acquisition and analysis pipeline developed in the present thesis and used in the present study is summarized in Figure 3.5 showing all steps from the raw data up to the source analysis results. T1w, T2w, DTI and combined SEP/SEF elicited by the three different somatosensory stimulation types (EW, BT and PT) are shown in the left block (data acquisition). After preprocessing of the structural and functional data, the generated calibrated realistic head models (6CBA_Cal and 3CI_Cal) are then used for source analysis of the P20/N20 components.

The remainder of this section is divided into three parts. The first part presents the individual skull conductivity calibration results for the different head models. The second part describes source localization, orientation and strength differences when using different modalities (EEG, MEG or EMEG), head models (3CI, 6CBA, standard or calibrated) and stimulation types (EW, BT, PT). The last part shows the optimized TES electrode montages when different target vectors due to change in the stimulation type of the most integrative modality (EMEG) and the 6CBA_Cal head model are used.

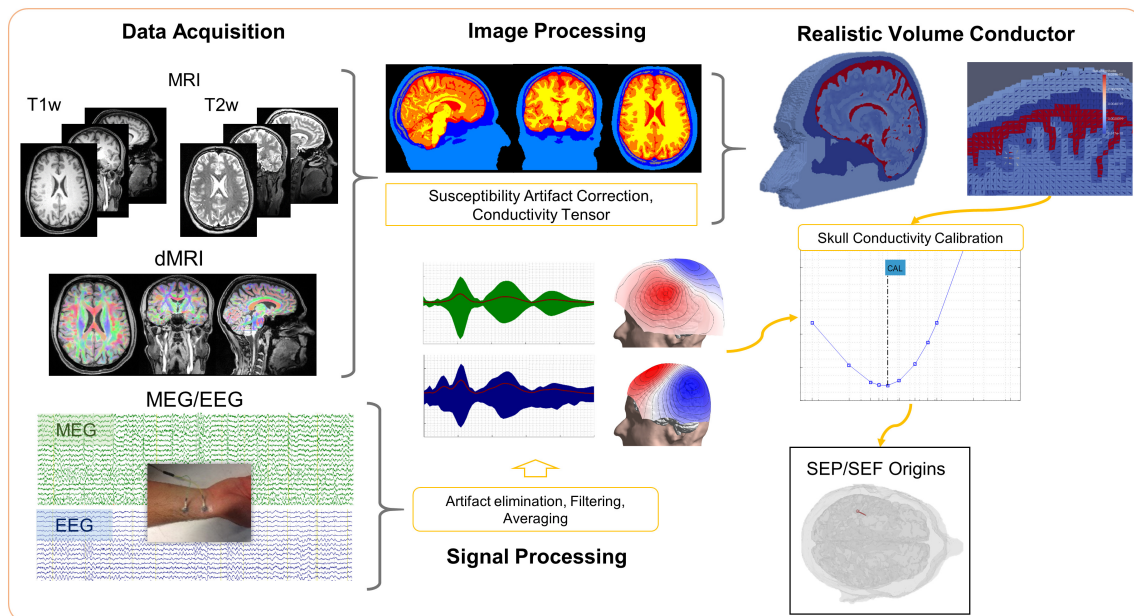


Figure 3.5: Summary of the experimental and modeling pipeline: The data acquisition block shows the MRI datasets (T1w, T2w, DTI) and the combined SEP/SEF data elicited by EW, BT and PT stimulation types. After preprocessing of the structural and functional data, calibrated realistic head models are generated that are then used for source analysis of the somatosensory P20/N20 component. The corresponding software tools used in each step are also indicated.

3.2.2 Individual Skull Conductivity Calibrations

The calibration procedure described in Section 3.1.7.3 was applied to both the 6CBA and 3CI head models resulting into their calibrated variants 6CBA_Cal and 3CI_Cal, respectively, (Table 3.1 and Figure 3.6). For the 6CBA head models, calibrated skull conductivities ranged from 0.0031 S/m and 0.0111 S/m (subject 1, male, age 49) up to 0.014 S/m and 0.0504 S/m (subject 5, female, age 27) for skull compacta and spongiosa, respectively. For 3CI, calibrated skull conductivities were overall lower, ranging from 0.0016 S/m (subject 1) up to 0.0083 S/m (subject 5) for the bulk skull conductivity. Note, that the lower values for 3CI_Cal are a result of the interplay between skull conductivity calibration and the modeling differences in the inner compartments, where 3CI uses a single homogenized brain compartment and 6CBA distinguishes CSF, GM and WM and models tissue anisotropy.

6CBA_Cal and 3CI_Cal are illustrated exemplarily in 3.6 to demonstrate the differences in head volume conductor modeling for one of the subjects (subject 1). Both models are presented using a common color map for the representation of the conductivities. In 6CBA_Cal, note the high conductivity of the CSF compartment and the spread of the maximum norm of the conductivity tensors visualized in the GM and WM compartments, which was due to the procedure described in Section 3.1.7.3. The benefit of the present calibration procedure can be appreciated by studying the sensitivity of combined SEP/SEF source analysis to changes in modality (EEG, MEG, EMEG) or head modeling, as done in the next section.

Table 3.1: Overview of the head models for every subject: First column indicates the subject number, the second one shows the gender of the subject (Male or Female), and the third is about the age (in years). The fourth column indicates the Head Volume Conductor Model (HVCM) and the remaining columns the conductivities for the respective compartment resulting from the calibration procedure described in Section 3.1.7.3. The ratio of skull spongiosa to compacta was kept constant to the mean of the ratio measured by [9] in all 6CBA_Cal HVCM. Sign dash was used for the absence of conductivities for non-distinguished compartments in the corresponding HVCM.

Subject	Gender	Age	HVCM	Skull	SC	SS
1	M	49	3CI_Cal	0.0016	-	-
			6CBA_Cal	-	0.0031	0.0111
2	M	27	3CI_Cal	0.0033	-	-
			6CBA_Cal	-	0.0083	0.0299
3	F	27	3CI_Cal	0.0041	-	-
			6CBA_Cal	-	0.0045	0.0162
4	M	32	3CI_Cal	0.0033	-	-
			6CBA_Cal	-	0.0087	0.0313
5	F	27	3CI_Cal	0.0083	-	-
			6CBA_Cal	-	0.0014	0.0504

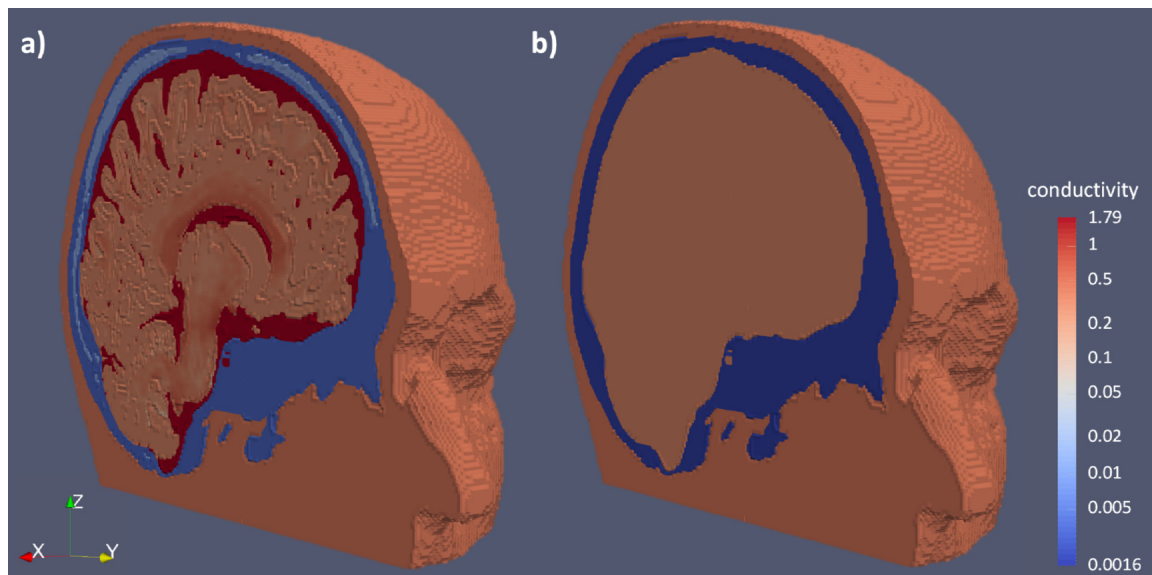


Figure 3.6: Calibrated head models: **a)** Six compartment anisotropic calibrated (6CBA_Cal) head model and **b)** three compartment isotropic calibrated (3CI_Cal) head model. Both models are color-coded (logarithmic scale) according to the conductivity range for subject 1 using a single color-bar. The spread of the maximum norm of the conductivity tensors, visualized in the brain compartments in model 6CBA_Cal, is due to the procedure as described in Section 3.1.7.3.

3.2.3 Effect of Modality, Head Modeling and Stimulation Type on the Reconstruction of the P20/N20 Component

In the following, the sensitivity of the single dipole deviation scans to modality (EMEG, EEG, MEG) and head modeling (6CBA_Cal, 6CBA_41, 3CI_Cal, 3CI_41, see Table 3.1 and Section 3.1.7.3) were tested. The sensitivity was defined in terms of location or orientation differences and strength reduction between pairs of reconstructed sources. For the location differences, the Euclidean distance was employed while the normalized inverse cosine of the inner product between the two underlying source was used for calculating the orientation difference. The strength difference was calculated by the percentage difference between the underlying reconstructed sources.

Figure 3.7 depicts the deviation scan differences for all subjects with regard to source location (left plot), source orientation (middle plot) and source strength (right plot). The stimulation type (EW) was kept constant because of the sharper P20/N20 response and the higher SNR when compared to the other two stimulation types (BT, PT) (see Figure 3.8). For easier comparison of the different effects, Figure 3.7, 3.9 and 3.10 have the same maximum y-axis scaling.

At first, the effect of modality in the source reconstruction of the P20/N20 response was investigated. In Figure 3.7a (upper row), the differences between the source reconstruction of the reference modality (EMEG) and EEG (in blue) and between EMEG and MEG (in yellow) are shown for the most detailed head model 6CBA_Cal (left) and the more

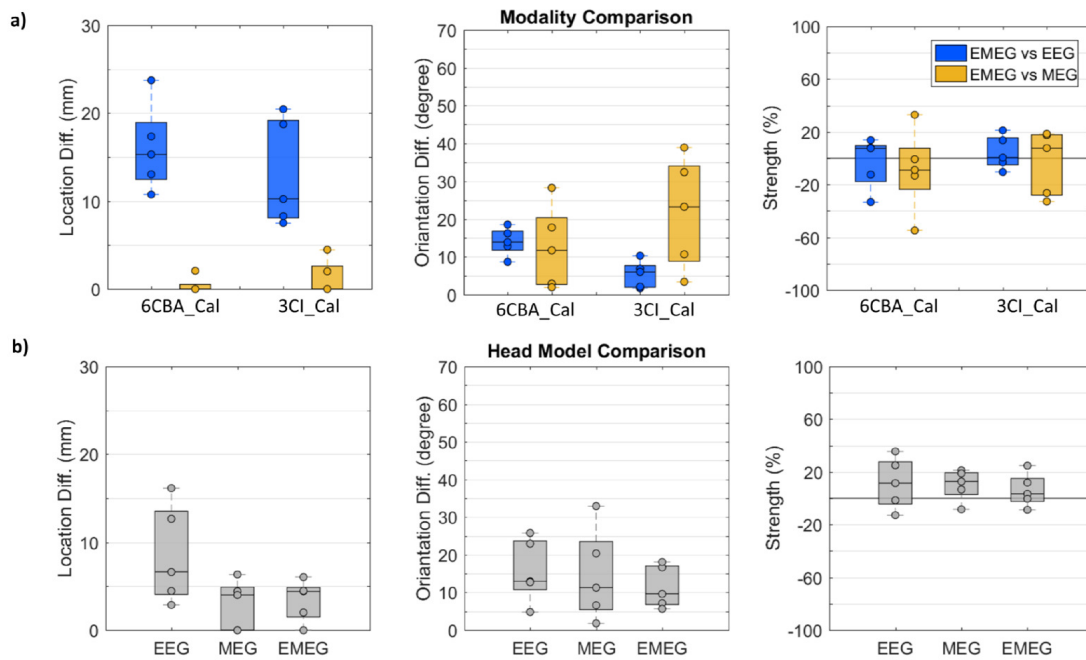


Figure 3.7: EW stimulation: Effect of modality and head model on P20/N20 reconstruction: Single dipole deviation scan differences for all subjects with regard to source location (left plot), source orientation (middle plot) and source strength (right plot). In **a)**, the reconstruction differences are shown when using as a reference the EMEG data versus the data of a single (EEG or MEG) modality for the most detailed head model 6CBA_Cal (left) and the more homogenized version 3CI_Cal (right). In **b)**, the reconstruction differences are presented when using as a reference the most detailed head model 6CBA_Cal versus the more homogenized 3CI_Cal for EEG, MEG and combined EMEG. In each boxplot, the central mark is the median, the edges of the box are the 25th and 75th percentiles. The circles indicate the values for each subject.

homogenized version 3CI_Cal (right). As Figure 3.7a (left plot) shows, with on average 16.1 ± 4.9 mm and 13 ± 6.1 mm largest localization differences can be observed between EMEG and EEG for 6CBA_Cal and 3CI_Cal, respectively (both in blue). The localization results based on EMEG and MEG differed comparably little (< 3 mm and < 5 mm) for both calibrated head models (both in yellow). In contrast to this result, for 3CI_Cal, source orientation differences (middle plot) are on average only $5.4^\circ \pm 3.6^\circ$ between EMEG and EEG (blue), but $21.7^\circ \pm 14.7^\circ$ for EMEG vs MEG (yellow). Larger differences in source orientations were found for 6CBA_Cal having an average of $14^\circ \pm 3.7^\circ$ for EMEG vs EEG (blue), but only $12.5^\circ \pm 10.9^\circ$ for EMEG vs MEG (yellow). Similar source strengths differences (right plot of Figure 3.7a) can be observed having an average of -3.3 ± 19.5 % for 6CBA_Cal and 4.3 ± 12.8 % for 3CI_Cal for EMEG versus EEG (blue) and -8.96 ± 31.4 % for 6CBA_Cal and -3.1 ± 24.6 % for 3CI_Cal for EMEG versus MEG (yellow). Finally, Figure 3.7a also depicts a strong inter-subject variability of the source reconstruction differences that were found for source location, orientation and strength.

Subsequently, the effect of the two different calibrated head models (3CI_Cal or

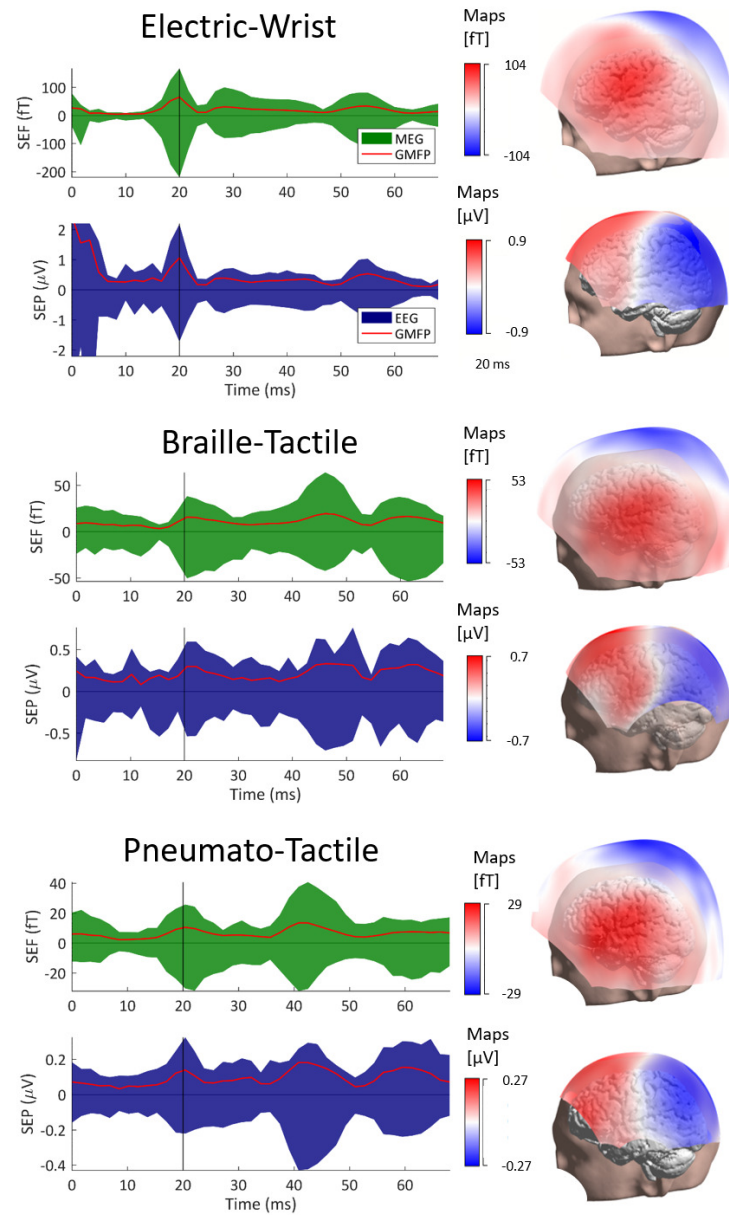


Figure 3.8: Somatosensory evoked fields (SEF) and potentials (SEP) for the three types of stimulation: For the averaged SEF (upper row) and SEP (lower row), butterfly plots with global mean field power (GMFP) (left plot, MEG in green, EEG in blue, GMFP in red) and P20/N20 topographies (right plot) are shown from one subject for each type of stimulation: **a)** EW **b)** BT and **c)** PT. The vertical black line at 20ms in the left plot represents the highest peak of the P20/N20 component for each stimulation type and the EEG and MEG topographies are then shown in the right plot. Note the different amplitudes for the three stimulation types.

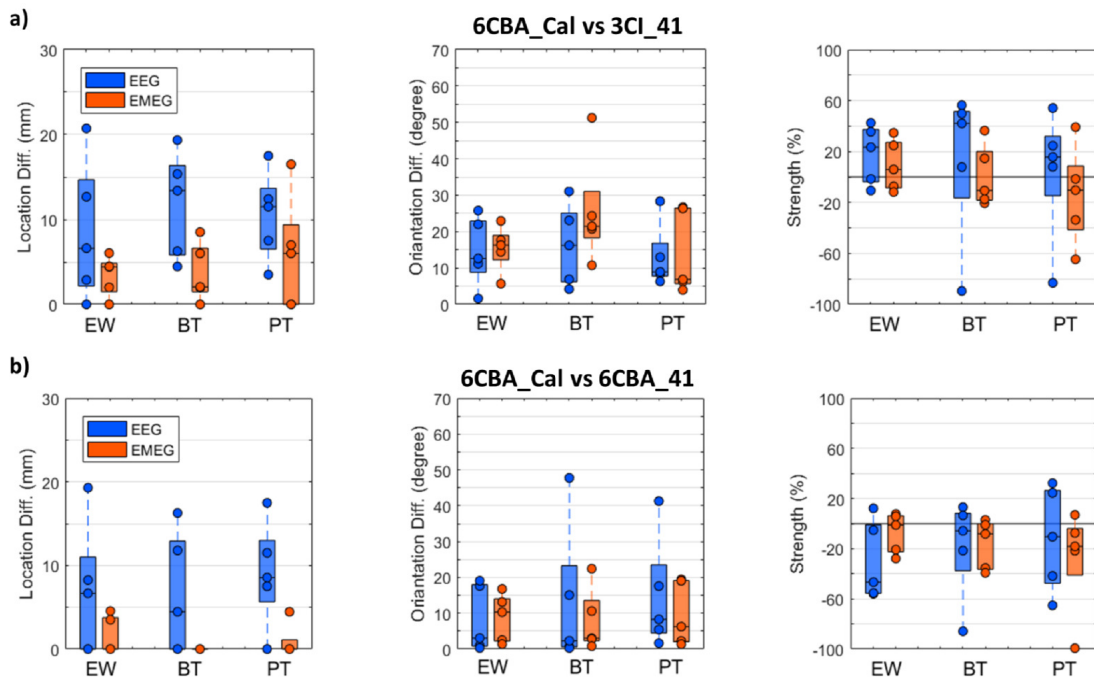


Figure 3.9: Effect of individual head modeling with focus on skull conductivity calibration on P20/N20 reconstruction: Single dipole deviation scan differences for all subjects with regard to source location (left plot, in mm), source orientation (middle plot, in degrees) and source strength (right plot, in %). **a)** Most detailed six compartment anisotropic head model with individually calibrated skull compartment (6CBA_Cal) in comparison to the standard isotropic three compartment model (3CI_41). **b)** 6CBA_Cal versus 6CBA_41. Results are shown for EEG (blue) and EMEG (orange) and all three stimulation types EW, BT and PT on the x-axes. In each boxplot, the central mark is the median, the edges of the box are the 25th and 75th percentiles. Notice that the data from the volunteers are overlapping in case that less than 5 circles are depicted.

6CBA_Cal) to the source reconstructions of the P20/N20 responses for all three modalities was tested. In Figure 3.7b, these differences are presented between the reconstructions based on the most detailed head model 6CBA_Cal in comparison to the more homogenized 3CICal for EEG, MEG and EMEG. The left plot shows mean source localization differences of 8.5 ± 5.6 mm for EEG, 2.9 ± 2.8 mm for MEG and 3.4 ± 2.4 mm for EMEG. With regard to source localization, the more detailed head modeling thus mainly influences the EEG modality. However, concerning source orientation (middle plot), larger mean differences between both head models are found for all modalities $15.8^\circ \pm 8.5^\circ$ for EEG, $14.6^\circ \pm 12.3^\circ$ for MEG and $11.4^\circ \pm 5.6^\circ$ for EMEG. In the right plot of Figure 3.7b, source strength differences were found between both head models with an average of 11.5 ± 19.5 % for EEG, 7.2 ± 11.8 % for MEG and 6.2 ± 12.8 % for EMEG. Finally, similar to Figure 3.7a, also Figure 3.7b depicts a strong inter-subject variability of the source reconstruction differences which were found for source location, orientation and strength.

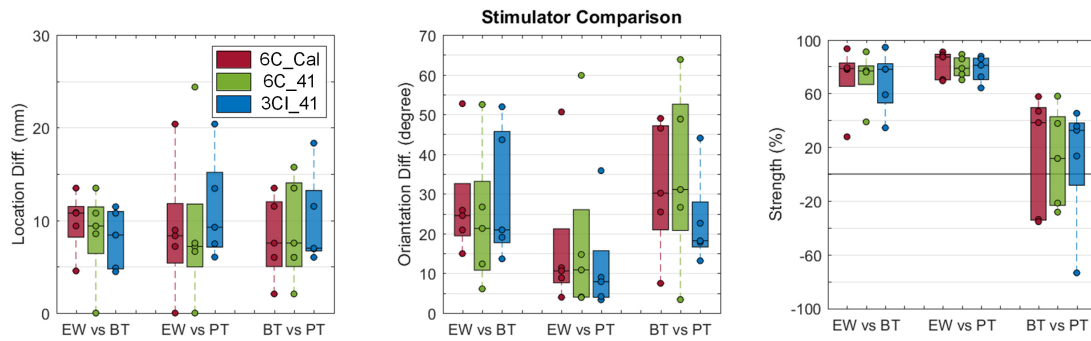


Figure 3.10: Effect of stimulation type on P20/N20 reconstruction: EMEG single dipole deviation scan differences for all subjects and for the standard head models (3CI_41, in blue), the more detailed head models (6CBA_41, in green) and the individually calibrated head models (6CBA_Cal, in red) with regard to source location (left plot, in mm), source orientation (middle plot, in degrees) and source strength (right plot, in %). Reconstructions for the stimulation type EW were compared to BT, as well as EW to PT and BT to PT (x-axes). In each boxplot, the central mark is the median, the edges of the box are the 25th and 75th percentiles.

In the following, the combined SEP/SEF responses are reported for all three stimulation types (EW, BT and PT, see Figure 3.8) comparing the effect of the head modeling and modality on the reconstruction of the P20/N20 response within and between the stimulation types (Figures 3.9 and 3.10). In the EW dataset (Figure 3.8a, left column), the components P14 (in EEG), P20/N20 (MEG/EEG) and N30/P30 (MEG/EEG) can be easily recognized due to their high SNR, most prominently the P20/N20, which is of main interest in this investigation. In BT (Figure 3.8b, left column) and PT stimulation (Figure 3.8c, left column), the P20/N20 is also well recognizable, but due to the less accurate triggering and, for BT also the lower number of stimuli, SNR is overall poorer. Clear bipolar topographies are illustrated for both modalities (EEG and MEG) and all three stimulation types (EW, BT, PT) at the peak of the P20/N20 response (Figure 3.8a-c, right columns). Note the different amplitudes for the three stimulation types in both butterfly and topography plots. Note also that different EEG channels were noise-corrupted and were therefore deleted in the three stimulation types.

In the upper row of Figure 3.9, the most detailed model 6CBA_Cal was considered as a reference and compared the single dipole scan result with the one when using the standard isotropic three compartment model without skull calibration, namely 3CI_41. For the lower row, the same most-detailed reference head model 6CBA_Cal was compared to a six compartment anisotropic head model without skull calibration (6CBA_41). Results are shown for all three stimulation types EW, BT and PT. Because it is well-known that source localization in MEG is far less sensitive to skull conductivity than in EEG [1, 54] and also less affected than EEG with regard to a more detailed modeling of the inner compartments (left plots in Figure 3.7(a and b) and [5]), the results shown in Figure 3.9 were determined only for the modalities EEG and EMEG.

The most detailed head model 6CBA_Cal was first used and compared its reconstructions with those of the standard volume conductor model 3CL41 (upper row in Figure 3.9). With mean differences of 8.6 ± 8.3 mm for EW, 11.8 ± 6.2 mm for BT and 10.5 ± 5.3 mm for PT, EEG source localization (left plot, in blue) was found to be strongly influenced by head modeling. For EMEG source localization (left plot, in orange), smaller mean differences of only 3.4 ± 2.4 mm for EW, 3.7 ± 3.4 mm for BT and 5.9 ± 6.8 mm for PT are found. As shown in the middle plot, the effect of head modeling on the reconstruction of source orientation is similar for EEG (EMEG) with on average $14.6^\circ \pm 9.5^\circ$ ($15.4^\circ \pm 6.3^\circ$) for EW, $16.3^\circ \pm 11.1^\circ$ ($25.7^\circ \pm 15.2^\circ$) for BT and $12.9^\circ \pm 8.9^\circ$ ($14^\circ \pm 11.5^\circ$) for PT. Finally, the right plot depicts source strength differences for EEG (EMEG) of on average 17.8 ± 23.1 % (9.2 ± 20.1 %) for EW, 13.3 ± 60.4 % (0.5 ± 24.4 %) for BT and 3.9 ± 51.6 % (-14.2 ± 38.5 %) for PT.

Furthermore, the most-detailed and calibrated model 6CBA_Cal was used as a reference and compared its reconstructions with those of model 6CBA_41 with standard skull conductivity (lower row in Figure 3.9). While with mean localization differences (left plot, in blue) of 6.8 ± 7.9 mm for EW, 6.5 ± 7.3 mm for BT and 9.0 ± 6.3 mm for PT, SEP reconstructions are strongly affected by skull conductivity variations, combined SEP/SEF differences (left plot, in orange) are rather negligible with 1.6 ± 2.3 mm for EW, no difference for BT and 0.9 ± 2 mm for PT. With EEG (EMEG) source orientation differences (middle plot) of on average $8.2^\circ \pm 9.3^\circ$ ($8.8^\circ \pm 6.7^\circ$) for EW, $13.2^\circ \pm 20.5^\circ$ ($7.9^\circ \pm 8.9^\circ$) for BT and $14.8^\circ \pm 15.9^\circ$ ($9.7^\circ \pm 8.9^\circ$) for PT stimulation and EEG (EMEG) source strengths differences (right plot) of on average -30.2 ± 31.5 % (7.2 ± 16.1 %) for EW, -18.6 ± 39.7 % (-16.2 ± 19.7 %) for BT and -12.1 ± 41.8 % (-27.9 ± 41.4 %) for PT stimulation, skull conductivity variations affect source orientations and strengths in both EEG and EMEG. All results in Figure 3.9 show again a large inter-subject variability.

In the last Figure 3.10, the effect of stimulation type on the EMEG deviation scan of the P20/N20 component was investigated for all subjects and for the standard head models (3CL41, in blue), the more detailed head models (6CBA_41, in green) and the individually calibrated head models (6CBA_Cal, in red) with regard to source location (left plot), source orientation (middle plot) and source strength (right plot). Reconstructions for the stimulation type EW were compared to BT, as well as EW to PT and BT to PT (x-axes). Source localization differences (left plot) between EW and BT were on average 8.7 ± 3.3 mm, between EW and PT 9.8 ± 7.4 mm and between BT and PT 9.0 ± 5.0 mm when averaging also over the different head models (because the variation among the different head models was rather small with 3 mm). Large average orientation differences (middle plot) can be noted for EW versus BT ($27.1^\circ \pm 16.4^\circ$) and for BT versus PT ($29.90^\circ \pm 17.3^\circ$), while the orientation differences are on average smaller for EW versus PT ($15.9^\circ \pm 18.6^\circ$). The source orientations in the BT stimulation type thus deviate most from the two other types, regardless of the head model used. This orientation difference can also already be noted in the topography plots in Figure 3.8. The stimulation type

Table 3.2: The λ values for the different stimulation types: The first column shows the subject number while the next three columns present the λ for all the stimulation types.

Subject	EW	BT	PT
1	210	90	80
2	530	420	590
3	280	270	300
4	870	900	890
5	170	170	740

differences between the head models are larger for source orientation (middle plot) than for source localization (left plot). Finally, as shown in the right plot, an average of 75 % higher source strengths for the EW stimulation was observed when compared to BT and PT, and this result is again independent of the head model used. If BT or PT leads to higher source strengths is unclear and differs across individuals (BT versus PT in the right plot). All results in Figure 3.10 show again a large inter-subject variability.

3.2.4 Effect of Stimulation Type on Individually Optimized TES

In the following, the effect of stimulation type on the individually targeting and optimized TES montage was investigated when taking into account the EMEG P20/N20 dipole sources and the 6CBA_Cal head model.

The λ values for all subjects are reported in Table 3.2. It is observed that a large inter-subject variability exists across the stimulation types.

The distribution of the optimized injected currents in the TES montage is also presented exemplarily for one of the subjects showing anodes and cathodes with respect to the properties (location and orientation) of the target vector. For the specific subject, when the target vector changed due to the stimulation type, a difference in the location of the anodal and the cathodal channels was observed (Figure 3.11). About the EW target vector, the anodes were the channels CP1, C3 and C1 and the cathodes were the Fz, F3, AF3, AF4 and Fpz (left column). For the BT target vector (middle column), the number of the anodes was smaller (CP1 and C1) than the EW target but the number of the cathodes was larger (Fz, F4, AF3, AF4, Fp2 and Fpz). When the PT P20/N20 dipole was used as target vector for the optimization of the TES montage (right column), the number of stimulation electrodes was the same as the BT stimulation type but different electrodes were considered as anodes (CP1 and P3) and cathodes (FC1, Fz, F3, AF3, AF4, and Fpz).

Figure 3.12 shows the corresponding two-patch montage for each one of the three targets and one of the subjects. This figure shows that the location of the patches is independent of the target.

To indicate the individual distribution of the modeled injected currents by the multi-channel TES montage and the two-patch TES, a projection of the current density is ex-

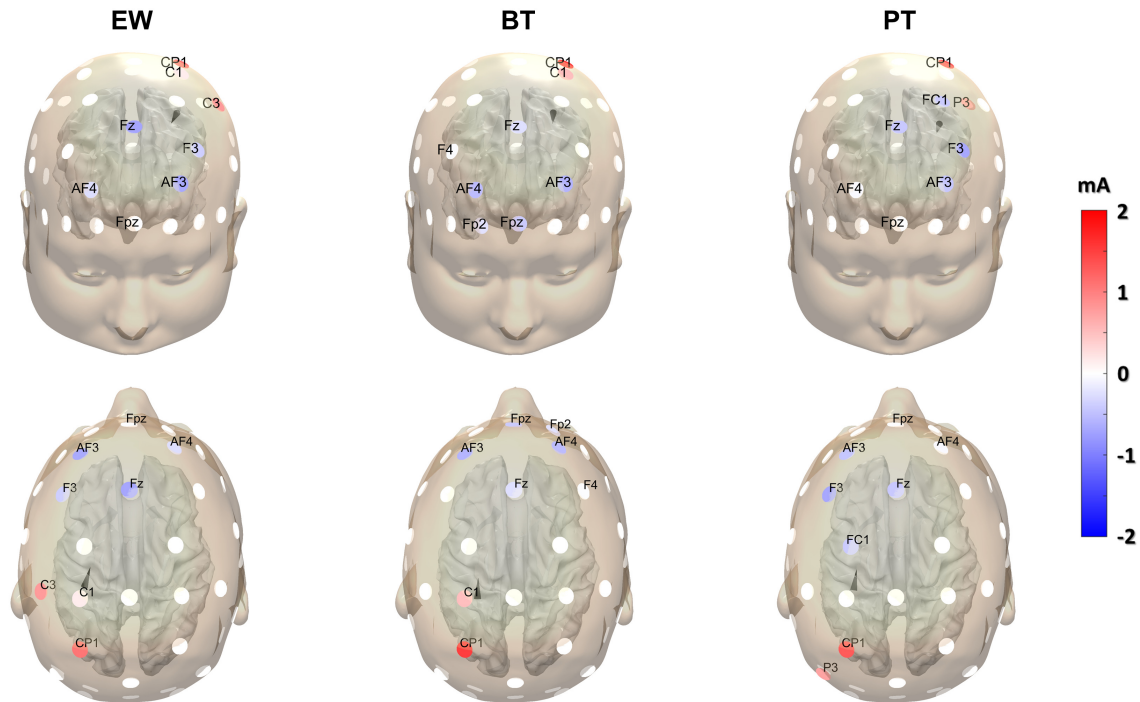


Figure 3.11: Optimized TES montages for the different stimulation types: TES montages are presented after the application of CMI optimization algorithm using the EW, BT and PT P20/N20 targets for a subject of the present study. The defined targets are indicated as black cones while the 39 electrodes of the Startstim System are represented by disk markers and colored by the optimized stimulation currents. The injected currents range from -2 to 2 mA while the total sum of the injected currents is equal to 2 mA to fulfill the safety constraint.

emplarily presented (Figure 3.13 and 3.14) (1) on the inflated cortex and (2) in the target area through a zoomed coronal view as presented in Figure 3.11 and 3.12 for one of the subjects used in this study.

For the current density distribution over the inflated cortex when using the multi-channel TES, the highest currents were observed over the postcentral gyrus for all stimulation types. However, when the BT dipole was used as a target vector, the currents were more broadly distributed compared to both EW and PT cases. About the current density distribution in the target region, the orientation of the currents followed mainly the dipole orientation (Figure 3.13, black cone) and the highest amplitude was observed for the EW dipole. When using the two-patch TES, the current density distribution is mainly located under the two stimulation patches (Figure 3.14). In the zoomed coronal view, it is observed that the injected currents do not follow the orientation of the targets BT and PT compared to the optimized TES montages.

The aforementioned deviation is better quantified by using the TES quality indices DIR and INT as introduced in Section 3.1.11.1. In Figure 3.15, it thus is observable that DIR (in A/m^2) is always two-times higher for the optimized multi-channel TES (CMI / Two-patch: $0.11 \pm 0.6 / 0.05 \pm 0.04$ for EW, CMI / Two-patch: $0.12 \pm 0.04 / 0.055$

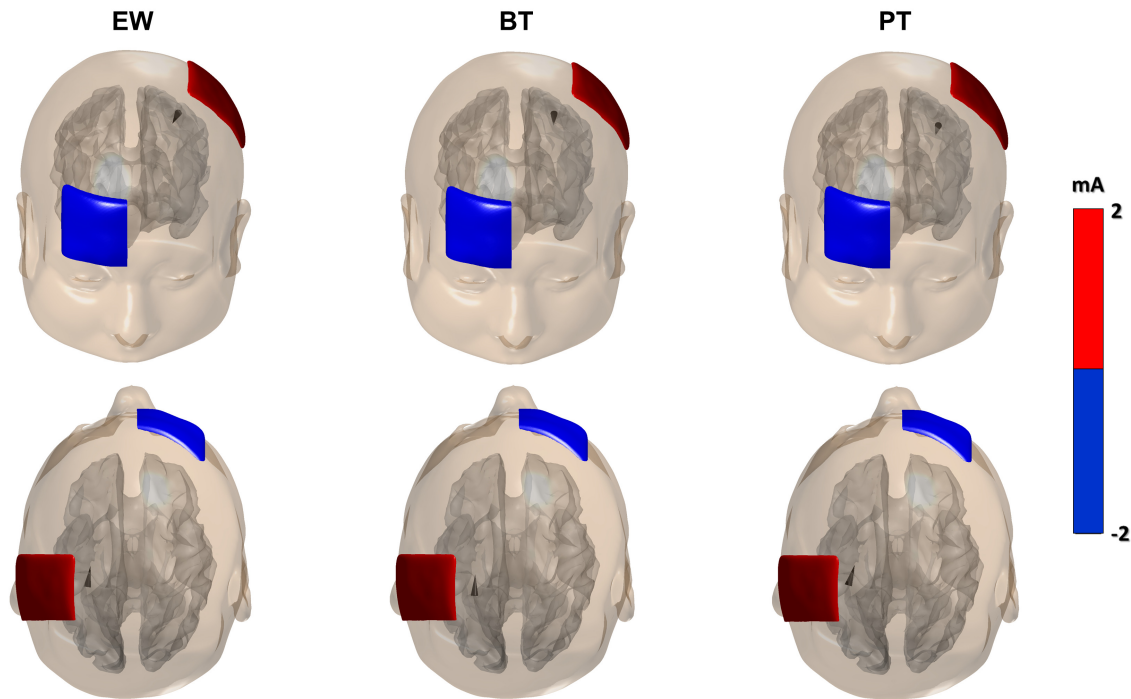


Figure 3.12: Two-patch TES montages for the different stimulation types: Two-patch TES montages are presented using the EW, BT and PT P20/N20 targets for a subject of the present study. The defined targets are indicated as black cones while the two patches are colored by the standard stimulation currents. The injected currents range from -2 to 2 mA while the total sum of the injected currents is equal to 2 mA to fulfill the safety constraint.

± 0.02 for BT, CMI / Two-patch: 0.11 ± 0.05 / 0.05 ± 0.03 for PT). The two-patch TES approach showed higher INT (in A/m^2) for all targets (CMI / Two-patch: 0.039 ± 0.0093 / 0.044 ± 0.013 for EW, CMI / Two-patch: 0.041 ± 0.014 / 0.044 ± 0.013 for BT, CMI / Two-patch: 0.039 ± 0.0096 / Two-patch 0.044 ± 0.013 for PT). With regard to the comparison between the three stimulators, the PT showed the highest averaged DIR value compared to BT and EW for the optimized TES montages while EW showed almost double DIR compared to the BT and PT when two-patch TES was used.

The averaged optimized TES current montages across all subjects were presented in Figure 3.16 for each stimulation type dipole source. All three montages consisted of electrodes that are located mainly in the left side of the TES cap. A threshold of ± 0.1 mA was used to reduce the number of the depicted electrode-labels. The estimated anodes were the electrodes CP5, C3, P3 and CP1 for all the stimulation types while a different number of cathodes occurred among the stimulation types. When the EW was used as a target vector, the cathodal electrodes were mainly AF3, F3, Fz, FC1 and FC2 and the same cathodes plus one more (AF4) for the PT target vector. When BT dipole was used as a target vector, the averaged cathodes were mainly the frontocentral electrodes, Fpz, AF4, Fz, AF3, F3 and FC3. The maximum anodal current occurred in the CP5 electrode for

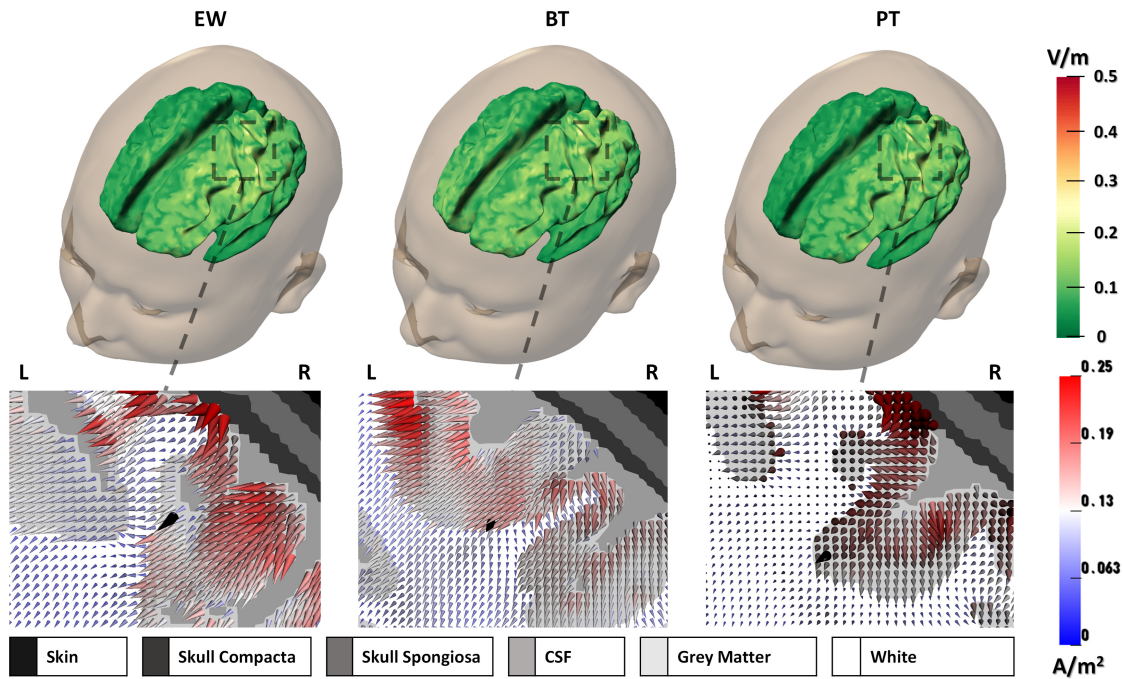


Figure 3.13: The distribution of the current density fields using the multi-channel TES on the inflated cortex and in the target area: The current density distribution is presented for EW (left column), BT (middle column), and PT (right column) on the inflated cortex (upper row) and on the zoom axial view (bottom row) of the reference head model (6CBAH_Cal) for one subject used in the present study. The target is represented by a black cone. The color distribution represents the current density fields measured in V/m. For the current distribution, the colorbar limit is same for all depicted distributions. The color distribution and the scaling factor of the represented current densities in the target area are fixed to the case that preserves the maximum optimized current density across EW, BT and PT. Left (L) and Right (R) indicate orientation.

stimulation types while maximum cathodal current differed among the stimulation types and the corresponding current was 0.87 mA for EW, 0.64 mA for BT and 0.83 mA for PT target. The highest cathodal current was observed in the FC1 for the EW and PT target vectors with a value of -0.7 and -0.49 mA, respectively. The maximum cathodal current for BT appeared in the channel AF3 with an average value at -0.41 mA across all subjects.

Figure 3.17 shows the proportion of the electric field within a sphere of increasing radius and center the location of every target vector (EW: left upper row, BT: right upper row and PT: left lower row). The index half-max radius was presented for showing the interplay between intensity and focality of the induced current in the target region. With respect to the value of radius for which the proportion of the electric field, F , was always equal to 0.5, when the P20/N20 dipole of the EW stimulation type was used target vector, the radius variability was much smaller (74 up to 80 mm, Figure 3.17: left upper row) than the BT (71 up to 85 mm, Figure 3.17: right upper row) and the PT (68 up to 82

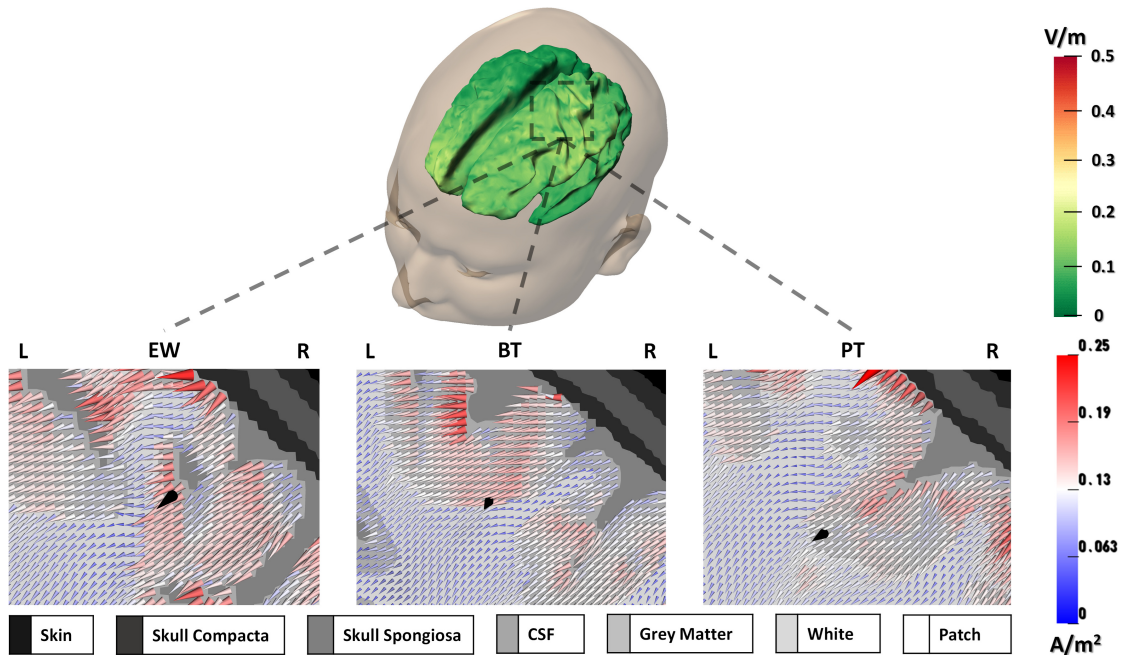


Figure 3.14: The distribution of the current density fields using two-patch TES on the inflated cortex and in the target area: The current density distribution is common for targets while a zoomed coronal view (bottom row) of the current density and each one of the targets is presented on the reference head model with two patches (6CBAH_Cal) for one subject used in the present study. The target is represented by a black cone. The color distribution represents the current density fields measured in V/m. For the current distribution, the colorbar limit is same for all depicted distributions. The color distribution and the scaling factor of the represented current densities in the target area are fixed to the case that preserves the maximum optimized current density across EW, BT and PT. Left (L) and Right (R) indicate orientation.

mm, Figure 3.17: left lower row). As it was presented in Figure 3.17 (right lower row), the amount of the electric field in the target region appeared to be the highest for BT ($0.51 \pm 0.21 \text{ Vm}^{-1}$) and lesser for EW ($0.42 \pm 0.16 \text{ Vm}^{-1}$) than PT ($0.43 \pm 0.16 \text{ Vm}^{-1}$).

3.3 Discussion

In this chapter, a sensitivity group study with five healthy subjects was presented focusing on the P20/N20 source analysis for three stimulation types (EW, BT, PT). The differences in source reconstructions due to these experimental conditions were compared to the differences due to measurement modality (EMEG or single modality EEG or MEG) and to the choice of the head model for the solution of the forward problem. Furthermore, the effects of forward modeling accuracy on the inverse reconstructions was investigated using head models with either the standard 3CI or 6CBA. Thereby, the present head models used either standard skull conductivity (3CI_41 or 6CBA_41) or individually-calibrated skull

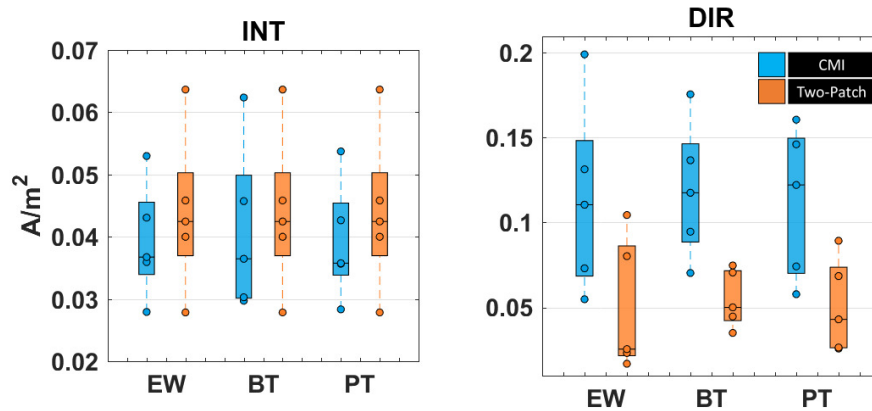


Figure 3.15: TES quality indices: Boxplots show the TES quality indices intensity in the non-target region (left column: INT in A/m^2) and directionally in the target region (right column: DIR in A/m^2) for each P20/N20 target (EW, BT and PT) and stimulation approach (optimization with CMI and Two-patch TES). In each boxplot, the central mark is the median, the edges of the box are the 25th and 75th percentiles.

conductivities (3CI_Cal or 6CBA_Cal).

The individual-skull-conductivity-calibration results revealed a high inter-subject variability with values ranging from 0.0031 S/m and 0.0111 S/m up to 0.014 S/m and 0.0504 S/m for skull compacta and spongiosa, respectively. Skull conductivities thus seem to be largely individual, motivating the need for the proposed calibration procedure using simultaneously measured SEP and SEF data.

The comparison between pairs of stimulation types showed considerable differences (EW-BT: 8.7 ± 3.3 mm / $27.1^\circ \pm 16.4^\circ$, BT-PT: 9 ± 5 mm / $29.9^\circ \pm 17.3^\circ$ and EW-PT: 9.8 ± 7.4 mm / $15.9^\circ \pm 16.5^\circ$ and 75 % strength reduction of BT or PT when compared to EW), regardless of the head model used. EMEG had nearly no localization differences to single modality MEG (0.41 ± 0.9 mm), but large ones to EEG (16.1 ± 4.9 mm), while source orientation differences were non-negligible to both EEG ($14^\circ \pm 3.7^\circ$) and MEG ($12.5^\circ \pm 10.9^\circ$). When comparing reconstructions in the most detailed and individualized reference head model to the standard three compartment head model, localization differences were much smaller for EMEG (EW: 3.4 ± 2.4 mm, BT: 3.7 ± 3.4 mm, PT: 5.9 ± 6.8 mm) than for single modality EEG (EW: 8.6 ± 8.3 mm, BT: 11.8 ± 6.2 mm, PT: 10.5 ± 5.3 mm), while source orientation differences for EMEG (EW: $15.4^\circ \pm 6.3^\circ$, BT: $25.7^\circ \pm 15.2^\circ$ and PT: $14^\circ \pm 11.5^\circ$) and EEG (EW: $14.6^\circ \pm 9.5^\circ$, BT: $16.3^\circ \pm 11.1^\circ$ and PT: $12.9^\circ \pm 8.9^\circ$) were in the same range. The standard realistically-shaped 3CI head model thus seems to perform reasonably well with regard to source localization when including the MEG modality in EMEG scenarios, but with regard to the source orientation and strength components, it might be too simplistic even for EMEG.

When using the CMI algorithm, the optimized channel montages and the corresponding TES metrics were clearly different with regard to the different stimulation types.

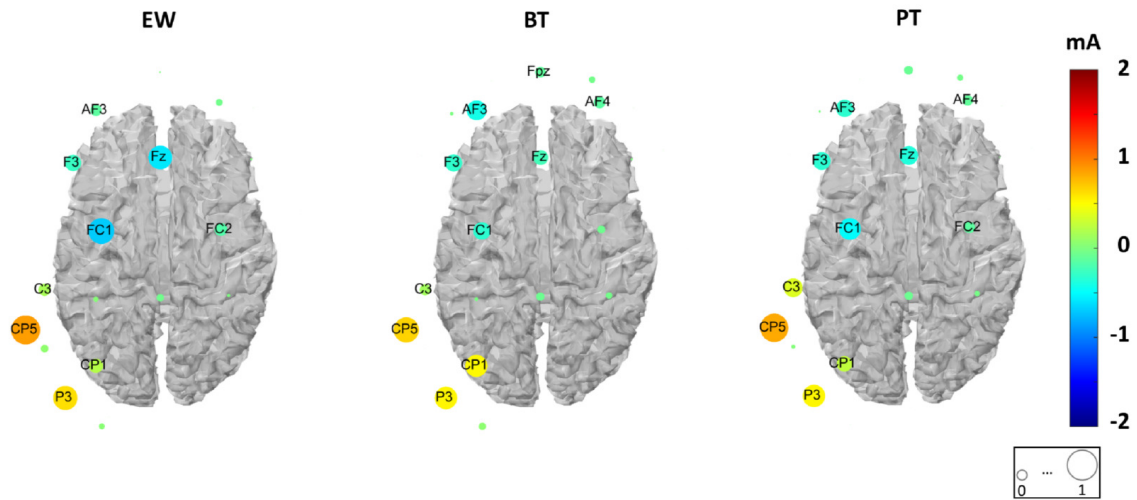


Figure 3.16: The averaged optimized currents on the TES electrodes per stimulation type: An average of the optimized TES currents across all the subjects is depicted per stimulation type (EW: left column, BT: middle column and PT: right column). Color-coded and circled markers represent the distribution of the averaged optimized currents. The markers are also weighted based on the averaged optimized current across all subject which is normalized to vary from 0 to 1 (see labeling within the square at the right-down corner). The color-limit is common for all the presented results.

It can overall be summarized that (1) stimulation type, modality and head modeling have a similar and not negligible influence on the source reconstruction of the P20/N20 component and (2) an accurate target determination with regard to both location and orientation is an important prerequisite for an individually optimized multi-channel TES protocol. Although the MEG can firmly stabilize the P20/N20 localization, the EEG contributes to the determination of source orientation and strength and the complementary information of both modalities in EMEG can be exploited, for example, in TES optimization on the basis of detailed and individualized head volume conductor models.

3.3.1 Effects of Head Modeling and Modality on the P20/N20 Reconstruction

The individual-skull-conductivity-calibration procedure for 3CI and 6CBA revealed lower skull conductivity for the former head model (compare 3CI_Cal to 6CBA_Cal in Table 3.1). This is due to the absence of the highly conductive CSF compartment and the homogenization of the conductivity in the source space area in the realistically-shaped 3CI head model (see Figure 3.6). Similar conductivity sensitivity effects have been found previously using either FEM or FDM [5, 13, 14, 53, 77, 112, 124]. The present results, therefore, support the importance of more realistic modeling of these inner brain tissue compartments that also strongly influence than the estimated individual conductivity parameters for the

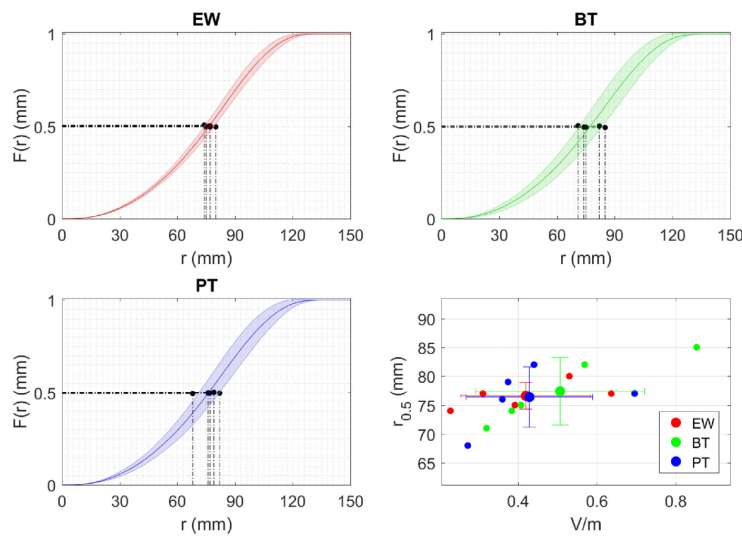


Figure 3.17: CMI performance based on the half-max radius: Proportion of the electric field ($F(r)$ in mm) included within a sphere of increasing radius (r in mm) around every used target (EW, BT and PT) and the variability of half-max radius ($r_{0.5}$ in mm) as a function of the intensity in the target area (in V/m). For the upper images and the bottom-left, an average of the electric field magnitude for increasing radius across all five subjects is depicted as a solid line (EW in red, BT in green and PT in blue) and the $r_{0.5}$ is indicated as a black point. The horizontal axis shows the range of r and the vertical axis represents the proportion of the electric field inside a sphere with center each target. The transparent thick curve (shaded errorbar) indicates the standard deviation across all subjects. In the bottom-right image, errorbars in both axes are shown together with the individual half-radius values. For each errorbar, the central mark represents the mean value and the edges are the 25th and 75th percentiles.

skull layer, as also shown by [44, 82]. In the current study, this skull conductivity variability was demonstrated by a non-invasive estimation procedure using EMEG source analysis and highly detailed FEM head models in healthy participants.

The head model differences in the forward problems then also had a high impact on the inverse source reconstruction of the P20/N20 responses as shown in Figure 3.7b for the EW-type and the comparison 6CBA_Cal versus 3CL_Cal and, even more importantly, when comparing reconstructions in 6CBA_Cal to the non-calibrated head models 3CL_41 and 6CBA_41 in Figure 3.9. For the standard realistically-shaped 3CL head model, even if in Figure 3.9a the MEG has a stabilizing effect on the EMEG average localization results (EW: 3.4 ± 2.4 mm, BT: 3.7 ± 3.4 mm, PT: 5.9 ± 6.8 mm) when compared to the much larger single modality EEG differences (EW: 8.6 ± 8.3 mm, BT: 11.8 ± 6.2 mm, PT: 10.5 ± 5.3 mm), the substantial differences in orientation and strength and the high variability among subjects provides a strong evidence for a considerable influence of the more detailed and individualized head models on the reconstructed activity for both EMEG and EEG. However, largest differences can be seen for the single modality EEG (Figure 3.9a), confirming EEG simulation results as reported by [10, 11, 13]. By focusing now

first on the localization aspect: The presence of the MEG modality, being less affected by volume conduction effects, is especially important to correctly determine the source depth (Figures 3.7, 3.9 a,b and [13]). The source localization difference was 0.41 ± 0.9 mm between EMEG and MEG (Figure 3.7a) and both MEG and EMEG localizations were only slightly affected by head modeling differences (Figures 3.7b and 3.9). The EMEG localizations were thus mainly driven by the MEG. In accordance to the literature [44, 125], conductivity changes close to the source such as CSF or brain tissue anisotropy affected the source localizations only to a small degree. Hence, about the localizational aspect of source reconstruction, the current results are in agreement with the literature and suggest that MEG or EMEG localizations are less affected by volume conduction effects [3, 4, 44].

By focusing now on the quality of source reconstruction with regard to the source orientation and strength components, i.e., the dipole moments: When using the most detailed and individualized head model 6CBA_Cal as the reference, larger source moment differences were found in comparison to 3CI_Cal (Figure 3.7b, middle and right column) and to 3CI_41 (Figure 3.9a, middle and right column) and 6CBA_41 (Figure 3.9b, middle and right column), demonstrating the keen sensitivity of source moment reconstructions to the forward modeling accuracy for all three modalities EEG, MEG and EMEG. A correct reconstruction of the source moment might, however, often be of specific importance. In [98], for example, it was suggested that the source orientation component contains important localizational information by predicting the correct (epileptogenic) side of a sulcal wall. Furthermore, in targeted and optimized multi-channel transcranial electric or magnetic stimulation (TES/TMS), slight changes in target orientation have an even stronger impact on the optimized montages than slight changes in target location (Figures 3.11,3.13 and [12, 56, 82]). Concerning the impact of head model differences to the reconstructed source moments for the EW stimulation type, EMEG was overall more stable, also with regard to inter-subject variability, than EEG and MEG alone, as shown for 6CBA_Cal versus 3CI_Cal in Figure 3.7b (middle and right columns) and for 6CBA_Cal versus 3CI_41 or 6CBA_41 in Figure 3.9 (left panel in middle and right columns). However, differences between EMEG and the single modalities are only moderate due to the fact that the P20/N20 sources are mainly tangentially oriented, so that even reconstructions from MEG alone are not much more affected than from EMEG (Figure 3.7b, middle and right columns), at least as long as they are sufficiently regularized [49]. Though, the MEG outlier of 33-degree orientation difference for one subject (Figure 3.7b, middle column, MEG alone) still points to the fact that source moment reconstructions from MEG alone might be spurious due to the insensitivity of MEG to radial source components. Results for the tactile stimulation types BT and PT are similar to EW as presented in Figure 3.9 (middle and right columns), except for an overall larger inter-subject variability, which might in parts also be due to their lower signal-to-noise (SNR). Noteworthy is also to note that the differences in source moments presented in Figure 3.7 and Figure 3.9 are not only due to changes in head modeling, but they are also resulting from the interplay with the corresponding location differences,

i.e., more substantial location differences (Figures 3.7 and 3.9, left column) most often also result in larger differences in source moments (Figure 3.7 and 3.9, middle and right columns). As shown in Figure 3.7b (right column), the homogenized 3Cl_Cal head model resulted for the majority of subjects in a higher source strength, especially for the EEG and to a smaller extent also for the MEG and EMEG modalities. Especially for the EEG and to a smaller degree for EMEG, this is caused by the lower values for calibrated skull conductivity for the 3Cl_Cal when compared to the 6CBA_Cal head models and by the current channeling due to the additional CSF compartment (Table 3.1 and Figure 3.6; see also [5, 13, 53, 77, 82, 109, 125]). Furthermore, in Figure 3.9 (right column), an increase or decrease of source strength is related to whether the calibrated skull conductivity in Table 3.1 is lower or higher than the standard one, resp., further supporting the crucial role of skull conductivity. For the MEG, where skull conductivity does not have this influence, the source strength differences are mainly caused by the interplay with the corresponding localization and orientation differences and, to a lesser degree, by the effects of the additional CSF and brain anisotropy modeling in the more detailed 6CBA_Cal head model [5, 125]).

In summary, it can be observed in Figure 3.7 and 3.9 that EMEG reconstructions are less susceptible to forward modeling inaccuracies than single modality EEG or MEG. EMEG exploits the ability of MEG to fairly localize the tangential source components even in the presence of forward modeling inaccuracies, while the EEG contributes its sensitivity to radial (and tangential) source orientation components, being, however, vulnerable to head modeling inaccuracies. Because of this complementarity, the combined analysis of EEG and MEG data are of great interest and might lead to less uncertain source reconstructions and a superior spatial resolution, as has already been shown by others [3, 4]. It is demonstrated here in a group-study using three different somatosensory stimulation types and pointed out the importance of using highly detailed and individualized calibrated six-compartment head models for EMEG source analysis.

3.3.2 Effects of Stimulation Type on the P20/N20 Reconstruction

For EMEG and when using the most detailed and individualized reference head model 6CBA_Cal, localization differences between the stimulation types were in average close to 1 cm (Figure 3.10, left column, in red: EW-BT: 8.7 ± 3.3 mm, BT-PT: 9.0 ± 5.0 mm and EW-PT: 9.8 ± 7.4 mm). The present stimulation type localization differences are thus in the same range than those reported for tactile stimulation of either the median nerve or the index finger by [25]. As expected, stimulation type thus has a considerable influence on the P20/N20 localization. The present localizations were validated by measuring Euclidean distances of 7-10 mm to the omega-shaped hand knob area in the motor cortex, showing that the P20/N20 components of all three stimulation types were localized in Brodmann area 3b on the postcentral wall of the central sulcus in SI contralateral to the side of stimulation. This localization result is supported by invasive recordings in humans and monkeys [26] and by later studies using source analysis of SEP and SEF [3, 25, 27, 30].

Because simpler head models had been used in these later studies, the less individualized and/or more homogenized head models 6C_41 and 3CI_41 were used, resulting in similar localization differences for the three stimulation types (Figure 3.10, left column, in green and blue, resp.). The stimulation type localization differences can thus also be worked out with simpler head models, even if their absolute localizations differ (Figures 3.7 and 3.9). Neurophysiologically, the stimulation type localization differences can easily be explained by the different number of activated neuronal fibers and the resulting different synchronization in SI as well as the resulting different source extent. Furthermore, when considering the differences in source strengths in Figure 3.10 (right column), it can be expected that the synchronized pyramidal cells in SI of the tactile conditions PT and BT are just different subsets of those of the EW type. Together with the limitations of the focal single dipole model in the localization of slightly extended activated cortical patches (see discussion in [126], this then leads to the observed localization differences. However, most importantly, and possibly less expected is the present result that the stimulation type localization differences in Figure 3.10 are in the same range than the differences due to modality and head model, as shown in Figures 3.7 and 3.9. It can thus overall be summarized that measurement modality and head modeling play a similarly important role than the less difficult to grasp stimulation type concerning the localization of the P20/N20 component.

Distinct differences were also reported in source orientation between the stimulation types (Figure 3.10, middle column, EW-BT: $27.1^\circ \pm 16.4^\circ$, BT-PT: $29.9^\circ \pm 17.3^\circ$ and EW-PT: $15.9^\circ \pm 16.5^\circ$). While the bulk orientation of the pyramidal cells activated by the BT stimulation type differ most from the other two, the source orientation differences between EW and PT are in a similar range than those due to modality (Figure 3.7a, middle column) or head model (Figures 3.7b and 3.9, middle column). The latter shows again that, like for the localizations, modality and head modeling can have a similar effect on source orientation than the stimulation type, where differences are possibly more apparent. For example, in the studies of [5, 13, 125], significant influences of local (i.e., local around the source such as CSF, white and gray matter as well as brain anisotropy) and remote (especially skull) conductivity changes on source orientation were shown, in agreement to the differences due to head modeling as presented here. While Onishi and colleagues [30] had shown in their SEF source analysis study that depending on the number of activated pins in BT stimulation of the index finger, the resulting localizations within area 3b could easily shift by 5mm, they did not show the corresponding differences in source orientation, most probably due to the limitations of MEG to the radial source orientation components. However, depending on the local and individual area 3b cortical curvature, a 5 mm shift in localization might easily lead to similar bulk orientation changes than presented in the study at hand. Furthermore, and as already discussed in the last paragraph, source orientation might be specifically important as it can also contain localizational information and as it might be influential in montage optimization for multi-channel TES (Figure 3.11). Therefore, it is specifically pointed out here the present result that the EW-PT stimulation type source orientation differences are

in the same range than those due to modality and head model. The current comparison study thus gives a better feeling of the contribution that can be expected in specific source analysis scenarios from combined EEG and MEG using detailed individualized realistic head models.

3.3.3 Effects of Stimulation Type on the P20/N20 TES Targeting and Optimization

Choosing as targets the EMEG dipole source with the most detailed and individualized reference head model 6C_Cal, the result of CMI algorithm was varied across stimulation types and subjects (Figure 3.16). As presented in [102], variations of the individually estimated targets influence the optimization procedure resulting in differently distributed currents over the electrodes compared to the standard montages, e.g., two-patch. For example, the use of fixed electrode montage (e.g. 5×1) was not adopted to the target orientation compared to the individually optimized one reducing the possibility to control stimulation effects on the pyramidal cells located in the target region [108]. Neurologically, the orientation of the stimulation current is important to guide currents towards the brain ROI in order to avoid unexpected cortical excitability effects in non target regions [101]. A similar result was also observed in this study (see Figure 3.15 and 3.14), where two-patch TES was used for simulation of the injection of currents in the regions of interest (EW, BT and PT targets).

As shown in Figure 3.10 and explained in the previous section (3.3.2), the stimulation types EW and PT had a smaller orientation difference than the differences that involve the BT while the location differences are in the same range (Figure 3.10, left column, boxplots in red). When using EW and PT dipole sources for targeting, the corresponding TES montages include the same anodes and cathodes compared to the BT-based TES montage on average across all subjects (Figure 3.16). Already from the selection of the λ (see Table 3.2) parameter was clear that the optimized TES montage would vary per subject and stimulation type. In the preliminary results of [123], such a variation was observed when applying the CMI algorithm to four healthy participants. In the individual level, the TES montages are different for each stimulation type as presented in Figure 3.11. In the same line, the simulated current density of the specific subject differs among the three stimulation types (Figure 3.13, bottom row). The orientation of the current density also follows the target orientation while the magnitude of the current density in the target region is affected by the depth of each target. For the latter, a distance between each EMEG dipole source due to stimulation type to the closest point of the skin compartment showed that the EW is more superficially located than the PT and BT. The corresponding distances were 25 mm for EW, 32 mm for BT and 34 mm for PT. In addition, when quantifying the TES quality among the three stimulation types, the variations in focality of the current density in the target region were considerable across subjects and stimulation types (Figure 3.17).

Finally yet importantly, it is observed that the strongest current densities were observed laterally in border of gray matter with CSF and not fully focused at the target regions 3.13. This could be due to the satisfaction of the potential field $\nabla\phi$ to the maximum principle for harmonic functions which states that a non-constant function always attains its maximum at the boundary of the compartment, in our case, this was CSF [104, 127]. A harmonic function is consider the another possible reason for the latter distribution of the current density could stand the depth of each target that may play a key role in order to reach maximum currents at the target region [127].

In summary, the individual targeting due to different stimulation types leads to large variations on the optimized TES electrode montages. An accurate target determination with regard to both location and orientation is an important prerequisite for an individually optimized multi-channel TES protocol.

3.3.4 Study Limitations

The remaining differences between single modality EEG or MEG and combined EMEG source analysis, are the following: Neither EEG nor MEG data alone allow accurate source analysis of the P20/N20 component. EEG source analysis is sensitive to individual volume conduction parameters, mostly to skull conductivity, but also to a lesser degree to skin conductivity and conductivity of tissues inside the inner skull surface [13, 44]. MEG alone is not sensitive to skull and skin conductivity, but to conductivity of tissues inside the inner skull surface and is especially weak in reconstructing the quasi-radial source component [44]. Skull conductivity calibration, as applied here, should actively alleviate the problem [13]. Therefore, the current results support the notion that the detailed head models and the additional computational costs (per subject, the calibration process and the calculation of all leadfields was performed in an overnight computation job) seem justified by the possible gain in precision. However, a remaining difference between EEG, MEG and EMEG source analysis, as also observed in present results, has to be expected even with the detailed and individualized head models used here. Thus, even though great care has been taken to construct subject-specific individualized multi-compartment realistic head models, the current models still contain simplifications, which might result in modeling errors. For example, in a recent meta-analysis of reported human head electrical conductivity values, [7] did not only report variations in skull conductivity, but also in other conductivity parameters, e.g. scalp conductivity. In [82, 90], also other individual parameters such as scalp conductivity were determined using EIT techniques. In the present study, skull and brain conductivity were individualized but other conductivity parameters were kept fixed at their standard constant value. Furthermore, the used Polhemus-procedure for EEG sensor registration, the fiducial-based registration of EEG and MEG onto the MRI, as well as subject movements in EEG/MEG and in MRI might cause artifacts, that are also reflected in persisting differences between EEG, MEG and EMEG reconstructions.

4 Inter-Subject Variability of Skull Conductivity and Thickness with Age Influences

In this chapter, the inter-subject variability of the calibrated skull conductivity was investigated non-invasively using six-compartment (6C) head models with calibrated skull conductivity and anisotropic white matter conductivity in a group-study of twenty adult subjects.

All figures presented in this chapter were obtained with custom MATLAB codes, Paraview and CURRY 8.

4.1 Material and Methods

4.1.1 Participants and Data Acquisition

4.1.1.1 Participants and Ethics Statement

Twenty right-handed adult subjects, ten male and ten female, in the age range of 18 to 53 years (mean and standard deviation 34.1 ± 10.88) participated in this study. All subjects gave their written informed consent forms and all measurements have been approved by the ethics committee of the University of Erlangen, Faculty of Medicine on 20.02.2018 (Ref No 4453 B).

4.1.1.2 Experiment and EEG/MEG/MRI Acquisition

Somatosensory evoked responses (SEP, SEF) were simultaneously acquired for each subject. The EEG/MEG recording system is the same as described in Section 3.1.2. SEP/SEF data were produced using only EW stimulation type as described in 3.1.3 for the purposes of this study. Furthermore, for each participant, the MRI dataset included T1w, T2w and DTI data using the same MRI system and scanning protocols as described in Section 3.1.4.

4.1.2 Preprocessing of EEG/MEG

For each subject, the preprocessing of EEG and MEG was similar to the procedure described in Section 3.1.5. In the present study, the SNR threshold was also defined empirically. The average number of the excluded trials was 100 per subject.

4.1.3 Head Model Preparation

A realistic and individual six compartment head volume conductor model was created for each subject. The head modeling procedure combines T1w and T2w MRIs for an improved distinction of the skin, skull compacta, skull spongiosa, CSF, gray and white matter. The MRI preprocessing and segmentation procedure for the creation of the corresponding 6C labeled volumes is explained in Section 3.1.6. However, after visual inspection in some cases 1 mm dilation is performed in the eroded full skull image if the resulting SS mask is not matching the corresponding cancellous bone represented in the registered T2w MRI. Calibrated realistic head models were then created following the procedure described in Section 3.1.7. Interaction of the calibrated skull conductivity (skull conductivity) with all the cranial compartment thicknesses and the surface distance with the source depth.

Although, gray and white matter anisotropy was embedded in the head models used in Chapter 3, due to the head modeling sensitivity results presented in [44], only white matter anisotropic conductivity was modeled for the purposes of this and the upcoming studies of this thesis. For this purpose, the scaling factor sf (see Section 3.1.7.2) was estimated differently following [5, 47]. Due to the absence of GM tissue compartment, the terms $d_{GM}\sigma_{GM}^{ISO}$ and d_{GM}^2 of equation 3.4 are zero and the scaling factor sf based only on the white matter (WM) and was equal to $\sigma_{WM}^{ISO}(\frac{d_{WM}}{N_{WM}})$ where N_{WM} was the number of conductivity tensors. The conductivity value for gray matter was 0.33 S/m [44]. The corresponding 6C calibrated head model with white matter anisotropy (6CA_Cal) is presented in Figure 4.1 for one subject of this study.

4.1.4 Definition of Measures

In this section, the four important measures are defined and will be investigated with regard to their inter-subject variability, age and gender dependence, as follows:

1. Skull conductivity (as well as the related measures of the calibration process)
2. Skull thickness
3. P20/N20 surface distance
4. Source depth

4.1.4.1 Measures for Skull Conductivity Calibration

Skull conductivity is individually modeled using the refined calibration procedure as described in Section 3.1.7.3. The outcome of this procedure is a calibration curve with refinement around the minimum, the skull conductivity calibration value, as shown in Figure 4.4. Besides (1) the calibrated skull conductivity, further measures were investigated.

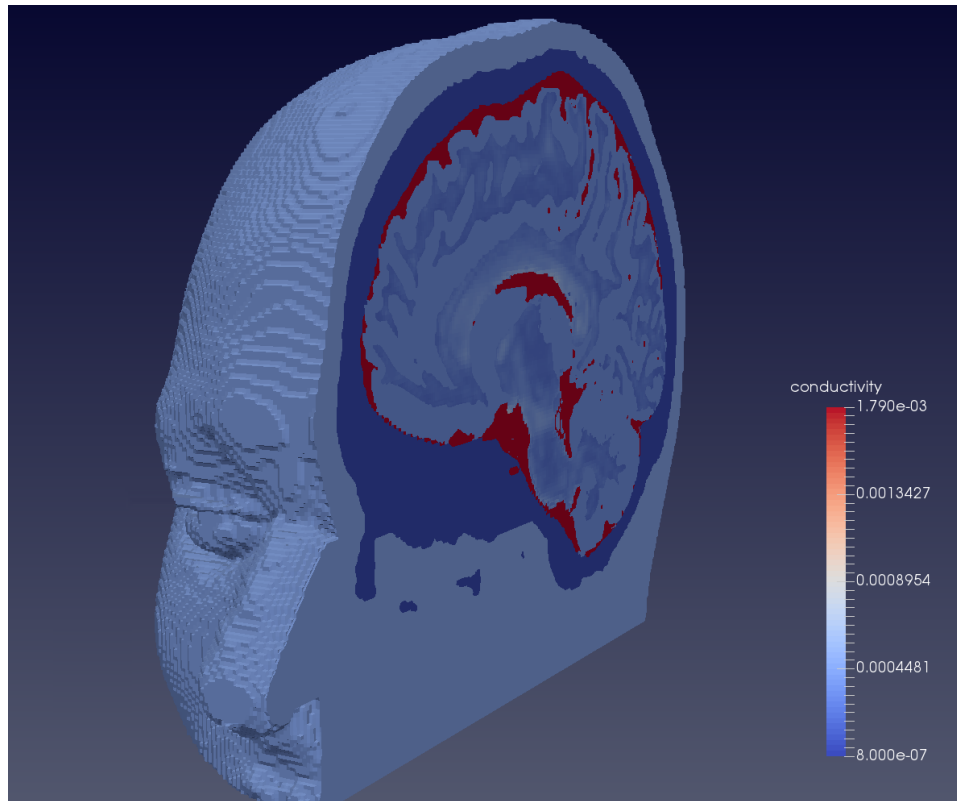


Figure 4.1: Calibrated head model with white matter anisotropy and six compartments (6CA_Cal). The model is color-coded (logarithmic scale) according to the conductivity range for one subject of this study. The spread of the maximum norm of the conductivity tensors, visualized in the white matter compartment.

Those measures are taken into account when accessing the overall quality of the source reconstruction in the calibration procedure [3]. These further measures are listed as follows:

- i The individual P20/N20 latency.
- ii The individual SNR_{SEP} and SNR_{SEF} , quantifying the quality of the SEP and SEF data, respectively, at the specific P20/N20 signal peak. In this study, the SNR is estimated based on [3] and it is considered as the maximum value across all sensors, separately for SEP and SEF data.
- iii The Residual Variance of the SEP data (RV_{SEP}) indicating the remaining distance of the forward simulated to the measured P20/N20 component.
- iv The source strength of the dipole scan result of the calibration procedure.

4.1.4.2 P20/N20 Surface Distance

The scalp surface distance is defined between the potential peak (point P in Figure 4.2b) and the potential trough (point N in Figure 4.2b), based on the following methodological

steps.

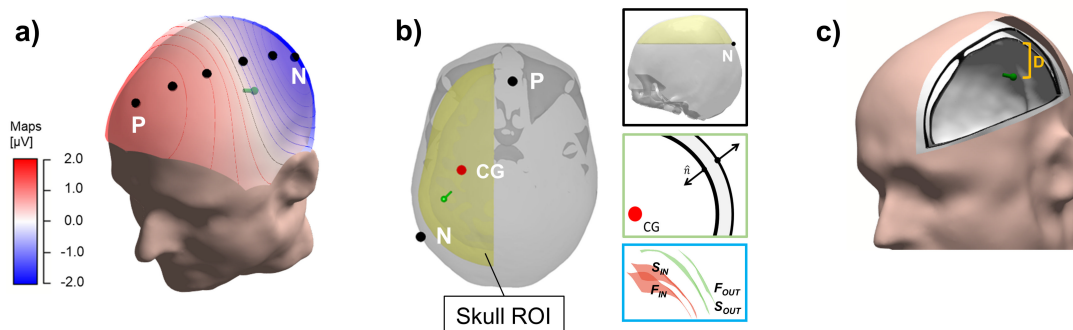


Figure 4.2: Visualization of the measures of Section 4.1.4 for one of the subjects: **a)** Dipole scan result (in green) for the measured P20/N20 component. The black points represent a subset of the surface points for the determination of the distance between the interpolated most positive (P) and most negative (N) potentials of the forward simulated topography. **b)** Skull ROI (in dark yellow) under the P20/N20 topography (P and N points) and dipole scan result (in green). The ROI includes an important area of the left hemisphere (due to right-hand stimulation) under the main SEP topography. It does not contain the potential peak P in order to avoid inclusion of mid-sagittal skull areas where the segmentation quality might be influenced by the pronounced dura compartment. Color boxes show the main steps for the calculation of skull thickness. The black box shows the skull ROI (sagittal view). The green box shows the normal vectors (\hat{n} in black) for the determination of outer and inner skull surfaces. The red point represents the center of gravity (CG) of the ROI. The blue box shows the two outer surfaces F_{OUT} (outer surface of full skull) and S_{OUT} (outer surface of skull spongiosa) (in green) and the two inner surfaces F_{IN} (inner surface of full skull) and S_{IN} (inner surface of skull spongiosa) (in red). **c)** Determination of the source depth: Minimum distance (D) between the reconstructed P20/N20 dipole scan result (in green) and the inner skull surface.

- (1) The subject-specific Cartesian coordinates of P and N is estimated. With the result from the calibration in Section 4.1.4.1, i.e., the best fitting dipole source (Figure 4.2b, green dipole) for the combined analysis of somatosensory P20/N20 component in combination with the calibrated individualized head model, a forward simulated dipolar scalp topography is produced with the following characteristics:
 - a. It maximally resembles the measured SEP/SEF topography at 20 ms post-stimulus.
 - b. It reduces the influence of data noise on the peak-to-peak detection procedure.
 - c. It allows to identify accurately the positive and negative potential peaks P and N, especially since they are most often between electrodes.

Thus, this procedure can be seen as a subject-specific optimal inter- and extrapolation method for the scalp potentials. An example of the dipole scalp topography is presented in Figure 4.2a for one of the subjects.

- (2) P and N are connected through a line with a length corresponding to the Euclidean distance between P and N and discretize this line into equidistant line points, where the distance is chosen according to the discretization size of the scalp surface triangles.
- (3) The MATLAB function `point2trimesh`¹ is used to determine for each line point the corresponding closest point on the triangulated scalp surface mesh (Figure 4.2b, a subset of these points is shown by black dots). Thereby, a distinct curved line results which consists of linear elements over the surface.
- (4) The final surface distance is then approximated between P and N, by summing up the Euclidean length of all linear elements of this curved surface line.

4.1.4.3 Skull Thickness

The region-of-interest, in which skull thickness is determined, includes an important area of the left hemisphere (due to right-hand stimulation) under the main SEP topography. It does not necessarily include the potential peak P and the potential trough N. For example, including P would mean to include mid-sagittal areas, where the pronounced dura compartment might influence skull segmentation accuracy. In Figure 4.2b shows an exemplary skull ROI (in dark yellow) for one subject used in this study. The investigated skull thickness in this ROI is measured for four different compartments:

- Full skull
- Outer skull compacta
- Skull spongiosa
- Inner skull compacta

The segmented masks of the full skull (including both compacta compartments and the spongiosa) and of the skull spongiosa (Section 3.1.6) are utilized for these skull thickness estimations. For each one of these masks, a surface-based geometry (or surface), i.e., a set of triangles and nodes, is constructed through the MATLAB function `isosurface`. Then, the thicknesses are estimated following a recent approach of [92]. In short, the thickness is measured using the compartments outer surface and its inner surface for each one of the four skull compartments. To determine the outer and inner surface of the given skull compartment, the normal vectors (Figure 4.2b, green box, arrows in black) and the center of gravity (CG) of the skull ROI is used (Figure 4.2b, red point). The determination of the normal vectors is established at each node of the skull compartment surfaces. If the scalar product of CG and a surface node normal is positive, the corresponding node is labeled as outer skull surface point, otherwise inner. By applying this procedure independently both

¹https://de.mathworks.com/matlabcentral/fileexchange/52882-point2trimesh-distance-between-point-and-triangulated-surface?s_tid=prof_contriblnk

to the full skull and the skull spongiosa surfaces, the surfaces F_{OUT} and S_{OUT} are extracted (Figure 4.2b, blue box, surfaces in green) and F_{IN} and S_{IN} (Figure 4.2b, blue box, surfaces in red) where “F” and “S” denote full skull and spongiosa, respectively. Then the four different skull compartment thicknesses are measured based on the average values across all the minimum Euclidean distances between each node of the corresponding outer surface (F_{OUT} for full skull; F_{OUT} also for outer skull compacta; S_{OUT} for skull spongiosa; S_{IN} for inner skull compacta) to all nodes of the corresponding inner surface (F_{IN} for full skull; S_{OUT} for outer skull compacta; S_{IN} for skull spongiosa; F_{IN} for inner skull compacta).

4.1.4.4 Source Depth

For each participant, the source depth is defined as the minimum Euclidean distance between the P20/N20 reconstructed dipole source location, resulting from the procedure in Section 4.1.4.1 and the inner surface of the skull. In Figure 4.2d, a sketch for the determined source depth is presented given a reconstructed P20/N20 source (red dipole) and the segmented skull surface in the ROI for one of the participants.

4.1.5 Statistical Analysis

The statistical analysis includes a correlation procedure for testing whether (a) the measures on the head tissues defined in Section 4.1.4 are age-related, (b) skull thickness is related to the calibrated skull conductivity and (c) the P20/N20 surface distance is related to the source depth.

The Robust Correlation Toolbox² is used, allowing automatic detection of outliers and determination of statistical significance through percentile bootstrap confidence intervals (CIs). The skipped Pearson correlation (ρ) is selected as a non-parametric method that takes into account the heteroscedasticity effects compared to the standard Pearson correlation [128]. The rejection of the null hypothesis is based on the bootstrapped CIs at the 95 % percentile level (95 % CI). The corresponding p-value (p) of each 95 % CI is further derived and false discovery rate control (FDR) is applied due to the multiple correlation estimations. The applied FDR method follows [129] and the adjustment level is set to 0.05. The data resampling within the bootstrap procedure is performed 1000 times while the outlier detection is based on the rule of the interquartile range from the same toolbox.

In a subsequent analysis of variance (ANOVA)³, the effect of the gender is considered by adding it as a between-subject factor in a linear regression analysis⁴ with each of the above-mentioned pairs. In a last step, pairwise gender comparisons are conducted, including two-tailed tests separately for each measure of Section 4.1.4 and P20/N20 source analysis parameters. The examined null hypothesis H_0 is that females and males have the same

²<https://sourceforge.net/projects/robustcorrtool/>

³<https://de.mathworks.com/help/stats/regression-and-anova.html>

⁴https://www.mathworks.com/help/matlab/data_analysis/linear-regression.html

mean value. For each test, a data normality test is applied based on a Kolmogorov-Smirnov test [130]. A parametric (paired sample t-test), or non-parametric (Mann-Whitney u-test, [131]) pairwise test is then applied depending on the result of the normality test. A threshold is defined at 95 % level of confidence for both ANOVA and pairwise tests for the significance level of the p-value. FDR adjustment is also applied to the p-values for the multiple comparison correction.

4.2 Results

The result section is divided into two parts: The first part presents the results for the four defined measures of Section 4.1.4 in male and female participants: (i) calibrated skull conductivity (ii) skull thickness (iii) P20/N20 surface distance and (iv) source depth. To improve readability, unless otherwise stated, the term skull thickness will be the full skull thickness (including outer compacta, spongiosa and inner compacta). In the second part, results from the correlation analysis are outlined as defined in Section 4.1.5.

4.2.1 Inter-Subject Variability in the Defined Measures

4.2.1.1 Variability in the Measures for Skull Conductivity Calibration

In Figure 4.3, the P20/N20 reconstructed dipole source (in red) is presented on the individual MRI for one of the subjects. This source reconstruction is the final result of the EMEG source analysis within the skull conductivity calibration procedure (Section 4.1.4.1). The calibrated conductivity is 12.5 mS/m for skull compacta and, due to the fixed ratio of 1:3.6, 45 mS/m for the spongiosa. The dipole source is located on the postcentral wall of the central sulcus in Brodmann area 3b in SI and has a mainly tangential orientation with regard to the inner skull surface.

For each participant, the skull conductivity calibration procedure (Section 4.1.4.1) was applied in the corresponding subject-specific realistic six-compartment head model with WM anisotropy (6CA), resulting in a 6CA calibrated (6CA_Cal) head model. The Residual Variance (RV) of the simulated to the measured data, collected for each conductivity within the calibration procedure, resulted in subject-specific calibration curves that are depicted in Figure 4.4. Finally, determining the minimum in the RV curve allowed us to set up the individual 6CA_Cal head model for each subject.

As Figure 4.4 and Table 4.1 show, the resulting residual variance for the SEP/SEF skull conductivity calibration (minimum of each curve) has a mean of 10.5 % with a standard deviation of 4.51 %, is below 20 % for all of the subjects and the best fit goes even down to only 4 %. Furthermore, large inter-subject variability of the skull conductivity can be observed across all subjects with the lowest skull compacta (spongiosa) conductivity being at 2.6 mS/m (9.36 mS/m) and the highest at 16.9 mS/m (60.84 mS/m), respectively.

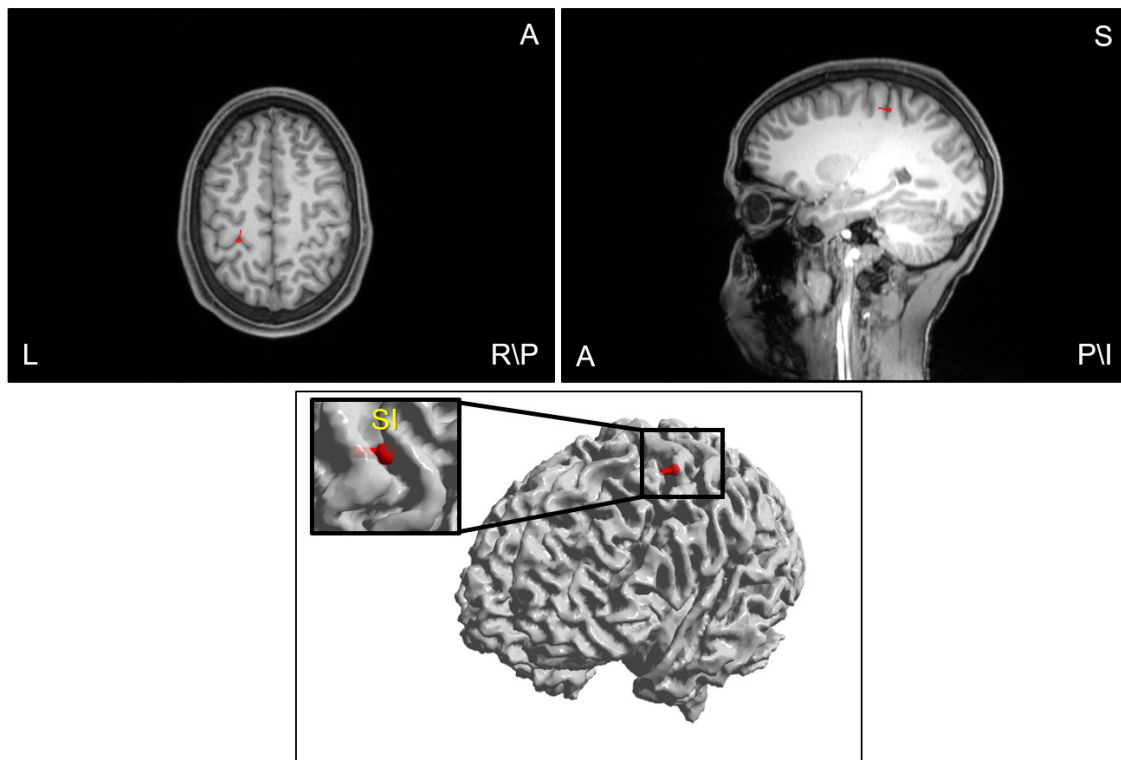


Figure 4.3: Source reconstruction of the P20/N20 component using combined SEP and SEF: The reconstructed dipole source (in red) is the final result of the skull conductivity calibration procedure of Section 4.1.4.1 applied in one of the subjects of the study. The reconstruction result is presented on axial (left) and sagittal (middle) slices of the subject's T1w MRI and on a 1 mm resolution volume-rendering of the cortical surface (right). The dipole is localized in Brodmann area 3b in SI on the postcentral wall of the central sulcus in the primary somatosensory cortex (SI). Further abbreviations correspond to Superior (S), Inferior (I), Anterior (A), Posterior (P), Left (L) and Right (R).

In Figure 4.4, the age-related color coding of the curves expresses at first glance a rather complex relationship between cranial conductivity and age, especially due to two older subjects of age 40 and 43 for whom the calibrated skull conductivities are at 16.1 and 16.9 mS/m, respectively, i.e., as high as for most of the young participants. However, a more detailed inspection shows that the calibration skull conductivity values of the younger participants are overall at higher skull conductivities than those of the older participants.

In the following, the P20/N20 source analysis parameters monitored during the skull conductivity calibration procedure are presented as additional measures introduced in Section 4.1.4.1. The resulting average value across all subjects is shown in Table 4.1. Between genders (Table 4.1, first row: males, second row: females), the P20/N20 latency is significantly shorter ($P = 0.02$) for females (22.67 ± 0.84 ms) than males (23.92 ± 1.3 ms). Otherwise, no other significant gender difference is observed for the remaining P20/N20 source analysis parameters.

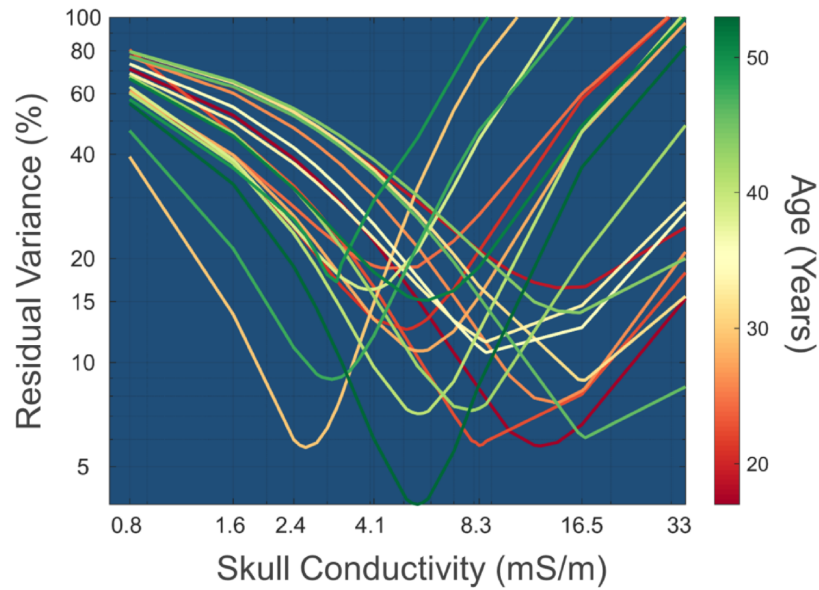


Figure 4.4: Skull conductivity calibration curves for the twenty subjects: Skull compacta conductivity (horizontal axis, in mS/m) and Residual Variance (in %) to the P20/N20 SEP data on the vertical axis, for the dipole scan result as determined by the skull conductivity calibration procedure (Section 4.1.4.1). Each subject is represented by one of the curves, color-coded by age. Y-axis is logarithmically-scaled for better readability.

4.2.1.2 Variability in Measures and Gender Differences

In the present section, the inter-subject variability of the four measures defined in Section 4.1.4 are presented and it is examined if gender differences can be found in those measures. The variability and the median of the measures is provided in Figure 4.5 across all subjects (grey boxplot) and split into subgroups of males (blue) and females (pink).

The most important result is the wide inter-subject variability with large ranges (from

Table 4.1: Gender-based mean and standard deviation across all the participants of the P20/N20 source analysis: Mean and standard deviation are showed with regard to latency (second column), signal-to-noise ratio (SNR) for SEP and SEF (third and fourth columns, resp.), source strength Q (fifth column) and residual variance to the SEP data RV_{SEP} (sixth column) resulting from the calibration procedure as described in Section 4.1.4.1. The symbol asterisk ‘*’ indicates a significant statistical difference ($p < 0.05$) between genders.

Gender	Latency (ms)	SNR_{SEP}	SNR_{SEF}	Q (nAm)	RV_{SEP} (%)
Male	23.92 ± 1.30*	14.94 ± 3.86	22.20 ± 7.52	19.98 ± 10.93	8.57 ± 3.44
Female	22.67 ± 0.84*	14.81 ± 4.72	23.25 ± 7.42	21.02 ± 7.34	12.43 ± 4.76
Total	23.29 ± 1.24	14.88 ± 4.20	22.72 ± 7.29	20.50 ± 9.08	10.50 ± 4.51

* indicates statistically significant difference at the level of alpha 95 %

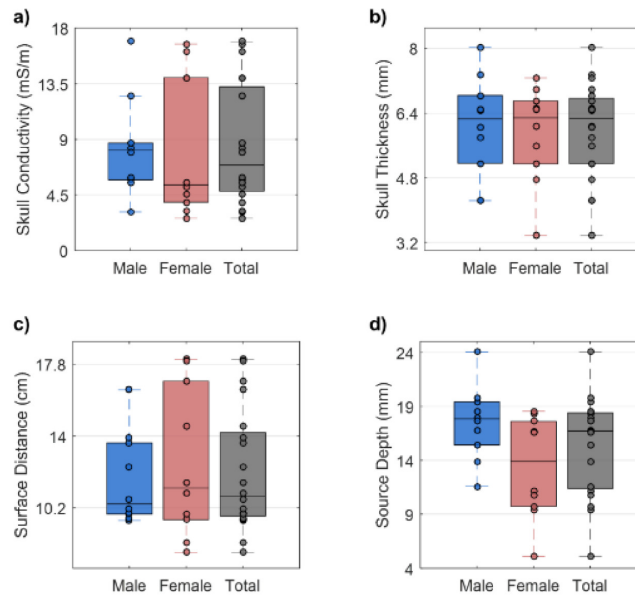


Figure 4.5: Descriptive statistics and inter-subject variabilities: Boxplots depict the inter-subject variability for **a)** skull compacta conductivity (in mS/m), **b)** the averaged full skull thickness in the ROI as indicated in Figure 4.2b (in mm) **c)** the P20/N20 surface distance (distance of P to N; in cm) and **d)** source depth (in mm). Color-coding is used to distinguish male (blue; 10 subjects), female (pink; 10 subjects) and total (grey; 20 subjects) groups. The filled circles represent individual results per subject. Note that there are overlapping values within some of the boxplots. Per boxplot, the central horizontal black line is the median and the edges of the box are the 25th and 75th percentiles.

minimum to maximum) for all four measures for the total group as well as for the male and female subgroups.

The calibrated skull compacta conductivity ranges from 3.1 up to 16.9 mS/m for males and from 2.6 up to 16.7 mS/m for females (Figure 4.5a). The mean and standard deviation across all subjects is 8.44 ± 4.84 mS/m.

The calibrated skull compacta conductivity ranges from 3.1 up to 16.9 mS/m for males and from 2.6 up to 16.7 mS/m for females (Figure 4.5a). The mean and standard deviation across all subjects is 8.44 ± 4.84 mS/m.

Figure 4.5b shows that full skull thickness in the ROI ranges from 4.22 up to 8.02 mm for males and 3.36 up to 7.27 mm for females. Mean and standard deviation across all subjects are at 5.97 ± 1.19 mm. In Table 4.2, group-wise (male, female, total) mean and standard deviation are additionally presented for the three different cranial compartments. For outer- and inner-compacta, the male subgroup is found having a higher mean thickness value than the female one, while it is the other way around for the spongiosa.

The P20/N20 surface distance was found to be in a range of 9.5 to 16.4 cm for males and 7.8 to 18.1 cm for females (Figure 4.5c). Mean and standard deviation across all subjects are 12.08 ± 3.21 cm.

Table 4.2: Gender-wise mean and standard deviation of the thicknesses for outer and inner compacta and spongiosa skull compartments in the ROI as indicated in Figure 4.2b.

Skull Compartment	Gender	Average Thickness in the ROI (mm)
Outer-Compacta	Male	1.12 ± 0.52
	Female	0.93 ± 0.62
	Total	1.02 ± 0.57
Spongiosa	Male	3.41 ± 0.93
	Female	3.96 ± 0.96
	Total	3.69 ± 0.96
Inner-Compacta	Male	1.10 ± 0.80
	Female	1.06 ± 0.46
	Total	1.08 ± 0.64

In Figure 4.5d, the inter-subject variability is presented in source depth, where values range from 11.57 up to 24.05 mm for males and from 5.1 up to 18.56 mm for females. Additionally to the results presented in Figure 4.5d, a mean and standard deviation of 15.45 ± 4.54 mm across all participants is determined for source depth.

Finally, no statistically significant gender difference was observed when applying pairwise statistical analysis on the mean value of each of these measures.

4.2.2 Statistical Results

The robust pairwise correlation was applied independently between the investigated adult age group and each of the four measures. The following relationships are also assessed: i) between the thickness of the skull (for all three cranial compartments) and the calibrated skull conductivity and ii) between the P20/N20 surface distance and the source depth.

In Figure 4.6, the statistically significant correlation pairs are presented, i.e., calibrated skull conductivity with age (left subfigure) and calibrated skull conductivity with skull thickness (right subfigure). The remaining correlation pairs are outlined in Table 4.3 and 4.4.

When including gender as a between-subject factor in these pairs through linear regression modeling, no statistically significant effect ($p > 0.05$) could be observed. Therefore, the corresponding ANOVA results are not presented.

In the first investigation, the examination was if the defined measures in Section 4.1.4 are correlated with age. In Figure 4.6a, a statistically significant negative relationship is presented ($\rho = -0.5$, 95 % CI = [-0.78 -0.18], $p = 0.017$) occurs between age and calibrated skull conductivity. One female (43 years old and calibrated skull conductivity: 16.9 mS/m) and one male (40 years old, calibrated skull conductivity: 16.1 mS/m) were identified as outliers (Figure 4.6a, two circled black crosses on yellow background). The P20/N20 surface distance has a weak positive interaction with age (Table 4.3, fifth row:

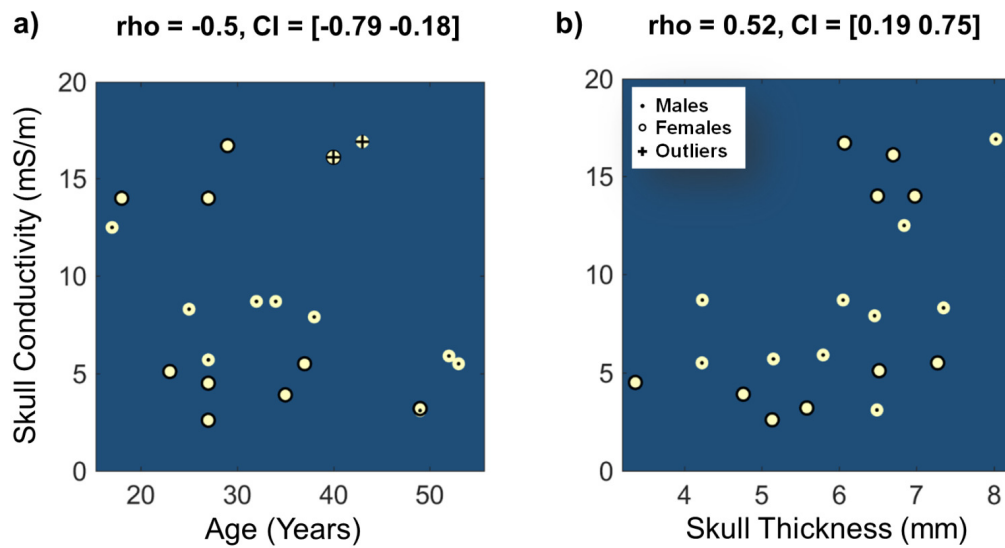


Figure 4.6: Interaction of skull conductivity with age and skull thickness: The figure contains the robust correlations between the (calibrated) skull conductivity (in mS/m) and **a)** age (in years) or **b)** (full) skull thickness (in mm). The skipped Pearson correlation value (ρ) and the confidence interval (CI) are presented on top of both images. 95 % CI were computed using bootstrapping with 1000 permutations. The corresponding FDR adjusted p-value was 0.017 and 0.01 for **a)** and **b)**, respectively. Notice that the data from the participants are overlapping in case that less than twenty points are depicted.

$\rho = 0.29$, 95 % CI = [-0.12 0.64]), while the thicknesses of the full skull, outer compacta, spongiosa and inner skull compacta in the ROI are also weakly, but negatively, correlated with age (Table 4.3, rows 1-4). For the correlation pair of source depth and age, a positive interaction is observed but not statistically significant (Table 4.3, row 6: $\rho = 0.35$, 95 % CI = [-0.14 0.65]). No outliers were detected for these correlations.

Table 4.3: Interaction of age with the measures from Section 4.1.4: Cranial compartment thickness in the ROI, surface distance and source depth with age. The first and second columns indicate the number and the name of the correlation pair, respectively. The third column shows the correlation value (ρ) and the fourth column presents the bootstrapped confidence interval (CI). The fifth column shows the p-value (p) as derived from each bootstrapped CI and adjusted with FDR.

No	Correlation pair	ρ	CI		p
1	(Full Skull Thickness, Age)	-0.10	-0.53	0.27	0.210
2	(Outer- Compacta Thickness, Age)	-0.14	-0.46	0.22	0.216
3	(Spongiosa Thickness, Age)	-0.11	-0.51	0.31	0.216
4	(Inner- Compacta thickness, Age)	-0.34	-0.76	0.08	0.216
5	(Surface Distance, Age)	0.29	-0.12	0.64	0.210
6	(Source Depth, Age)	0.35	-0.14	0.65	0.210

In the second study, it was investigated whether there is a dependence between skull

thickness and conductivity, also with the aim of observing whether the non-invasive approach can achieve a similar result as an invasive approach (e.g. [87]). With regard to the correlations between the thickness of all of the cranial compartments in the ROI and the calibrated skull conductivity, the results varied depending on the combination. In Figure 4.6b, a statistically significant positive correlation was revealed between skull thickness and calibrated skull conductivity ($\rho = 0.52$, 95 % CI = [0.19 0.75], $p = 0.01$). The remaining correlation pairs, shown in Table 4.4, are not statistically significant according to their CIs and p-values. In particular, the thickness of the cranial compartments spongiosa and inner compacta has a low positive interaction with the calibrated skull conductivity (Table 4.4, rows 2-3), while an opposite low interaction occurs with the outer compacta thickness and the calibrated skull conductivity (Table 4.4, row 1, $\rho = -0.25$).

For the last correlation pair, i.e., the surface distance and the source depth, a marginally negative but non-significant value occurred (Table 4.4, row 4, $\rho = -0.34$).

No outliers occurred during the assessment of the correlations showed in Table 4.4.

Taking into account the significant correlations 4.6, a linear mixed-effect analysis⁵ was also used to assess the effect of age and full skull thickness on the calibrated skull conductivity based on gender. The predicted variable was the calibrated skull conductivity which age, full skull thickness and gender were the predictor variables (b). From this analysis, we get that age and (full) skull thickness are two significant predictors ($b_{\text{age}} = -0.01$ and $b_{\text{skull.thickness}} = 0.18$, $p < 0.05$) while gender showed a weak effect ($b_{\text{gender}} = -0.39$, $p = 0.06$). In this analysis, similar outliers were observed as presented in 4.6.

4.3 Discussion

In this study in a group of twenty adult subjects in the age of 18 to 53, it is estimated and evaluated the inter-subject variability of bulk (calibrated) skull conductivity using the non-invasive modalities EEG and MEG in fusion with MRI, modalities that are available in MEG laboratories and for which ethical clearance is nowadays standard. The most important result is the high inter-subject variability over the investigated age range and in each age subgroup, as the high variances in Figures 4.4, 4.5 and 4.6 clearly illustrate. This means that approaches like the proposed calibration procedure are needed to individually estimate skull conductivity, one of the most important forward modeling parameters in EEG and EMEG source analysis [13, 132] as well as in TES [12]. Besides the high inter-subject variability, pointing to the need for individualization of experimental procedures, two significant relationships were found (Figure 4.6). The present results therefore motivate the following experimental setup: In a first run of 10 min, SEP and SEF data are collected, serving for head model calibration. This first run is followed by the main acquisition runs of EMEG data of interest (for example inter-ictal activity in presurgical epilepsy diagnosis). These main data are then being analyzed using the individually calibrated realistic head

⁵<https://www.mathworks.com/help/stats/fitlme.html>

Table 4.4: Interaction of the calibrated skull conductivity (skull conductivity) with all the cranial compartment thicknesses and the surface distance with the source depth. The first column indicates the row number, the second the correlation pair, the third the correlation value (ρ), the fourth the bootstrapped confidence interval (CI) and the fifth the p-value (p) derived from each bootstrapped CI and adjusted with FDR.

No	Correlation pair	ρ	CI	p
1	(Skull Conductivity, Outer-Compacta Thickness)	-0.25	-0.59 0.17	0.210
2	(Skull Conductivity, Spongiosa Thickness)	0.13	-0.41 0.62	0.216
3	(Skull Conductivity, Inner-Compacta Thickness)	0.26	-0.13 0.61	0.210
4	(Surface Distance, Source Depth)	-0.11	-0.53 0.35	0.216

model.

The application of the presented calibration procedure in a group of twenty adult subjects yielded large inter-subject variability among the estimated skull conductivities (Figures 4.4, 4.5a and 4.6). This was also reported in [7]. Other studies using DAC on skull pieces temporarily removed during surgery showed a high inter-subject variability [8, 87]). For 1 kHz DAC, Tang et al. [87] indicated a variation of skull conductivity between 3.77 and 17.29 mS/m, a result which is close to the present range of 2.6 to 16.9 mS/m. Arumugam et al. [90] used EIT in ten subjects and found a skull conductivity variability of 1.8 to 5.6 mS/m using T1w MRI for the segmentation of a five compartment head model. Compared to the above DAC and EIT studies, the present results (Figures 4.4, 4.5a and 4.6) were found to be in a similar variability range. Those results are based on the non-invasive modalities EEG, MEG and MRI that are generally available in a standard MEG laboratory, measured under *in vivo* conditions and in the low frequency range of interest, when considering the frequency-dependence of conductivity measurements [9, 87, 133, 134]. By using same modalities (i.e. EEG/MEG/MRI), Baysal and Hauelsen [135] included individual skull conductivity estimations using SEP/SEF of nine subjects, showing also an inter-subject variability from 1.5 up to 1.74 mS/m. This study was one of the first step towards the use of SEP/SEF data for calibration of skull conductivity. However, their reported variability contained a much smaller range (1.5 mS/m up to 1.74 mS/m) than in the present study. This smaller range might be due to the neglect of modeling the highly conductive CSF compartment or the use white matter anisotropy that play an important role on the forward simulations of both EEG and MEG at the primary somatosensory cortex [5, 53].

In Table 4.1 the further defined measures from Section 4.1.4.1 were presented for the source analysis within the skull conductivity calibration procedure. With SNR values of 14.88 ± 4.20 for SEP and 22.72 ± 7.29 for SEF data, a single run of only 10 min for 1200 trials gave enough data quality for accurate source analysis. The higher SNR value for MEG compared to EEG for the same number of trials shows the higher sensitivity of MEG than EEG to the rather lateral (Figure 4.5, maximally 24 mm deep) and mainly tangentially-oriented (on average only $25.5^\circ \pm 18.6^\circ$ deviation from the tangential plane, being parallel to the inner skull surface) P20/N20 dipole source in Brodmann area 3b.

It has been shown in various studies that such sources are better detectable by MEG than by EEG [4, 136]. This higher detectability together with the insensitivity of MEG to skull and skin conductivity [2] supports the idea of relying on MEG dipole scans for an accurate localization within the SEP/SEF calibration procedure. The low residual variance of 10.50 ± 4.51 % (Figure 4.4 and Table 4.1) shows that the collection of only a single run with 1200 trials together with the model of a focal dipolar P20/N20 source [25, 26] in a calibrated and highly realistic head model seems acceptable for the calibration needs. A simultaneously activated deep thalamic source at the P20/N20 peak as proposed by [3, 27] is hardly detectable in the MEG [3] and therefore also hardly influences the MEG driven localization process. Furthermore, Götz et al. [137] showed that in 10 out of 12 subjects, the single dipole model performed accordingly at the P20/N20 peak and in some first test simulations, an additional thalamic source also did not significantly influence the calibration results. The short acquisition time of 10 min for SEP/SEF data are an important advantage when compared to e.g. MREIT, which takes longer [7]. The computation time for the skull conductivity calibration, including all EEG/MEG forward calculations for six compartment white matter anisotropic head modeling, was an overnight job, for each subject. It can be thus summarized that the proposed calibration procedure is feasible in a standard MEG laboratory with an additional EEG/MEG measurement time of only 10 min per subject.

A particularly strong influence of skull conductivity on EEG forward simulations and EEG source analysis has been reported in many studies using realistic head models of different detail [10, 11, 13, 14, 44, 53, 89, 124]. Previous studies on EEG [11, 13, 53] and EMEG [44] source analysis also showed that skull conductivity inaccuracies can easily lead to localization errors in the centimeter range. Furthermore, skull conductivity was also found to be the most influential parameter for optimized TES, as shown in recent uncertainty analyses [12, 132]. Therefore, the use of subject-specific calibrated realistic head volume conductor modeling, as presented in this work, is suggested to take into account the inter-subject variability of skull conductivity in EEG and EMEG source analysis as well as in optimized TES.

Based on the results of the robust correlation analysis, (calibrated) skull conductivity and age showed a significant negative correlation (Figure 4.6). This inverse relationship is in line with previous studies on this topic [8, 90]. In agreement with the results of this study, Hoekema et al. [8], who worked on a group study with five patients aged 11 to 50 years, found that skull conductivity is higher in younger patients than in older patients, which supports the present finding on the relationship between cranial conductivity and age. Using EIT, Arumugam and colleagues [90] found a negative correlation trend in a group study with ten subjects, aged 23 to 49 years. Other studies with mammals such as for example rats [138] that, however, measured skull conductivity at microwave frequency, have also reported such a negative relationship. In the present study, the skull conductivity was estimated by means of a non-invasive procedure based on SEP/SEF recordings in the low frequency range of interest and in an age range from 18 to 53 years. Since EIT and

SEP/SEF methods have shown agreement on their estimated skull conductivities [83], the resulting correlation of the calibrated skull conductivity with age could have been expected, considering the distribution of the age range used in this study.

The correlation analysis also yielded a statistically significant positive correlation between skull conductivity and (full) skull thickness (Figure 4.6b). This finding is supported by [87] who measured resistivities of 388 skull samples, excised from 48 skull flaps of patients undergoing surgery using DAC. Furthermore, we observed a non-significant negative correlation between skull thickness and age (Table 4.3). As shown in [139] (see Fig. 5), skull thickness increases exponentially in the age range from 0 to 18 years, while in the age range from 18 to 20 years, a high inter-subject variability starts dominating an only small remaining linear increase of skull thickness over time. It can be assumed that this variability continues for older subjects, as shown here (Figure 4.5b) and similarly supported by [78, 91, 92], which makes it difficult to extract a robust correlation of skull thickness with age.

The significant finding on the relationship of skull conductivity and age could depend on the chosen age range. When excluding the older participants around 50 (49 – 53), it does no longer observe a significant negative correlation ($\rho = 0.11$, $CI = [-0.55 \ 0.60]$) between calibrated skull conductivity and age. When excluding the same subgroup of participants, a non-significant correlation of spongiosa thickness over age is still observed ($\rho = 0.17$, $CI = [-0.30 \ 0.63]$) compared to (Table 4.3, row 3). This irregularity in the age subgroups over the larger age range should be further studied in this study, also due to the results of ([78]; Figs. 3 – 5), where it was shown that the spongiosa thickness varies non-monotonically over the large age range from 16 to 90 years. A future study should therefore include a larger number of participants, particularly in the age range from 40 to 53, to further investigate the relationship between skull conductivity, age and thickness, with a possible further focus on age subgroups. Finally, osteoporosis [140] could potentially influence these relationships.

The evaluated correlation pairs of this study were determined for a group of subjects in the adult age range (age of 18 to 53). The results could surely differ strongly for a group of subjects in childhood and also in older age. Particularly in newborns, also due to the presence of fontanelles, as well as in the first years of life, cranial development, including skull thickness and skull conductivity, can be considered highly nonlinear [77, 89, 139].

Regarding the lack of further significant correlations (Table 4.3, 4.4), the limited sample size and the relatively non-uniform age range could be main factors, and remaining modeling simplifications might play a role. Sowell et al. [141] determined that cortical thickness in the postcentral gyrus could decrease in the age from 20 to 87, replaced by CSF [142]. The latter could be a reason for the positive, however, non-significant, correlation of P20/N20 source depth over age (Table 4.3). In addition, modeling simplifications, such as the use of standard non-individualized skin and gray matter conductivity values could have influenced the calibrated skull conductivity values in this work, source strength and

residual variance to the SEP data RV_{SEP} in Table 4.3 ([13]; Fig. 7).

With regard to gender, the only significant difference was found for the P20/N20 latency (Table 4.1). The shorter measured P20/N20 latency in males is in line with previous studies [143, 144] and can easily be attributed to the longer arms of males [144]. Furthermore, even if gender is often considered as an additional factor in the relationship between skull thickness and age (see Review [93]), in the data presented here, inter-subject variability limits the possibility of an observation of such a gender effect. Since skull thickness and conductivity are related (Figure 4.6b and [87]), it was assumed that through a possible influence of gender on skull thickness, an indirect influence of gender on skull conductivity could also exist. However, as ANOVA analysis showed, no gender effect was observed ($p > 0.1$). Considering also gender in a linear mixed-effects analysis, as presented in Section 4.2.2 age and full skull thickness remained significant predictors of the calibrated skull conductivity while gender was weak ($p = 0.06$). Taking into account the variability of cranial thickness in both subgroups (Figure 4.5b, Table 4.2) which is supported by [91, 92], the absence of a gender effect could be expected. These two studies used a large number of CT datasets and also showed no significant gender differences for thickness of the skull regions in the left hemisphere. The results presented in this and their study mainly only emphasize the large inter-subject variability. In summary, due to the large inter-subject variability, the evaluation of gender effects and differences in the measures studied here might remain a challenging task.

Two subjects in the age of 40 and 43 were detected as outliers in the correlation pair presented in (Figure 4.6a) due to their exceptionally high calibrated skull conductivity. We found that their average skull thicknesses of 6.5 mm and 8 mm in the defined skull ROI (Figure 4.3b) was also relatively large, with large variation over the ROI (3.4 – 8 mm). However, while in this group study, these values were on the higher side, according to (Fig. 6 in [87], Fig. 1 in [91]), even higher thicknesses can be found. It is expected that a larger number of participants in the age range of 40 would smoothen the skull thickness range presented in this study.

The selected age group in this study reflects the age range of the subject pool at a MEG center, with fewer data points in the range under 22 and over 40 and many participants of student age. In particular, however, this study is an important part of an epilepsy project to investigate whether EMEG analysis in individualized head-volume conductor models with calibrated skull conductivity can provide a better estimate of the epileptogenic zone. Of particular interest is the comparison to EEG or MEG single-modality analyses and analyses using simplified and non-calibrated head models. In first proof-of-principle studies, a superiority of EMEG analysis using head models calibrated for skull conductivity has already been shown [18, 47]. Most epilepsy patients in presurgical epilepsy diagnosis - a main clinical application of EEG/MEG source analysis - in whom surgery is considered are also in the age group as investigated here [39]. Therefore, in especially this age range, individually calibrated skull conductivity can provide useful information for

epilepsy diagnostics. Thus, it was a specific interest in this study to use a non-invasive method using hardware available in a MEG center to investigate how age and gender can influence skull conductivity and thickness in middle-aged adults. Therefore the number of participants was different in all age subgroups, but special attention was paid to an equal number of men and women for the gender investigations. The main result of this work, namely to show the need for individually calibrated head models for a MEG source analysis due to the large variance in skull conductivity for this important age range, could therefore be achieved.

Correlations between skull conductivity, thickness and age in childhood have not been examined here due to the limitation of the ethics vote of this work to adult studies. Future studies using the non-invasive procedure present in this work could thus investigate not only larger sample sizes, but also include the childhood age range, and thereby stabilize the statistics for an analysis in a complete age-range. It would also be interesting to investigate how other factors, e.g., nutrition or health, might influence the defined measures.

Within the construction of the realistic head models in Section 4.1.3, modifications in the erosion operator would have influenced the determined ratio between cancellous and cranial bone. An erosion of only 1 mm could have resulted in too thin inner and outer compacta and could have thereby led to a “skull leakage” as described by [145, 146]. A higher erosion value (> 2 mm) could have artificially reduced the skull spongiosa and increased the inner and outer compacta thicknesses, which would in turn have increased the calibrated skull conductivity presented here. In the future, investigations will be carried out for the use of level set tissue segmentation approaches in combination with unfitted finite element methods that better include the partial volume effects [147], and its influence on skull conductivity calibration.

In order to avoid overfitting [29, 86], one degree of freedom was allowed in the calibration procedure for the most influential parameter as detected by uncertainty analysis, namely skull conductivity [13, 132]. It cannot be excluded that possible inter-subject variabilities in skin or GM conductivity could have influenced the calibrated skull conductivity values in this work [13, 132]. However, for the influence of the second most important parameter for the EEG, namely skin conductivity ([13], Figures 7, 9), it was also found that variability of skin conductivity has a smaller influence on source depth ([13]; Fig. 9) for lower skull conductivities. Furthermore, since MEG is insensitive to skin conductivity, at least the presented source localizations and source depths should be mainly not influenced by individual variations in skin conductivity. An overlaid thalamic activity might also simultaneously be present in the P20/N20 component in a small percentage of subjects [137]. Still, future studies are needed to determine the potential of these effects on the calibration procedure.

Head models used in this study ignored the volume conduction effects of the dura [148], blood vessels [149] as well as local skull inhomogeneities such as sutures, which could provide a path of higher conductance [87]). In addition, following [96], a fixed CSF

conductivity was assumed at 1.79 S/m at body temperature which is also nearly identical to the recommended weighted average mean value of 1.71 S/m of a recent meta-analysis [7]. In the latter study, however, a larger variability of CSF conductivity was reported when using MREIT instead of DAC for its determination (Fig. 8 in [7]). These are the main reasons why the terms “estimation” or “calibration” of skull conductivity have been consistently used in this study, since the term “determination” would have feigned too much precision. Despite these limitations, it is believed that the proposed procedure is a considerable step forward when compared to the current standard, i.e., the use of non-individual literature-based or only age-dependent skull conductivity values.

The conductivity ratio between skull compacta and spongiosa was fixed based on the measurements of [9], again with the main argument to avoid overfitting [29, 86]. First of all, skull conductivity calibration with such a fixed conductivity ratio for compacta:spongiosa has been successfully used in a proof-of-principle study for EMEG source analysis in presurgical epilepsy diagnosis [18]. Secondly, also the simulation studies of [5, 11, 79] support the use of skull modeling approaches that distinguish between skull spongiosa and compacta. However, it was also shown that this distinction causes only a weak effect in both EEG and MEG for the somatosensory cortex when using an optimized conductivity value for the homogenized full skull compartment (Fig.12 in [5]). Therefore, it is not expected that a calibration similar to the one presented here would be able to additionally estimate an individual ratio as a second degree of freedom. For the MEG, the observed effect on forward solutions was even much smaller compared to EEG (Fig. 12 in [5]), and since the first step of calibration procedure uses the MEG for the localization part, it is not expected a high sensitivity of the calibration procedure on the chosen ratio. Skull conductivity calibration could also be performed using a homogenized full skull compartment, which would lead to a calibration value reflecting the combined effect of both compartments. Because of the overall weak effect of the spongiosa compartment on EEG and especially MEG forward solutions for somatosensory sources (Fig. 12 in [5]), it is expected only moderate changes in the calibration value.

5 EMEG Source Analysis and TES Modeling of an Epilepsy Patient with Cranial Burr Holes

In this study, EMEG source analysis is performed for the localization of irritative zone in a patient with supposedly non-lesional left frontal lobe epilepsy. It is hypothesized that the quality of source reconstruction is influenced by the accuracy of head modeling, especially by modeling of cranial burr holes, head tissue compartment homogenizations and the use of anisotropic or individually calibrated conductivities. All head models are compared using either EEG or MEG alone, or combined EMEG, assuming that EMEG should be more accurate than each modality alone. Localization results are compared at the middle of the rising flank of the spike and at the very onset of the spike, assuming that source reconstruction at the very spike onset should deliver the more meaningful result. A comparison of source localizations from three commonly-used inverse methods is presented. Finally, individually targeted and optimized multi-channel TES is examined as alternative of epilepsy surgery taking into account head modeling effects.

All figures presented in this Chapter were obtained with custom MATLAB codes, Scirun, and CURRY 8.

5.1 Patient and Methods

5.1.1 Ethics Statement and Patient

The patient consented that her clinical data may be used for scientific publications in anonymized form. All procedures have been approved by the local ethics committee, as well as by the ethics committee of the University of Erlangen Faculty of Medicine on 20.02.2018 (Ref No 4453 B).

In this study, a twenty-year-old female patient is reported with normal intellectual state and without focal neurological deficits. The patient has had epilepsy since the age of 14, with a seizure semiology described as distributed thinking and inability to speak or follow a conversation, without any motor symptoms and without impairment of awareness. The frequency of seizures was four times per day. There have never been any seizures with loss of consciousness or tonic-clonic seizures (grand mal) [17]. The patient did not become seizure free despite treatment with multiple anticonvulsant drugs, including levetiracetam, lamotrigine, and oxcarbazepine. Levetiracetam was not tolerated because of psychiatric side-effects (aggressiveness, drowsiness); lamotrigine induced myoclonus as a side-effect.

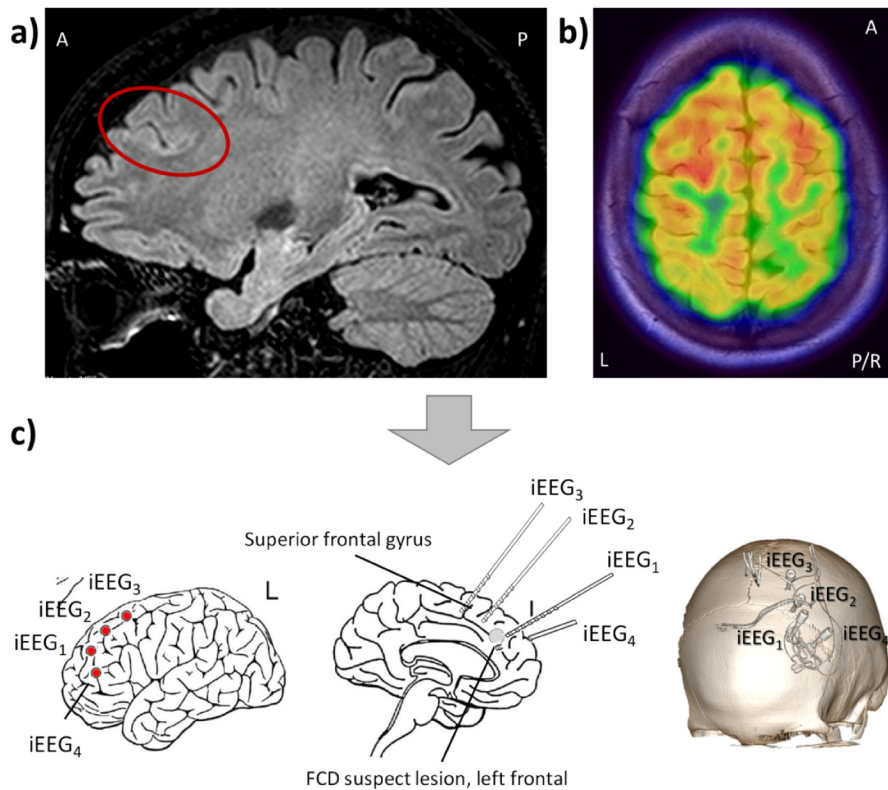


Figure 5.1: Results of non-invasive presurgical workup and planning of the invasive EEG study: **a)** a sagittal view of the 3D-FLAIR MRI at that time which was reported as normal, but with a suspicious, unusually deep sulcus in the middle frontal gyrus (area in red circle); **b)** hypometabolism in the left superior frontal gyrus on fluorodeoxyglucose positron emission tomography (FDG-PET), suggesting a possible functional deficit zone; **c)** depth electrode placement for the invasive video EEG study (electrodes named iEEG₁, iEEG₂, iEEG₃ and iEEG₄). The electrodes were implanted into the suspicious deep sulcus and the left superior frontal gyrus. Abbreviations Anterior (A), Posterior (P), Left (L) and Right (R) declare orientation.

Despite the rather mild semiology, the patient was highly disturbed by the seizures. As the patient met the criteria for pharmacoresistance, a presurgical evaluation for possible resective epilepsy surgery was done.

During an initial non-invasive video-EEG monitoring, with surface electrodes applied according to the international 10-20 system with additional anterior-temporal and basal-temporal electrodes, electrographic seizure patterns (3 to 5 per day) were recorded, originating in the left frontal area (F3 maximum). Of note, the seizure patterns consisted of evolving surface-positive spikes, suggesting seizure onset in an area of cortex oriented in a way that deep cortical layers project towards the skull surface. The FLAIR (Fluid-attenuated inversion recovery) MRI at that time (3D-FLAIR at 3T with voxels of $1 \times 1 \times 1 \text{ mm}^3$) was reported as normal, but with a suspicious, unusually deep sulcus in the middle frontal gyrus (Figure 5.1a). When estimating voxel-based morphometry maps (VBM) [150] using T1w-MRI, no clear evidence for an FCD was indicated. Fluorodeoxyglucose positron emis-

sion tomography (FDG-PET), on the other hand, showed a slight hypometabolism in the left superior frontal gyrus, suggesting a possible functional deficit zone (Figure 5.1b). Neuropsychological tests was reported normal with no deficit. In order to further improve the hypothesis regarding localization of the epileptogenic zone and to guide optimal electrode placement for an invasive EEG evaluation, a first 40 minutes EMEG recording was done during which the patient was awake. The acquisition protocol was the same as described in 5.1.2. Unfortunately, there were no spikes, sharp waves, or seizure patterns recorded. Thus, the implantation of the invasive EEG electrodes was planned based on the evidence derived from non-invasive video-EEG, MRI, and FDG-PET alone. Four invasive electrodes (iEEG₁, iEEG₂, iEEG₃ and iEEG₄, Figure 5.1c) were implanted into the suspect deep sulcus and the left superior frontal gyrus. There were eight electrographic seizures recorded, beginning with rhythmic alpha activity in one contact of the depth electrode implanted into the suspect sulcus (iEEG₄, contact 5), evolving into rhythmic theta, and spreading to the neighboring electrode contacts. However, interictal epileptic discharges (IED) were very infrequent (maximum at iEEG₄, contact 5). Both infrequent interictal spikes and seizure patterns starting with rhythmic alpha instead of low-amplitude fast activity were considered clues that the actual epileptogenic zone was not captured and that the recorded seizure patterns represented spread patterns. Hence, the invasive evaluation was not conclusive, with the actual seizure onset considered very close, but with some distance to contact 5 of electrode iEEG₄. For this reason, the depth electrodes were explanted without resection. Instead, another anticonvulsant drug was recommended, and the patient was discharged on monotherapy with lacosamide. A year later, the patient was still not seizure-free. So, a second EMEG recording was scheduled (detailed information is given in section 2.4). This time, anticonvulsant drugs were withdrawn 3 days before the recording. The patient was sleep-deprived in order to provoke epileptiform discharges. This time, over 1000 interictal spikes were recorded within 40 minutes of recording time, with a maximum in the left frontal region. These were used for combined MEG/EEG source analysis. As the recording was done a year after the invasive video EEG evaluation with depth electrodes, there were four burr holes in the skull overlying the left frontal lobe. A hypothesis was that these burr holes would affect the results of source reconstruction. Therefore, one of the goals of this study was to evaluate the impact of these skull holes on the results of source localization using different realistic head volume conductor models.

5.1.2 EEG/MEG Acquisition and Preprocessing

Six EEG and MEG recordings were acquired using the same experimental setup as described in Section 3.1.2. The first run was as SEP/SEF data elicited by EW stimulation (see Section 3.1.3) for calibration purposes (Section 3.1.7.3). The remaining five runs were about the measuring of spontaneous activity with the goal to detect IED. Thus the patient was advised to relax and close her eyes. Each of those runs was 8 min long. The sampling rate was at 2400 Hz for all measurements in order to record highly oscillatory epileptic activity.

The preprocessing all of the measurements consist of baseline-correction, filtering and reduction of the non-cerebral activity. Similar preprocessing was applied on the SEP/SEF described in Section 3.1.5. The rest of measurements were first baseline corrected and a digital band-pass filter was used from 1 to 100 Hz. A reduction of non-cerebral activity was performed in CURRY 8 in which ocular and cardiac artifacts were detected based on a matching of those signals with the recorded EEG ocular and cardiac activity. A visual inspection was followed for each EEG/MEG modality before the exclusion of the candidate non-cerebral activity.

5.1.3 Spike Detection

Epileptiform spikes were manually identified and marked by two experienced epileptologists on the artifact-free EEG and MEG continuous data. For the EEG modality, a common average montage was used. The two evaluators marked 1050 spikes, which were selected for further analysis. The individual spikes were aligned (Figure 5.2, black solid vertical line) using the F3 electrode as reference since it presented the highest negativity compared to all the rest of channels (Figure 5.2, lower row). Through a custom MATLAB tool [44], every hand-marked position was examined for possible shifts right to the peak of the maximum negativity of each epileptic spike, whereby all markings were ensured to be at the same propagation phase of the epileptic activity. The continuous EEG and MEG data were then divided into spike epochs with 400 ms (200 ms before and after the spike peak). Finally, the EEG and MEG noise covariance matrices were calculated in the time range of -200 up to -50 ms before the spike peak.

The butterfly plot of a grand average across all spikes is presented (Figure 5.2, left column) for EEG (in blue) and MEG (in green). The corresponding EEG and MEG scalp topographies (Figure 5.2, right column) are presented for the time points of interest at -6.25 ms, i.e., the middle of rising flank of the spike peak or *spike upstroke*, and at -10.83 ms, i.e., *spike onset*.

5.1.4 Image Data Collection and Processing

The MRI dataset of the present patient included T1w, T2w and DTI data using the same MRI system and scanning protocols as described in Section 3.1.4. In addition to those MRI images, FLAIR MRI (turbo spin echo pulse sequence (TR/TE/FA = 5000/388 ms/90°, cubic voxels, 1 mm edge length)) was collected. Cranial Computed Tomography images (CT, Siemens SOMATOM Definition) were scanned, guiding the electrode placement the invasive EEG evaluation. Slices from the corresponding FLAIR and CT images are presented in Figure 5.3b. A brain suppression is observed in the CT images due to the implantation of the depth electrodes (Figure 5.1a). These electrodes were removed one year before the MRI scanning (see Section 5.1.1). Thus, patients' brain was no longer suppressed as presented in Figure 5.3a.

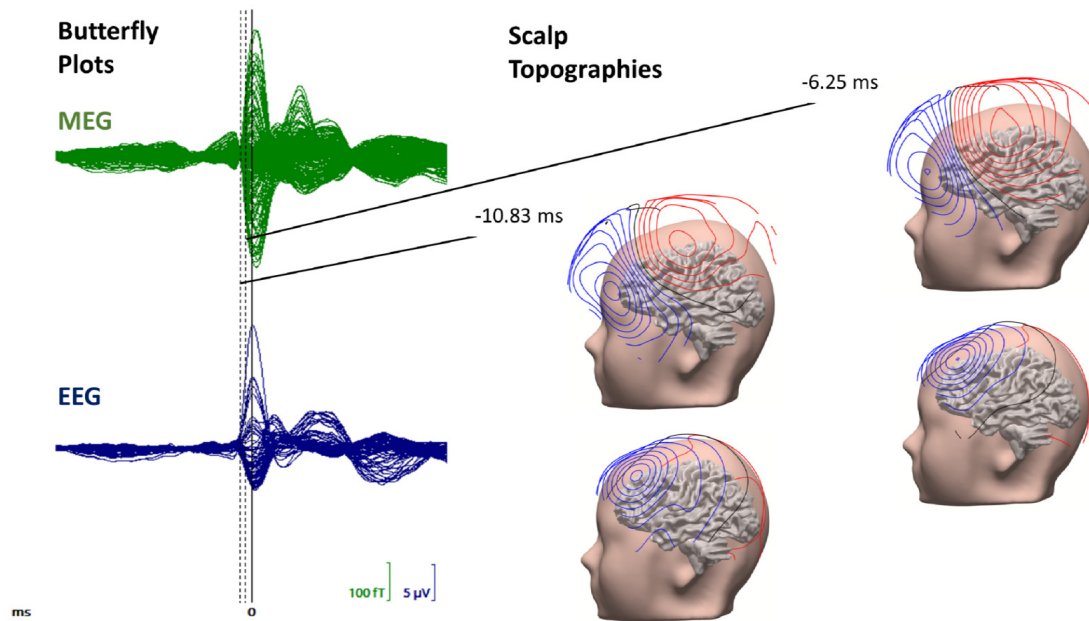


Figure 5.2: Grand-averaged MEG and EEG spikes: Butterfly plots (left) and topographies (right) of MEG (upper row) and EEG (lower row) for the average across the 1050 individual spikes. The time points of interest are indicated with black-color vertical dash lines. The scalp topographies are presented on the patient's head model. The peak of grand-average is at 0 ms as pointed by the solid black vertical line in the butterfly plots while the presented amplitude range is in femto-Tesla (fT) and milli-Volt (μV) for MEG and EEG, respectively.

T1w and T2w were then used to construct individual 3C and 6C head models as explained in 3.1.6. The most detailed 6C model was then separated into a model including the four cranial holes (6CH) and a 6C head model without those cranial holes (6CNH). The CT images were used for an accurate modeling of the cranial burr holes in the 6CH. These images were first registered into the T1w using FSL. Then, the skull compacta (SC) and skull spongiosa (SS) with holes (SCH and SSH) were created by segmenting the skull burr holes in the SC and SS compartments manually using the software Seg3D¹. The location of the four holes was over the left frontal side of the skull bone. The holes had a average diameter of 6 mm (Figure 5.3c, left column). The created gap in these holes was filled with scalp compartment (Figure 5.3c, right column). The assumption was that after a year, the cranial holes would be filled with collagenous tissue that has the same conductive properties as the scalp. For the 3CH head model, the SCH and SSH compartments were merged into a single homogenized skull compartment with holes and the compartments CSF, GM and WM, into the brain compartment. The final head models (6CH, 6CNH and 3CH) were visually inspected for possible errors in Seg3D.

In the next image processing step, DTI data were processed to include white matter

¹Seg3D: Volumetric Image Segmentation and Visualization. Scientific Computing and Imaging Institute (SCI): <http://www.seg3d.org/>

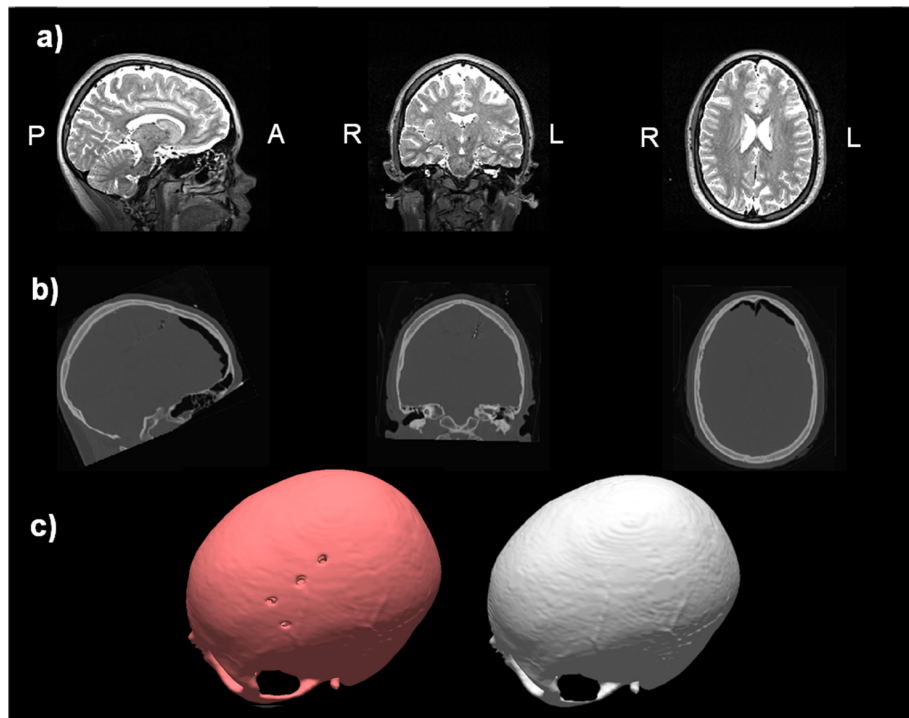


Figure 5.3: Patient's image data: Sagittal (left column), coronal (middle column) and axial (right column) slices of **a)** FLAIR MRI (upper row), **b)** CT (middle row) and **c)** the reconstructed surfaces of the skull with and without the burr holes (left and right column and light red and gray, respectively). Anterior (A), Posterior (P), Left (L) and Right (R) indicate MRI/CT orientation.

anisotropy in the head models as explained in Section 3.1.6.

5.1.5 Realistic Head Volume Conductor Models

In this study, the realistic head models were created using the labeled volumes as described in Section 5.1.4. Following the same steps as explained in Section 3.1.7, the resulting head models were the following: i) a three-compartment isotropic (3CIH) including a homogenized skull with cranial holes, brain and scalp and ii) a six-compartment isotropic with a) cranial holes and isotropic white matter tissue (6CIH), b) without cranial holes and white matter tissue anisotropy (6CANH), and c) with cranial holes and white matter tissue anisotropy (6CAH). To model the WM anisotropic conductivity for the head models 6CAH and 6CANH, the effective medium approach was used as explained in 4.1.3.

The conductivities for the compartments scalp and CSF of 6CIH, 6CANH, and 6CAH head models, for the homogenized brain compartment of 3CIH head model were as those described in Sections 3.1.7.1. In this study, the conductivity of the homogenized skull compartment was 0.1 S/m for 3CIH following the recommendations of [79] resulting in the 3CIH_100. A calibration procedure was used for the individual estimation of skull

conductivity as described in Section 3.1.7.3. The procedure was carried out for the head models 6CAH and 6CANH resulting in the calibrated 6CAH_Cal and 6CANH_Cal with SC and SS conductivities 0.0041 S/m and 0.0148 S/m, respectively. The last head model was the 6CIH_41 that contained literature-based [3] SC and SS conductivities which were similar to the calibrated ones for this patient.

5.1.6 Source Reconstruction of Epileptic Activity with Sub-Averaging

In the present source reconstruction “sub-averaging” approach (see Section 2.4.7), the focus was on the trade-off, improving SNR and keeping information about the extent of active cortex.

The source reconstruction sub-averaging approach starts with the calculation of a source space similar to the one described in Section 3.1.8. The SimBio software was used to calculate the forward solutions of EEG and MEG with the solver described in Section 3.1.9.

Subsequently, a bootstrap like inverse procedure was performed to estimate a cluster of dipole sources. This procedure starts with the calculation of a set of random realizations. In this study, the set size was equal to the total number of the spikes (i.e. 1050). Each realization is an average of ten randomly selected spikes following the suggestions of [47] while it is ensured each generated combination of individual spikes is unique for each realization. The SDS inverse algorithm is selected (see Section 3.1.10) for the estimation a dipole source on each realization. The performance of SDS is compared to current density approaches WMNE and sLORETA (Section 2.4.5). For each one these inverse methods, the dipole with the maximum magnitude from the estimated current density distribution is considered as the dipole source.

After the application of each inverse method on each realization, the so-called *centroid dipole* was defined by the mean location and orientation of the dipole sources that survived a two-step procedure. The first step is about the exclusion of low-quality dipole sources based on a thresholding to the SNR and RV values. In this study, the corresponding thresholds were adapted to be 2 for SNR and in the range of 20 to 30 % for RV. Then, a distance matrix is calculated among all the remaining dipoles of the previous thresholding for the preservation of dipoles with very close location. The determined threshold is the mean plus two times the standard deviation of the distance matrix. Finally, the centroid and the ellipsoid are calculated based on the remained dipoles after the thresholds. Further details are provided in [44].

While all electrodes of EEG were used on the source reconstruction sub-averaging approach, the corresponding MEG gradiometers were weighted non-uniformly. This weighting was carried out to improve the SNR of the MEG data for better source reconstructions in the region-of-interest. The non-uniform weighting was performed by modifying the covari-

ance matrix of the MEG so that the specific set of gradiometers (123 out of 275) would influence the source analysis in a larger degree compared to the rest of gradiometers.

To enable EMEG source reconstruction, an SNR transformation was performed on both EEG and MEG as described in Section 3.1.10 converting them to unitless measurements. The data were whitened according to the noise level (estimated from the pre-trigger interval -200 ms to -50 ms) of each channel.

5.1.7 Alternating Direction Method of Multipliers

Optimized TES is examined in this study with the goal to use it as an neurotherapeutic alternative of surgery (see Section 2.6). The optimization algorithm “alternating direction method of multipliers” (ADMM) [127] was used in this study. With the side-constraints of this algorithm, one can reach high focality in the target region that is important in order to not affect non-target regions. Based on the introduced notations of Section 3.1.11, a description of ADMM is stated as

$$s_{opt} = \max_s \int_{\Omega_e} \langle K_e s, e \rangle dx - a \int_{\Gamma} s^2 \Omega dx - \beta \|s\|_{L^1(\Gamma)} \quad (5.1)$$

$$\text{subject to } w|K_e s| \leq \varepsilon \text{ and } \|\tilde{s}\|_1 \leq 4$$

where the parameters α and β are the L_1 and L_2 regularizations, respectively. The state constraint $w|K_e s| \leq \varepsilon$ was introduced for fulfilling the safety constraint and minimizing the current density in the non-target regions, where ε was set to 0.5 and adapted based on the weighting matrix to be more abundant in the target region than in non-target regions. The condition $\|\tilde{s}\|_1 \leq 4$ described the L_1 -norm of \tilde{s} and limited the total current.

The optimization algorithm was applied twice to reach the highest possible current on the eight available stimulation electrodes in this thesis. The ADMM was first performed to estimate s_{opt} using all 38 electrodes. Then, eight electrodes with the maximum absolute injected current were selected and the ADMM was applied again. The selection was balanced, having four positively and four negatively current-weighted electrodes. In the second ADMM run, the s_{ref} was equal to the minimum absolute current from the initial optimization scheme per head model.

A comparison about the influence of head modeling on orientation and amplitude of the modeled currents was performed using the following metrics:

$$Ang(i) = \arccos \frac{\langle \vec{j}_1(i), \vec{j}_2(i) \rangle}{\|\vec{j}_1(i)\| \|\vec{j}_2(i)\|} \quad (5.2)$$

$$Amp(i) = \frac{\|\vec{j}_1(i)\|}{\|\vec{j}_2(i)\|} \quad (5.3)$$

In the equations above \vec{j}_1 and \vec{j}_2 represent the current densities in the compared head

models and i is the element in which this comparison was made.

The quantification of the present TES optimization quality was done using four metrics as introduced in [104]: averaged current density (A/m^2) in the target region or *intensity in the target region* as $IT = \frac{\int_{\Omega_e} |K_{es}| dx}{|\Omega_e|}$; averaged current density (A/m^2) in the non-target regions or *intensity in the non-target regions* $INT = \frac{\int_{\Omega \setminus \Omega_t} |K_{es}| dx}{|\Omega \setminus \Omega_t|}$; inner product of the current density and the target vector to formulate the directionality (A/m^2) of the current density to the target vector as $DIR = \frac{\int_{\Omega} \langle K_{es}, e \rangle dx}{|\Omega_e|}$; focality of current density in the target region as $FOC = \frac{IT}{INT}$.

5.2 Results and Discussion

This section is divided into four subsections. Results are presented and discussed. The first subsection includes the investigation of the hypothesis that EMEG source reconstruction is more accurate than EEG/MEG source reconstruction. The second subsection shows head modeling effects on source reconstruction. For these two sections, the sensitivity comparisons are expressed in terms of location and orientation differences as well as strength reduction as described in Section 3.2.3. The last subsection reports head modeling effects on optimized TES channel montages.

5.2.1 Effects of EMEG Source Analysis on the Detection of the Focal Cortical Dysplasia

5.2.1.1 Source Analysis Comparisons

The source reconstruction comparisons were performed at the spike onset (-10.83 ms) and spike upstroke (-6.25 ms). The most detailed head model (6CAH_Cal) was used for these evaluations. The corresponding source reconstructions are presented in Figure 5.4 while Table 5.1 describes the source reconstruction differences. Table 5.2 provides information relative to the source reconstruction quality.

At the spike onset, all centroid dipoles were localized in deep areas of the left frontal cortex (Figure 5.4a). The EMEG dipole centroid (Figure 5.4a, dipole source in red) was located at the bottom of sulci-valley on the left frontal cortex. This dipole was in the middle of EEG and MEG dipoles with a distance of 9.6 mm and 4.2 mm, respectively. The EMEG orientation component pointed radially inwards to the cortex. This component differed very little from the corresponding EEG dipole (18.7°) but very much from the MEG dipole (66.9°). As to the source strength differences, the one for the EMEG dipole was moderately closer to the one of EEG dipole (-14.3 %) than the one of MEG dipole (73.8 %).

At the spike upstroke (Figure 5.4b), all centroid dipoles shifted to more superficial

Table 5.1: Source analysis effect due to changes in the measurement modality for the most detailed head model: Differences in centroid location (third column), orientation (fourth column) and strength (fifth column) between measurement modalities (second column) for the F3 spike cluster at the latencies of interest (first column) when the most detailed head model (6CAH_Cal) was used.

Latency (ms)	Modality Pair	Location Diff. (mm)	Orientation Diff. (degree)	Strength Diff. (%)
	EMEG vs. EEG	9.6 (9.3)	18.7 (8.1)	-14.3 (-13.9)
-10.83 (-6.25)	EMEG vs. MEG	4.2 (0.6)	66.9 (73.8)	57.1 (64.2)
	EEG vs. MEG	10.3 (9.7)	82.5 (74.1)	62.4 (68.6)

positions on the left frontal cortical region. Compared to the spike onset, EMEG centroid dipole was in the same location as the MEG centroid dipole (0.6 mm) while the distance to the EEG dipole remained constant (9.3 mm). The orientation component of EMEG dipole was even closer to the EEG centroid dipole (8.1°) and far away from the MEG dipole (73.8°). There were small strength reductions for all the centroid dipoles compared to the spike onset (Table 5.1, fifth column).

As presented in Table 5.1, EEG and MEG dipoles had a location difference at 10.3 mm and orientation difference at 82.5° . The source strength was 62.4 % higher for the EEG than the MEG centroid. Already from scalp topographies of the time points of interest, it got clear that MEG contained the tangential component of the mainly radially orientated epileptic activity (Figure 5.2, see scalp topographies). At -10.83 ms, a quite negatively monopolar potential pattern was observed over the left frontal side of the EEG cap while a dipolar spread field pattern appeared on the left frontotemporal side of the MEG sensors. At -6.25 ms, the monopolar pattern was less focal and shifted slightly to the EEG sensors placed in left centrofrontal side of the scalp while the MEG field pattern was less spread with a small orientation shift.

In Figure 5.4, it can also be observed that the ellipsoid diameter of the EMEG centroid dipole was always smaller (spike onset: 14 mm, spike upstroke: 7 mm) than the corresponding EEG (spike onset: 19 mm, spike upstroke: 15 mm) and MEG (spike onset: 20 mm, spike upstroke: 11 mm) centroids.

The source reconstruction quality was expressed in terms of SNR and GOF. In Table 5.2, the averaged value across the remaining dipole sources is presented (see Section 5.1.6). All modalities had low SNR in a similar range at the spike onset while SNR got higher at the spike upstroke (Table 5.2, third column). At the latter time point, MEG signals were of better quality than the other two modalities. A similar trend was observed for GOF (Table 5.2, fourth column) where values were 80 % for EEG, 74 % for MEG and 72 % for EMEG at the spike onset while they were higher (EEG: 91 %, MEG: 85 % and EMEG: 82 %) at the spike upstroke.

In accordance with the literature [1, 3, 4, 5], the present results are attributed to the different sensitivity profiles of EEG and MEG (Figure 5.2 and 5.4, Table 5.1). The presence of noise was high (Table 5.2) and the radially oriented origins of the FCD at the spike onset

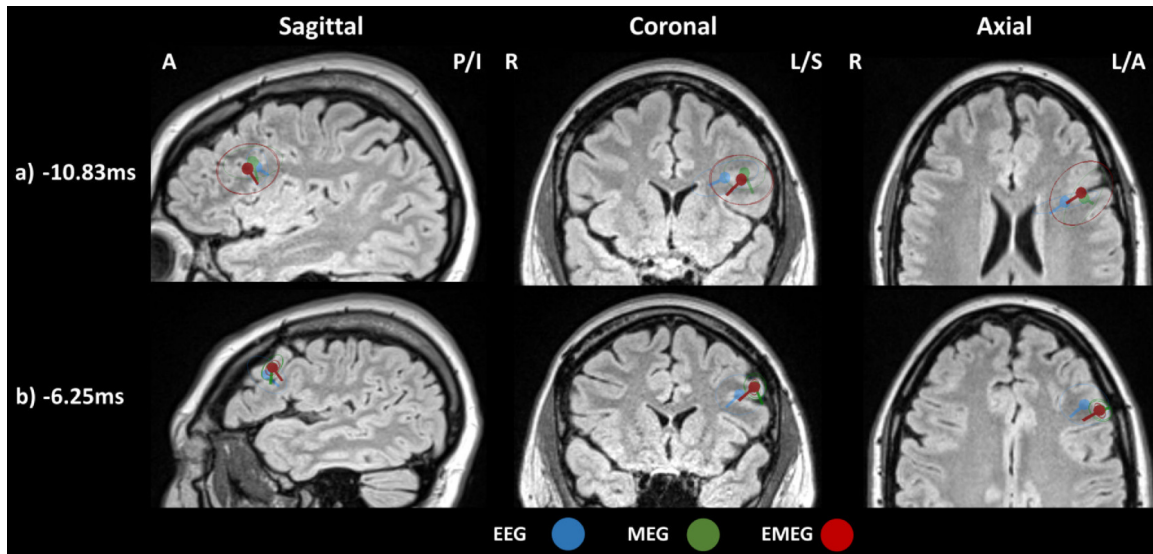


Figure 5.4: Measurement modality source reconstruction comparisons: Spike cluster centroids and spread ellipsoids are depicted on the FLAIR MRI views (sagittal (left column), coronal (middle column) and axial (right column)) at **a)** -10.83 ms and **b)** -6.25 ms. The centroid dipoles are presented for each modality (EEG: blue, MEG: green and EMEG: red) when the most detailed head model was used 6CAH_Cal. The MRI slices are presented for the position of the EMEG centroid dipoles. The size of all dipoles is kept constant. Anterior (A), Posterior (P), Inferior (I), Left (L) and Right (R) shows MRI orientation.

were the main reasons that made the MEG contribution to the EMEG source location less dominant than at the spike upstroke. Due to also the comparable SNR between EEG and MEG and the larger EEG source strength compared to the MEG one (Table 5.1), the contribution of EEG to the EMEG source location was not negligible. From the spike onset to the spike upstroke, a propagation of the epileptic activity to other regions was observed, affecting mainly the location of dipoles while the orientation component remained similar to the ones observed at spike onset (Figure 5.4). This propagation and the better MEG SNR (Table 5.2) brought EMEG and MEG dipoles to almost at the same location. Thus, the EMEG source location of the present case study involved both or single EEG and MEG depending on the selected latency. In the same line, Aydin et al. [47] proven that EMEG uses the complementarity of both EEG and MEG allowing accurate source localizations at very early time points before the spike peak. About the dipole moment (orientation and magnitude), EMEG dipole was significantly closer to the EEG than the MEG for both time-instants (Table 5.2). This confirms the major contribution of EEG to the EMEG dipole source determining orientation in the presence of a realistic head volume conduction model. In agreement with our results, Aydin et al., [44] presented orientation differences at 20° between EEG and EMEG and at 70° between MEG and EMEG. Besides, already from the scalp topographies (Figure 5.2), it is understood that EEG and MEG detect different activity from of the underlying cortical region. Therefore, the combination of the different sensitivity profiles of EEG and MEG contain valuable information that could lead to more

Table 5.2: Source analysis quality: Per time point of interest (first column) and measurement modality (second column). The quality of the source analysis is quantified by the signal to noise ratio (third column: SNR) and the Goodness-Of-Fit (fourth column: GOF).

Latency (ms)	Modality	SNR	GOF (%)
-10.83 (-6.25)	EEG	2.67 (4.5)	80 (90)
	MEG	2.61 (6.1)	74 (85)
	EMEG	2.6 (5.6)	72 (82)

accurate source reconstructions in presurgical epilepsy diagnosis.

The selected latencies (spike onset and spike upstroke) played an essential role in the determination of the FCD (Figure 5.4). Source reconstructions propagated to more lateral regions when shifting the time point from the spike onset to the middle of the rising flank of the spike peak. The present results confirm [47] in which it was shown that the EMEG source location was around the stereo EEG (sEEG) contacts while the dipole source spread to superficial regions when getting closer to the spike peak. In [18], the EMEG source reconstruction also indicated a second FCD in the left hemisphere of the patient at a very early time points before the spike peak.

In [151], it has been shown that during the epileptic spike waves, the activated cortical areas are focal with dynamic changes on their spatial positions within the epileptic tissue by using optical imaging on epileptic human neocortical slices resected during epilepsy surgery. These observations motivated us to follow recently developed procedures [47] for the determination of focal ellipsoids of the activated pattern within the epileptogenic zone that change due to the stochastic behavior of each spike. Therefore, the goal in this study was to estimate the extent of a cortical patch (see Section 5.1.6) in which the activity origin differs for each spike and not to estimate the extent of a patch with all neurons being active simultaneously and always in the same way.

5.2.1.2 Co-localization of Source Analysis and MRI

In Figure 5.4, EMEG source reconstruction and the patient's FLAIR MRI are illustrated side by side. Compared to MEG and to a smaller degree to EEG, EMEG reconstructed areas at -10.83 ms (Figure 5.4a) point to a highly grayscale contrasted region on the specific MRI slice (Figure 5.5b, area in red circle). Such a suspicious lesion is very likely to be a type 2b focal cortical dysplasia (FCD type IIb) which was not visible earlier by neuroradiological appraisal of the MRI study. The lesion was judged by the board-certified epileptologists (collaborators of this thesis) to be in very close proximity to Broca's area, so that a resection would be associated with a high risk of aphasia. Therefore, TES was considered as an alternative treatment option as presented in Section 5.2.4.

This is a major finding and of high clinical relevance in this study because when applying several other modalities (see Section 5.1.1), there was no clear sign for a cortical malformation. Following a similar EMEG source analysis, Aydin et al. [18, 47] also indicated

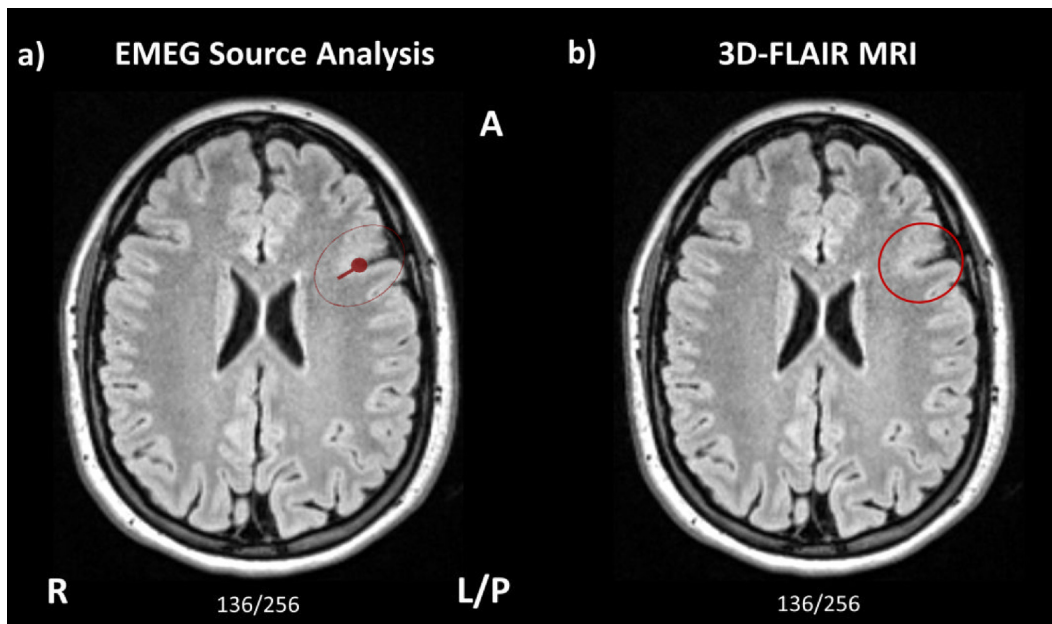


Figure 5.5: Indication of a cortical malformation based on source reconstruction result: **a)** The EMEG source reconstruction (red centroid and ellipsoid) at the spike onset (-10.83 ms) is presented when the SDS inverse method was used and the head model was fixed to most detailed 6CAH_Cal. **b)** Indication of a suspicious cortical malformation at the bottom of sulcus (center of the red circle). The slice number is indicated at the bottom of each image. Anterior (A), Posterior (P), Left (L) and Right (R) show MRI orientation.

cortical malformations eliminate for different patients. Combined EMEG source analysis in presurgical epilepsy diagnosis is also indicated in a series of recent studies [41, 48, 152] that analyzed a greater number of focal epilepsy patients but used less realistic head models. In this thesis, EMEG source analysis performance to determine the FCD was based on detailed head modeling with calibrated skull conductivity and white matter anisotropic tensors (6CAH_Cal), offering a precise indication (Figure 5.5b).

5.2.2 Influence of Head Modeling on Source Reconstruction

The effect of head modeling on source reconstruction of the epileptic activity is presented in this section. The time point was kept fixed at the spike onset (-10.83 ms) and the most detailed head model 6CAH_Cal was considered the reference head model. The different source reconstructions are presented in Figure 5.6 while Table 5.3 describes the corresponding differences.

For the MEG centroid dipole, simplifications on the detailed head model 6CAH_Cal had a minor impact on the source reconstruction of the epileptic activity (Figure 5.5b). However, the volume conduction effects and compartment simplifications had a substantial effect on both EEG and EMEG source reconstructions. The centroid dipole shifted to more lateral regions of the cortex (Figure 5.6a and c, left and middle columns) with moderate

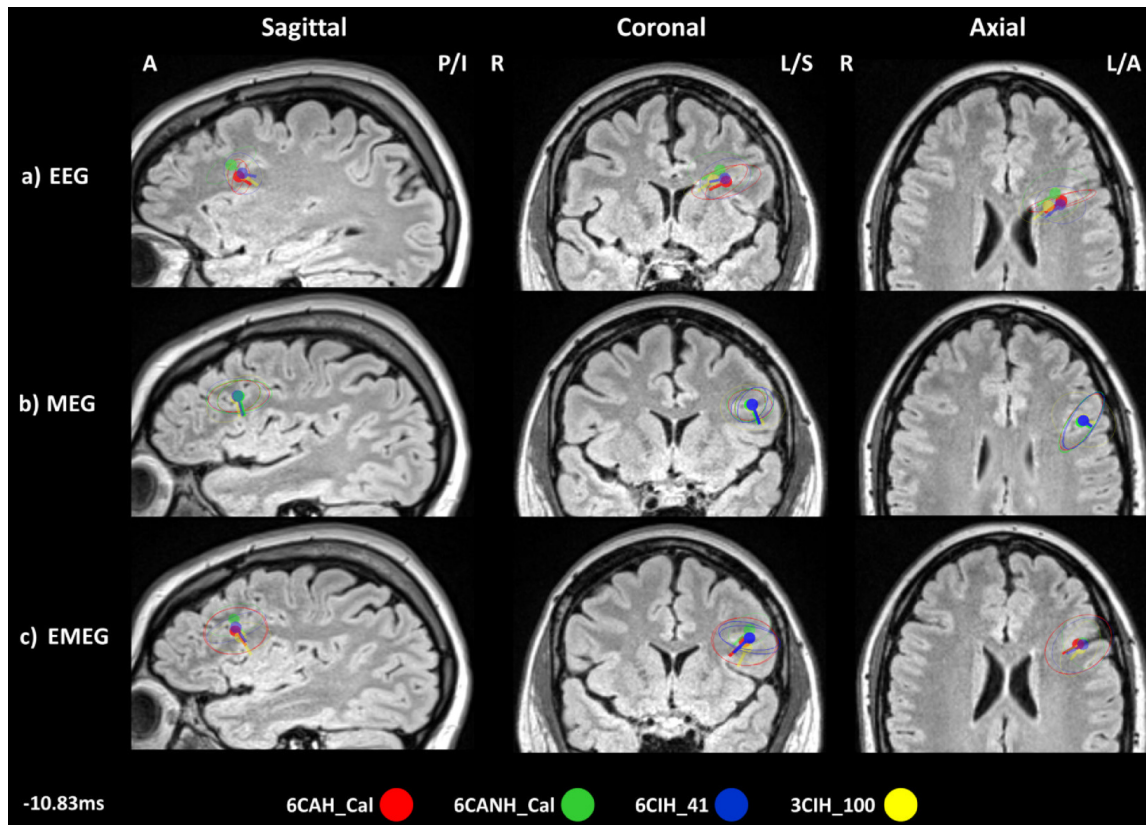


Figure 5.6: Head modeling effects on source reconstruction: a) The different head models used in the present study, the spike cluster centroids and spread ellipsoids (red for 6CAH_Cal, green for 6CANH_Cal, blue for 6CIH_41 and yellow for 3CIH_100) are depicted for a) EEG, b) MEG and c) EMEG at -10.83 ms. The source reconstructions are presented on the FLAIR MRI of the patient with sagittal (left column), coronal (middle column) and axial (right column) views. The centroid dipole locations of 6CHA_Cal were used for the selection of MRI slices and all results were projected on these slices. Anterior (A), Posterior (P), Inferior (I), Left (L) and Right (R) show MRI orientation.

changes in the orientation and strength for both EEG and EMEG when neglecting the modeling of the skull burr holes (6CANH_Cal: green dipole), and using the white matter isotropic conductivity (6CIH_Cal: blue dipole). Both EEG and EMEG centroid dipoles occurred in deeper cortical regions when brain and skull homogenizations were performed and the skull conductivity was set to the standard value of 0.1 S/m (Figure 5.6a and c, 3CIH_100 yellow dipoles).

The source reconstruction differences are reported in Table 5.3). For the centroid dipole comparison when using the head model 6CAH_Cal or 6CANH_Cal, the largest differences occurred for EEG (7.6 mm) and EMEG (6.4 mm) while the MEG dipole remained unaffected (0.2 mm). The orientation component was unaffected for EEG (1.8°) and EMEG (1.1°) but the source strength reductions was substantial for both EEG (-33.6 %) and EMEG (-18.3 %). Negligible differences occurred for the MEG source orientation (0.7°)

Table 5.3: Effect of head modeling on the evaluation of the epileptic activity: Differences in centroid location (third column: Location Diff. in mm), orientation (fourth column: Orientation Diff. in degree) and strength (fifth column: Strength Diff. in %) for the F3 spike cluster between the most detailed head model (6CAH_Cal) and every head model with less details are presented at -10.83 ms (first column) and every modality (second column: Modality).

Latency (ms)	Modality	Head Model	Location Diff. (mm)	Orientation Diff. (degree)	Strength Diff. (%)
-10.83 ms	EEG	6CANH_Cal	7.6	1.8	-33.6
		6CIH_Cal	2.5	12.6	-2.8
		3CIH_Cal	7	9.3	57.3
	MEG	6CANH_Cal	0.2	0.7	-0.3
		6CIH_Cal	1.4	4	-1.3
		3CIH_Cal	2.1	9.1	-11
	EMEG	6CANH_Cal	6.4	1.1	-18.3
		6CIH_Cal	3	2.1	4
		3CIH_Cal	4.1	18.8	81.2

and source strength (-0.3 %).

The comparison between the 6CAH_Cal and the 6CIH_41 revealed small source location shifts (EEG: 2.5 mm, MEG: 1.4 mm and EMEG: 3 mm) and source strength reductions (EEG: -2.8 %, MEG: -1.3 % and EMEG: 4 %). The source orientation differences were negligible for MEG (4°) and EMEG (2.1°) but large for EEG (12.6°).

As Table 5.3 shows, the source reconstruction comparison between the reference head model 6CAH_Cal and the standard isotropic 3CIH_100 head model demonstrated a smaller source location change for EMEG (4.1 mm) and MEG (2.1 mm) than EEG (7 mm). However, the EMEG dipole orientation showed the largest change (18.8°) compared to EEG (9.3°) and MEG (9.1°). Finally, the compartment homogenization caused moderate source strength reductions for EMEG (81.2 %) and EEG (57.3 %) and small for MEG (-11 %).

In this study, the influence of the cranial holes on source analysis was not high as in [80, 153] because the holes are relatively small and far away from the sensors. As it was deeply investigated by [80], the effect of local skull defects on the electric potentials are significantly high for sources in the vicinity of the skull defects. In [153] similar influences were highlighted for the magnetic field activity measured very close to the skull defects. In this work, the MEG sensors were not very close to the skull defects, and it is not clear if the influence is negligible on source reconstruction. Nevertheless the effect was visible for the EEG and EMEG source dipole location and strength due to the closest position of the EEG sensors to the cranial holes. A possible reasoning for these differences are the small diameter (approx. 6 mm) of the burr holes.

In previous studies [5, 125], it has also been also shown that the use of isotropic WM conductivity compared to anisotropic one has an important influence in the source strength and orientation. In the present study, the EEG dipole was in a deeper position than MEG

and EMEG dipoles. In the cortical region that the dipole was only determined with EEG, the presence of white matter anisotropy is higher and the currents are denser through the white matter fiber tracks [54]. Thus, the neglect of modeling white matter conductivity anisotropy can affect the orientation of deep source to a major degree. A non accurate source orientation could lead to misinterpretations of the epilepsy foci. For example, in [98], it was suggested that the source orientation component involves important localizational information for predicting the correct (epileptogenic) side of a sulcal wall.

In the last comparison, i.e., between 6CAH_Cal and 3CIH_100, the EEG dipole location is mainly influenced while MEG and EMEG remained less affected concordant to the literature [99]. A more considerable difference occurred in the EMEG source orientation component. An orientation error as the latter will influence the estimation of the epileptogenic side [98]. The major source strength absorption was due to the depth bias [5] caused by the high selected conductivity (e.g. 0.1 S/m for 3CIH_Cal) for the homogenized skull compartment. The present results are not surprising in epilepsy research [11] but they confirm that neglecting highly highly conductive (e.g. CSF) or resistive (skull compacta and spongiosa) compartments and using sub-optimal skull conductivities in the head model have a strong effect on the source reconstruction of brain activity [3, 53, 109].

To sum up, source analysis is a delicate procedure susceptible to simplifications of the head model. Calibrated and realistic head volume conductor models can improve the dipole location and moment so that the determination of the irritative zone is closer to the actual cortical patch.

5.2.3 Source Localization Comparisons

Source reconstructions with sub-averaging and different inverse algorithms are compared in the present section keeping fixed the time point at -10.83 ms and the parameters head model and modality at 6CAH_Cal and EMEG, respectively. The assumption was that the combination of these two parameters is the most integrated compared to the use of single modality EEG/MEG or less detailed head model. The dipole source differences due to different inverse problem method was investigated in terms of dipole source location difference.

Figure 5.7 shows the reconstructed epileptic activity on the FLAIR MR slices for three different MRI views (sagittal, coronal and axial). The sLORETA centroid dipole (in blue) was located deeper than the SDS dipole (in red) and their between-distance was 3.5 mm. When comparing the WMNE solution (in green) to the SDS solution, the WMNE dipole was in a 5.4 mm distant from the SDS dipole (in red). The WMNE dipole was superficially located in the sulci-wall compared to SDS and sLORETA solutions.

Both sLORETA and WMNE have shown promising results as reported by [99] on the reconstruction of the epileptic activity, showing location differences at 2.6 mm (6.6 mm) between SDS with sLORETA (WMNE). These location differences are in the same range as the results presented in this study. Therefore, these two methods could be a alternative

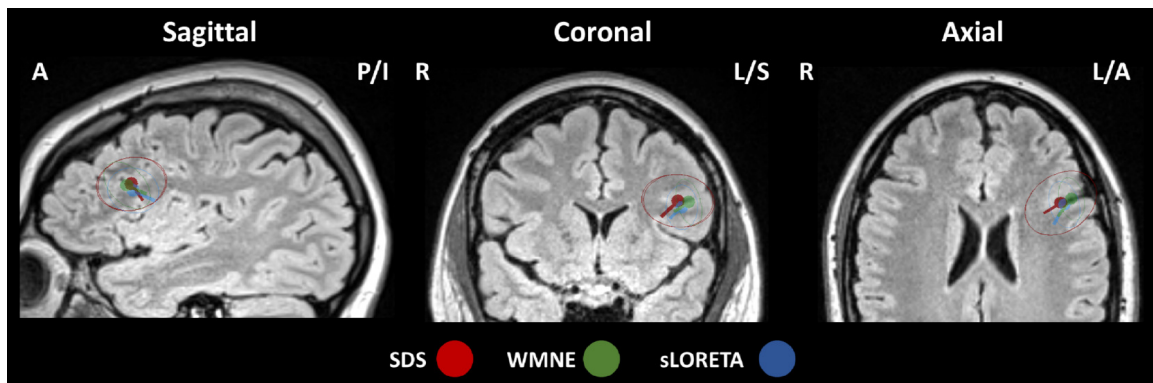


Figure 5.7: Comparison of difference inverse methods: Spike cluster centroids and spread ellipsoids for SDS (in red), WMNE (in green) and sLORETA (in blue) are depicted on the FLAIR MRI at the spike onset. The centroid dipoles are presented for the EMEG modality while the most detailed head model 6CAH_Cal was used. The SDS centroid locations were used for the selection of MRI slices. The dipole size was kept constant for all the dipoles. Anterior (A), Posterior (P), Inferior (I), Left (L) and Right (R) show MRI orientation.

of the SDS in the sub-averaging procedure utilizing the fast solution that these methods offer. However, it is known that current density approaches could deviate from the actual solution due to depth bias [60] as mentioned in Section 2.4.5. The use of these methods in source reconstruction with sub-averaging could serve an alternative of SDS but depth localization deviations should be taken into account in the interpretation of the final result. Novel inverse algorithms such Hierarchical Bayesian Modeling [60] could be also examined.

5.2.4 Optimized Multi-Channel TES in Focal Epilepsy

For the estimation of an individually optimized multi-channel TES montage, the EMEG source reconstruction was used as target vector (Figure 5.8b, black cone) in the ADMM algorithm. This source reconstruction provided the most meaningful information for the irritative zone 5.5 compared to the single modality (EEG or MEG) source reconstructions. Figure 5.8a shows the modeled current density mainly over the left middle frontal gyrus with asymmetrical expansions to the surrounding areas. In Figure 5.8b, the optimized TES montage is presented including the highest anodal (F7, T7, C3, Fp1 and AF3) and the lowest cathodal (AF7, FC5, and F3) stimulation electrodes after the second application of ADMM. The cathodal electrodes were mainly distributed in a circularly and the anodal electrodes surrounded them.

5.2.4.1 Head Modeling Effects on the Optimized TES

The effect of head modeling on the TES stimulation of the present epilepsy case is investigated. The most detailed 6CAH_Cal and most homogenized 3CIH_100 are selected in order to investigate differences on the optimized TES montages and electric fields.

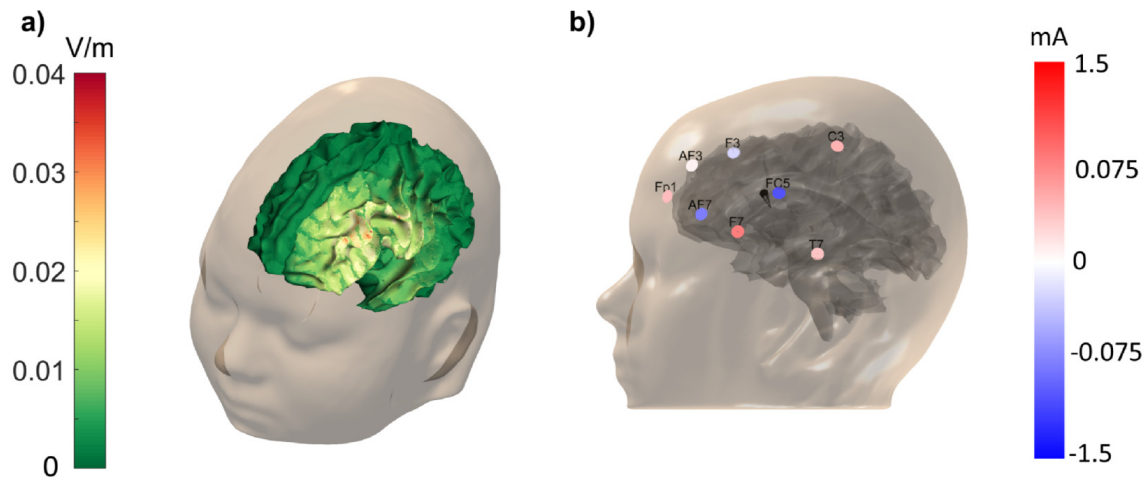


Figure 5.8: An alternative treatment option for the epilepsy patient: a) The current density distribution over WM surface of the patient. The color represents the current density distribution (in V/m). **b)** The individual optimized TES montage. Disk markers are used to represent the electrodes and they are color-coded with a range from -1.5 to 1.5 mA.

The optimized TES montage for the 6CAH_Cal had three electrodes as cathodes (FC5, AF7 and F3) surrounded by five anodes (F7, C3, Fp1, T7 and AF3) (Figure 5.9a). For the 3CIH_100, the anode electrode AF3 was replaced by an additional cathode electrode (P7) (Figure 5.9b). The rest of anodes/cathodes in the optimized TES montage were the same as 6CAH_Cal. The current amplitudes were observed substantially higher for 3CIH_100 than 6CAH_Cal (Figure 5.9), varying from -1.24 up to -0.1 mA and from 0.21 up to 0.81 mA for the cathodes and anodes, respectively.

In Figure 5.10, the current density distribution is presented after the ADDM optimization for both head models. The highest current density was observed over the left frontotemporal regions, which increased for 3CIH_100 compared to 6CAH_Cal (Figure 5.10b). The upper current density boundary was kept fixed at 0.04 A/m² for both the head models to make the effect of head modeling homogenizations easier comparable. For the 6CAH_Cal, the highest current density existed in the target region with a growing pattern around the target region (Figure 5.10a), region within the black rectangular) and varied from 0.02 up to 0.03 A/m². For the 3CIH_100, the simplifications to skull and brain compartments showed a strong influence on the simulated current density (Figure 5.10b) compared to the 6CAH_Cal. The current density distribution was above the visualization upper boundary in a substantially broader cortical patch around the target region compared to the 6CAH_Cal head model.

The quantification indices for the TES quality (see Section 5.1.7) were always higher for the 3CIH_100 than the 6CAH_Cal:

- $IT_{3CIH_{100}} = 0.08 > IT_{6CAH_{Cal}} = 0.03,$
- $INT_{3CIH_{100}} = 0.009 > INT_{6CAH_{Cal}} = 0.003,$

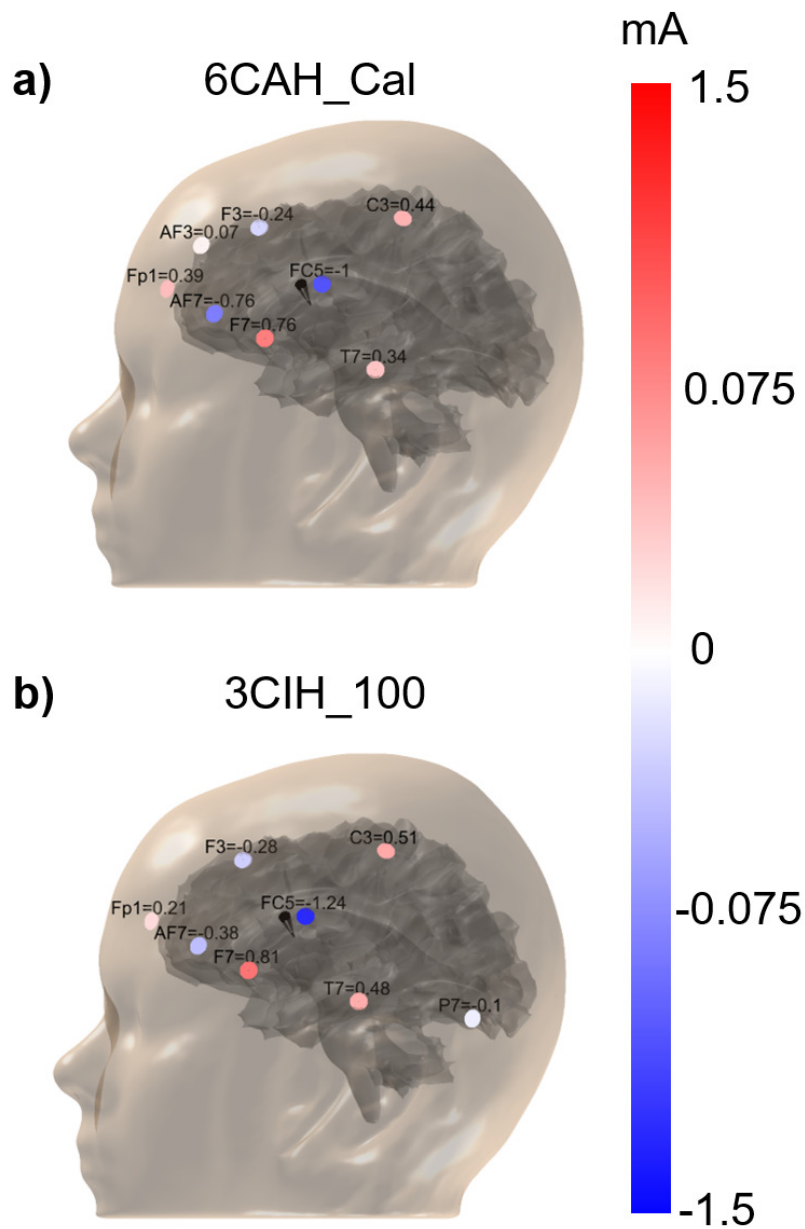


Figure 5.9: Effects on optimized TES montage due different head models: a) 6CAH_Cal and b) 3CIH_100. The optimally selected electrodes are represented by disk markers. The color-ranged is fixed to -1.5 to 1.5 mA for easier comparison of the difference in the optimized stimulation currents. The total sum of the injected currents is equal to 0 mA while the induced current is limited to 2 mA on each electrode to fulfill the safety constraint.

- $DIR_{3CIH_{100}} = 0.06 > DIR_{6CAH_{Cal}} = 0.02$).

Interestingly, the FOC index was higher for 6CAH_Cal than 3CIH_Cal ($FOC_{6CAH_{Cal}} = 10 > FOC_{3CIH_{100}} = 9$).

From the above mentioned TES results, it can be observed that the moderate head

model homogenization point to a homogenized distribution of the injected current density as well as the optimized TES montage. The main reason is mainly attributed to the use of single and homogenized skull and brain compartments with standard conductivities and the neglect of the highly conductive CSF and the one order of lower conductive three-layer skull. The present findings are in agreement with other studies [104, 132, 154]. The importance of modeling multi-layer skull and CSF compartment is also supported by results presented in Chapter 3 and previous studies about the modeling of the electrical forward problem [5, 14, 77].

The current density amplitude and orientation differences are presented in Figure 5.11 between the reference head model 6CAH_Cal and the 3CIH_100. The results are presented for the same axial slice using in Figure 5.10. The differences are reported for the gray and white matter, focusing on the effect of head modeling in the target region. For the amplitude differences, a value equal to one denotes no difference in the current density of the two examined head models. Any value below or above one denotes a higher amplitude for the reference or the simplified head model, respectively.

The current density amplitude was substantially higher for the 3CIH_Cal than the 6CAH_Cal head model (Figure 5.11a). The amplitude factor between the two head models was between 0 and 10. It is observed that this factor was close to 10 around the target region. The orientation differences in the current density of the two head models (Figure 5.11b), varied from 0° up to 100° . Those differences were high around the target vector, varying from 0° to 50° .

All in all, head modeling simplifications caused substantial current density overestimations and non-negligible effects on the individually optimized TES montages. These effects might result in misinterpretations for the application of optimized TES in the present epilepsy patient. Therefore, the use of a calibrated and detailed head volume conductor is suggested to model injected currents and optimized TES electrode montages realistically.

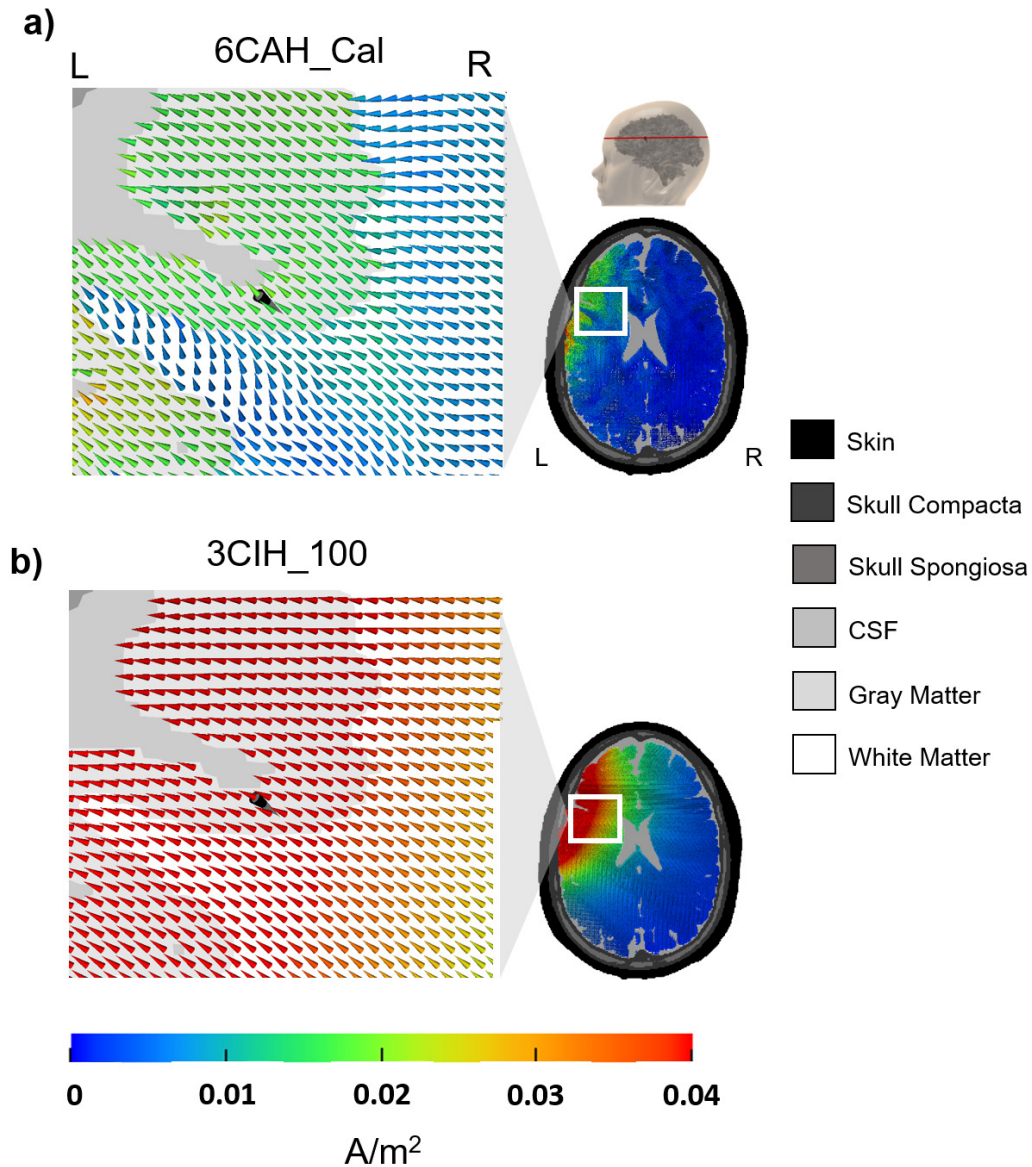


Figure 5.10: Effects on TES current density due different head models: a) 6CAH_Cal and b) 3CIH_100. The visualization is presented on an axial view of the segmented 6C volume. A red horizontal line across the head model presented in the right upper corner of **a)** indicates the position of axial slice in the target region. The illustrated zoomed target areas are outlined by a white square in the full axial slice. The target is represented by a black cone in those regions. Color-coded cones represent the distribution of the current density measured in A/m^2 . The cone scaling is fixed. Left (L) and Right (R) show MRI orientation.

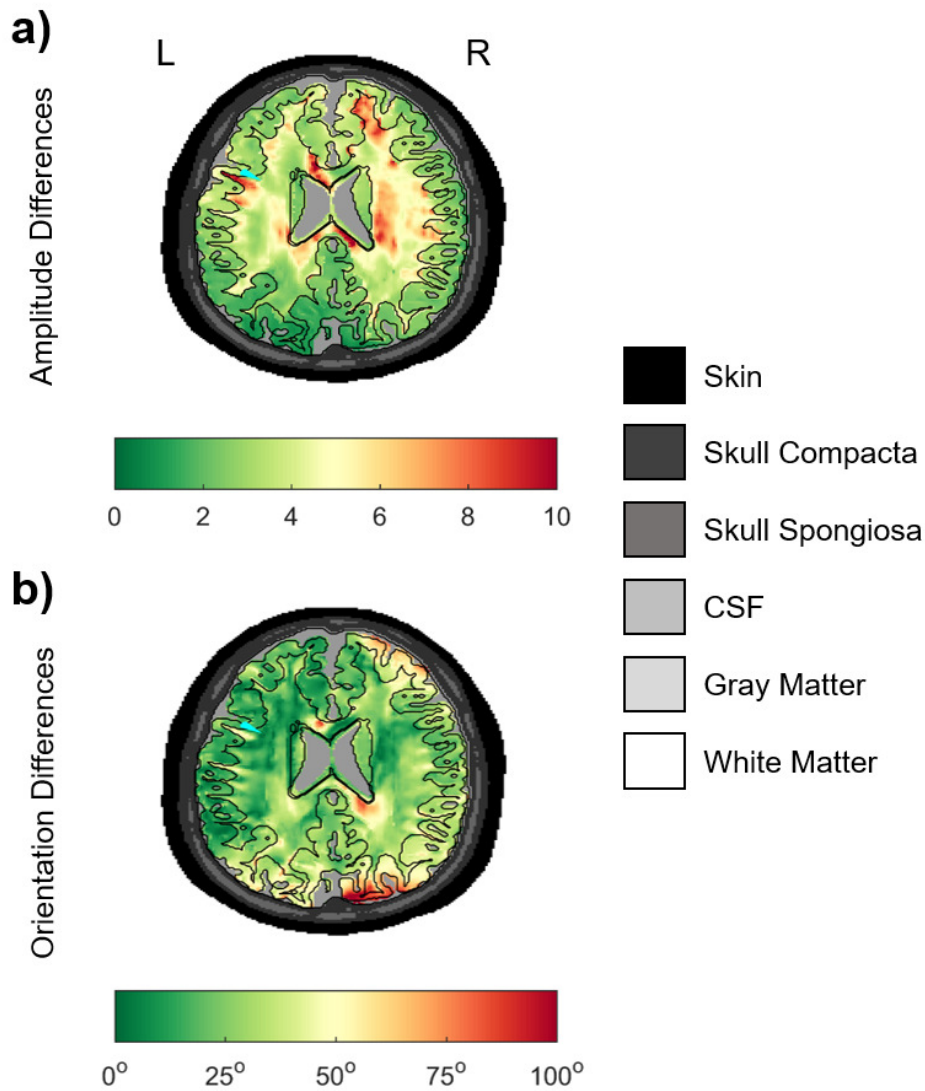


Figure 5.11: Current density differences for: a) amplitude and b), orientation between the head model 6CAH_Cal and 3CIH_100. The differences are presented in the axial slice, where the target vector exists (cone in cyan color). The results are restricted on gray and white matter to highlight differences at the target region. The colormap differs on each comparison to highlight better the differences in the specific regions. Black boundaries represent the distinction of different compartments existed in the 6CAH_Cal head model. Left (L) and Right (R) show MRI orientation.

6 EMEG Source Analysis of Epileptic Activity with Calibrated Head Modeling and Pattern Recognition

In this chapter, the study ([155]) is presented in which the author of this thesis had a contribution. EMEG source reconstruction was performed for characterizing the epileptic activity, paving the way on the utilization of the complementary information and avoiding the implications of invasive diagnostic techniques. Moreover, combination of two unsupervised algorithms for spike clustering is proposed with the goal to alleviate the problem of hidden patterns. Such patterns often have low SNR and thus, they could lead in detection of an epileptic focal area that is correlated with the seizure semiology.

6.1 Patient and Methods

6.1.1 Patient & Ethics Statement

The patient [18] signed all the appropriate consent forms, while the data were collected from both electrophysiological measurements and MR acquisitions.

6.1.2 Preprocessing of the Data

Initially, the filtering on the each EEG/MEG data were similarly applied as described in Section 5.1.2. To detect artifactual activity derived by physiological sources (such as cardiac or ocular activity), the filtered signals were decomposed using Principal and Independent Component Analysis and the components were selected to explain 95 % of the variance. The extracted independent components (ICs) were then submitted to an artifact detection plan consisting of 3 phases, the calculation of their Kurtosis, Entropy and Skewness based on [156], the visual inspection and the correlation with the channels recording non brain activity. The suspicious components were rejected if they were associated with cardiac or muscular interference. Alternatively, they were corrected if corresponding to ocular contamination, using the Empirical Mode Decomposition (EMD) [156].

6.1.3 Clustering of Epileptic Spikes

The measurements were evaluated by three certified epileptologists who marked 30 MEG and 36 EEG interictal epileptic spikes, along the 6 out of the 7 runs of the recording pro-

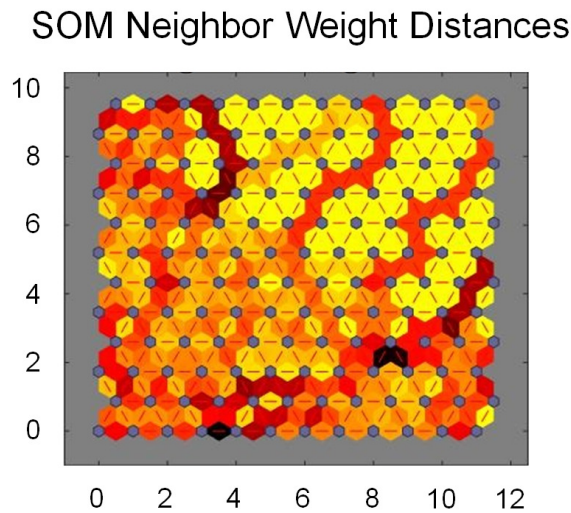


Figure 6.1: Weights Distribution for Feature Vector: The SOM network with node (in blue), the SOM neurons, which are compared with the feature vectors of samples in an iterative manner and are weighted reversely proportional to the respective distances. The dark colors represent large distances, while lighter colors represent smaller distances.

cedure. For each spike, each epoch defined with 200 ms before and after the spike peak for feature extraction described as follows. The representative features were extracted so as to be able to discriminate them or group them together in the clustering procedure. The selected features were Kurtosis, Entropy and Energy. Furthermore, a 4-level 2-Dimensional Wavelet decomposition with haar wavelets was applied selecting the first 10 wavelet coefficients with the greatest deviation from Gaussian distribution as features [155]. The selection of these coefficients was achieved with Lilliefors test (a modification of Kolmogorov-Smirnov test) [156]. Turning now to the clustering of the epileptic spikes after having constructed two feature vectors (EEG (36x13) and MEG Spikes Feature Vector (30x13)), we considered a two phase approach for clustering performing first Self Organizing Map (SOM) on a 12x12 grid (chosen by Vesanto rule). Generally, SOM produces a matrix along with a color codebook vector which stores the information of the assignment. Afterwards, the output of SOM (assignment to the grid and the color codebook vector) is fed to K-means trying different Ks as input (2-10). The clustering efficiency was evaluated with silhouette score which led to the optimal number of clusters for the 2 Feature vectors.

6.1.4 Source Analysis

The source reconstruction of the clustered EEG/MEG and EMEG spikes included a solution of the forward and inverse problem for a given volume conductor model of the head. A calibrated and realistic head model was produced based on the procedures described in Section 3.1.6 and 3.1.7. The EMEG reconstruction was performed by solving the inverse

problem using the EEG and MEG leadfields in a concatenated form along with a covariance matrix of the signals in the window between -20 ms and -5 ms for appropriate sensor weighting [3]. The localization performed at the rising flank of the spike to detect the onset of the epileptic activity and to avoid propagation [157]. For inverse source analysis, sLORETA was used (see Section 2.4.5). The timepoints selected for identifying the epileptic zones were set at: -23 ms, -17 ms, -13 ms, -10 ms, -8 ms, -5 ms, -3.3 ms and 0 ms. These time points were selected accordingly in order to gain insights into propagation phenomena for epileptic activity and to compare them with the related study of [18].

6.2 Results

6.2.1 Two-phase Clustering Approach

Figure 6.1 shows how the spikes are assigned to the SOM grid based on the distance of the nodes' weights from the feature vector of the spikes. Two light-yellow areas could be observed in the top right corner and one in the top middle, which indicates that the values of the spike feature vector are grouped into three regions which are clearly separated one to another from the red lines that traverse these groups. On the other hand, the information extracted from SOM is not easily grasped and this is one of the reasons why the output is not decoded through K-means.

The SOM output is fed to the K-means algorithm which was tested with the silhouette metric for various clusters ranging from 2 up to 10 but also for every cluster point for the selected K with the results summarized below.

By observing the evaluation of K-means, it cannot be stated that the optimal number of epileptic clusters is equal to three since it has mean value close to one but also the majority of the silhouette points of this cluster surpass the mean value. The last step before the source reconstruction is the averaging of the spikes which belong to the same cluster. In Figure 6.3 the signals produced for EEG and MEG clusters are visualized.

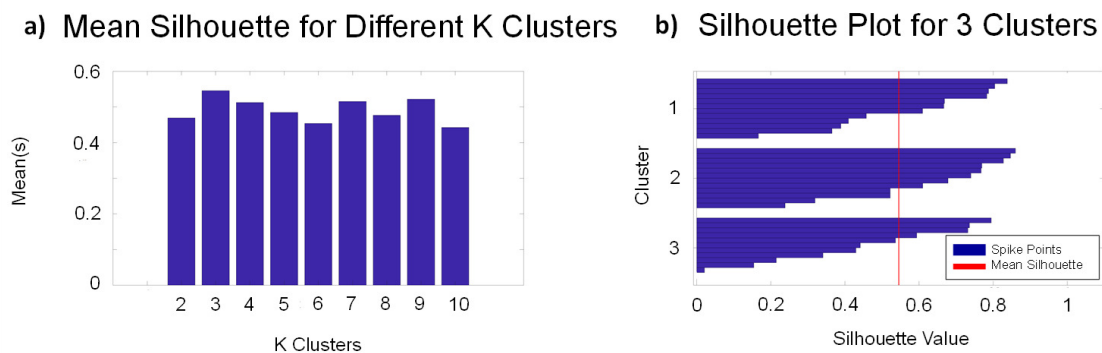


Figure 6.2: Evaluation of K-means clustering: a) Mean silhouette value for each K **b)** Silhouette values for K = 3.

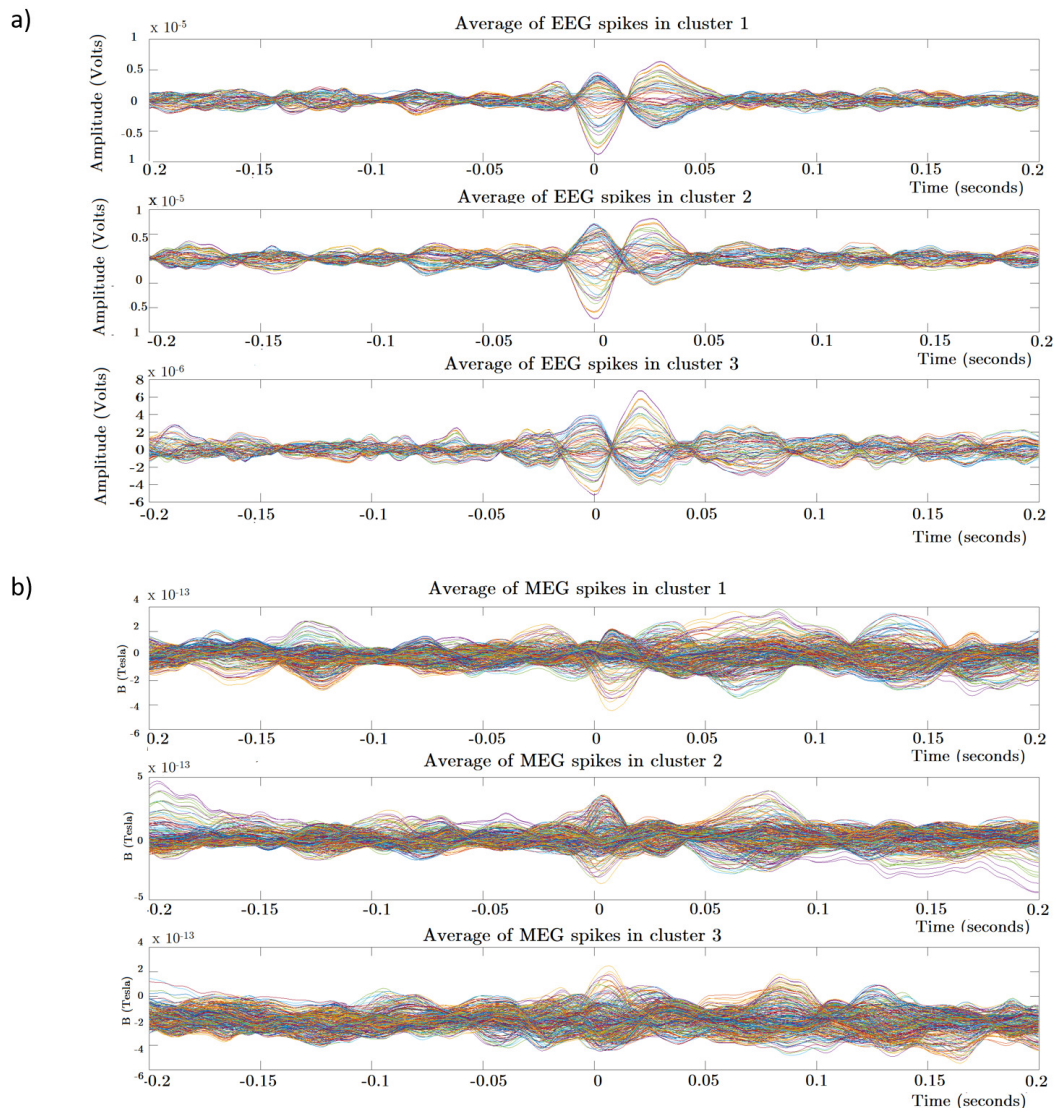


Figure 6.3: Subaveraged signals for: a) EEG and b) MEG based on two-phase clustering.

6.2.1.1 Combined EMEG Source Reconstruction

The inverse problem was solved using sLORETA for the 9 different combinations of the clusters and for each timepoint explained before. The visualization of the detected activity was depicted on the cortical surface by selecting a threshold of 85 % of the maximum F-value of sLORETA (red areas). Furthermore, the two FCDs were sketched in Figure 6.4 at the locations where MRI Zoom Imaging lesions were marked (black spheres). The output of the reconstruction for some of the clusters combination is outlined in Figure 6.4.

Figure 6.4 shows the reconstruction of the EMEG source in the frontal region near the right FCD, visualized for each time point before the peak. Figure 6.5 represents the results of sLORETA, for other cluster combinations for the detection of epileptic activity

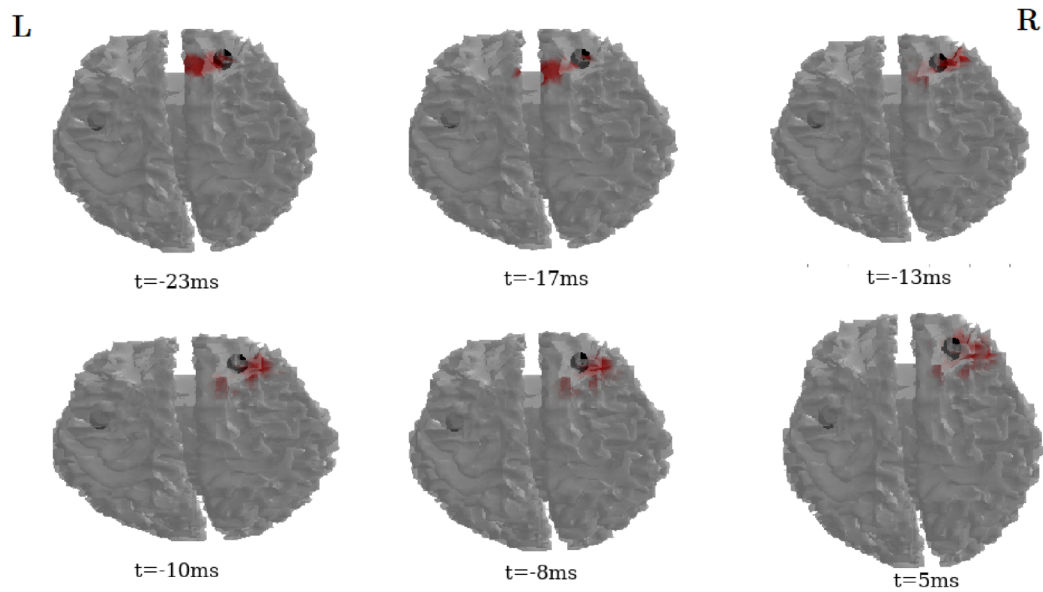


Figure 6.4: sLORETA combined EMEG source reconstruction for 2nd EEG & 2nd MEG cluster ($t=[-23,-17,-13,-10,-8,-5]$ ms).

in the vicinity of the right frontal FCD, at time-point -3.3 ms (a) and in the vicinity of the left frontocentral FCD at time-point -13 ms (b).

6.3 Conclusions

In this study the combination of Self Organizing Maps with K-means helped on disentangling the sources associated with two FCDs from which the subtle earlier one with low SNR could be reconstructed from combined EMEG data in the left frontocentral area, fitting well with the patient's semiology. The combined use of EEG and MEG in both data acquisition and source reconstruction paved the way for accurate reconstruc-

a) EMEG Source Localization 3rd and 3rd EEG Cluster: -13.3 ms b) EMEG Source Localization 2nd and 2nd EEG Cluster: -3.3 ms

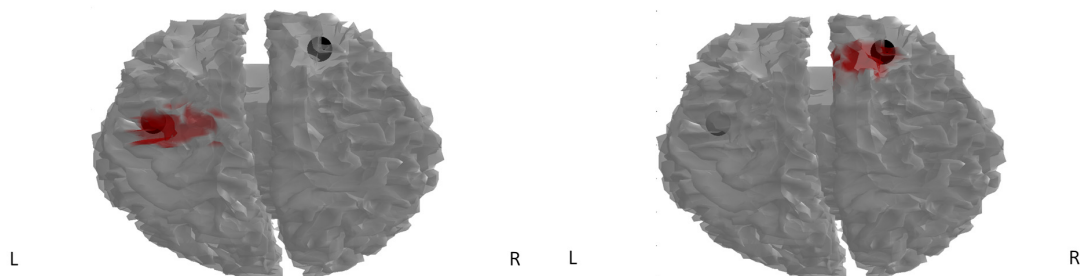


Figure 6.5: sLORETA EMEG reconstruction leads to FCDs detection: a) EMEG reconstruction 3rd EEG & 3rd MEG cluster at -13 ms and b) EMEG reconstruction 2nd EEG & 2nd MEG cluster at -3.3 ms.

tions of the epileptogenic zone, as proved by later sEEG and the surgical procedure using radiofrequency-thermocoagulation. The results presented in this study showed that combined EMEG source analysis using a calibrated realistic head model and a sophisticated spike clustering approach can be an important additional tool in presurgical epilepsy diagnosis. Hence, the main outcome of this study is a process pipeline that can be used to guide epilepsy diagnosis and treatment.

6.4 Author's Contribution

The contributions of the author to the studies described in this chapter are the following:

- Conceptualization of the main pipeline for the analysis of combined EEG/MEG data with a two-phase clustering approach.
- Provide MRI/EEG/MEG data with the recording protocols as described in [18].
- Realistic and calibrated head modeling for the subjects/patients used in this study based on the methods described in Sections 3.1.6, 3.1.7.
- Interpretation of results, writing and editing the corresponding sections in [155].

7 Conclusions and Outlook

In this thesis, we performed a series of group studies with combined EEG/MEG (EMEG) source analysis with detailed and individualized head modeling for first time. New methodology for image processing was developed to support this purpose as well as to model unusual skull defects for an epilepsy case study. Substantial influences were presented on the reconstruction of somatosensory and epilepsy activity as well as on the modeling of TES electric fields and optimized channel montages.

In Chapter 3, we presented that different stimulation types, measurement modalities and head modeling all have a similar and non-negligible influence on source analysis of the somatosensory P20/N20 component and the individually targeting and TES optimization of five healthy subjects. This study thus makes possible to record the effect sizes of modality and head modeling in comparison to the more easily understandable effect size of stimulation type. Using three different somatosensory stimulation types (EW, BT and PT), EMEG source reconstructions are less susceptible to forward modeling inaccuracies than single modality EEG or MEG and showed the importance of using highly detailed and individualized calibrated six-compartment FEM head models. Using the EMEG source dipoles based on the different stimulation type as targets in montage optimization and two-patch for TES, it was also observed the influence of inter-subject variability on the optimized electrode montages. While the MEG is the superior modality for P20/N20 localization, both EEG and MEG modalities contribute to the determination of source orientation and the estimation of individual skull conductivity. These modalities provide complementary information in combined EMEG that can be exploited based on detailed and individualized head volume conductor models. Combined EMEG with individual and detailed head modeling might lead to more stable source reconstructions as well as targeting in optimized TES even in the presence of unavoidable remaining modeling errors, and thus to an overall superior spatial resolution.

In Chapter 4, the inter-subject variability of skull conductivity was evaluated in the context of EMEG source analysis using a non-invasive refined calibration procedure applied on twenty healthy participants. This method is based on the reconstruction of the SEP and SEF P20/N20 component with subject-specific realistic head modeling. A large inter-subject variability was observed for the calibrated skull conductivity, as well as for the examined measures skull thickness, P20/N20 surface distance and source depth. The statistical analysis showed that the calibrated skull conductivity is significantly related to the skull thickness and age of the participants with no gender differences. In the context of source analysis of EEG or EMEG data and for optimized TES, this study emphasized the critical importance of taking the inter-subject variabilities of skull conductivity and thickness into account. Therefore, we propose the additional measurement of the individual SEP/SEF P20/N20 component and its use for subject-specific calibrated realistic head modeling. The

proposed procedure is non-invasive and easily applicable in a standard MEG laboratory.

In Chapter 5, an EMEG source analysis with realistic head modeling including cranial burr holes was performed for the localization of irritative zone of a patient with supposedly left frontal epilepsy. The results confirmed the clinical hypothesis for the existence of an FCD at the bottom of the sulci-valley when using EMEG source analysis and the most detailed head model. The localization was at the spike onset, avoiding the propagation of the epileptic activity for time points close to the spike peak. With regard to the head modeling effects on source reconstructing, modeling of cranial burr holes and white matter anisotropy as well as skull conductivity calibration are suggested to minimize source localization errors. Calibrated and realistic head volume conductor models do improve the dipole source for a better determination of the epileptogenic zone. Current density inverse methods can be a usable alternative of the SDS in the “sub-averaging” based source reconstruction. Due to the negative presurgical outcome, optimized TES was investigated as a possible alternative to suppress the epileptic seizures. A sensitivity study with head modeling modifications was performed showing large effects on the modeled electric field and the multi-electrode TES optimization. Moderate changes were observed in the modeled current density amplitude and orientation as well as on the optimized TES montage. These head modeling modifications might result unclear effects of TES in epilepsy.

Based on the results of this thesis and on the first clinical success in presurgical epilepsy diagnosis [18, 47], EMEG source analysis is highly recommended using detailed individualized realistic head models. The new software framework *Duneuro* [146, 158] can be used to facilitate individualized analysis, with accurate forward models, TES simulations and automatic calibration procedures. Currently, a calibration based on EW stimulation is still recommended. However, in order to investigate if the more comfortable BT stimulation might replace this standard, SNR, stimulator artifact and SEF source analysis differences due to different number of pins in BT stimulation (not shown here) have been investigated. These results motivated the use of the middle four out of eight pins that the BT stimulator offers. In a future study, it is suggested the investigation of the influence of different number and combination of pins in EEG and EMEG source analysis scenarios as well as the impact of the stimulation type on the calibration procedure.

The proposed calibration procedure in this thesis is a considerable step forward when compared to the non-individual literature-based or only age-dependent skull conductivity values. Still, further future investigations are needed to evaluate the sensitivity of the calibration procedure to these modeling simplifications. Comparison with EIT and/or combination with EIT procedures might also be interesting as future goals. Calibration procedures might be studied that exploit other SEP/SEF (left median nerve, tibial nerve, trigeminal nerve) or auditory or visually evoked potentials (AEP, VEP) and fields (AEF, VEF) data in order to calibrate other skull ROI's. Combinations of such calibration datasets might even allow the use of more than one degree of freedom in the calibration process, which, if presented alternately, need not even extend the measurement time.

The use of different subsets of individual spikes of different size in the “sub-averaging” source analysis procedure could be investigated. This investigation could also be evaluated for more epilepsy patients. A future goal would also be the application of the resulting optimized TES electrode montage based on the most detailed head model, to show whether, and at what level the epileptic seizures can be suppressed. EEG monitoring before and after TES application can be used for this purpose. The duration of TES application is also important and further investigation is necessary to define the optimal temporal window of the TES application. Finally, another interesting step might be about the evaluation of the effect of skull burr holes on the optimized multi-channel TES montages using discontinuous Galerkin FEM [146].

Bibliography

- [1] M. Hämäläinen, R. Hari, R. J. Ilmoniemi, J. Knuutila, and O. V. Lounasmaa, "Magnetoencephalography—theory, instrumentation, and applications to noninvasive studies of the working human brain," *Reviews of Modern Physics*, vol. 65, no. 2, pp. 413–497, 1993.
- [2] R. Brette and A. Destexhe, eds., *Handbook of neural activity measurement*. Cambridge: Cambridge University Press, 2012.
- [3] M. Fuchs, M. Wagner, H. A. Wischmann, T. Köhler, A. Theissen, R. Drenckhahn, and H. Buchner, "Improving source reconstructions by combining bioelectric and biomagnetic data," *Electroencephalography and clinical neurophysiology*, vol. 107, no. 2, pp. 93–111, 1998.
- [4] M.-X. Huang, T. Song, D. J. Hagler, I. Podgorny, V. Jousmaki, L. Cui, K. Gaa, D. L. Harrington, A. M. Dale, R. R. Lee, J. Elman, and E. Halgren, "A novel integrated MEG and EEG analysis method for dipolar sources," *NeuroImage*, vol. 37, no. 3, pp. 731–748, 2007.
- [5] J. Vorwerk, J.-H. Cho, S. Rampp, H. Hamer, T. R. Knösche, and C. H. Wolters, "A guideline for head volume conductor modeling in EEG and MEG," *NeuroImage*, vol. 100, pp. 590–607, 2014.
- [6] R. Hari and A. Puce, *MEG-EEG primer*. New York, NY: Oxford University Press, 2017.
- [7] H. McCann, G. Pisano, and L. Beltrachini, "Variation in Reported Human Head Tissue Electrical Conductivity Values," *Brain topography*, vol. 32, no. 5, pp. 825–858, 2019.
- [8] R. Hoekema, G. H. Wieneke, F. S. S. Leijten, C. W. M. van Veelen, P. C. van Rijen, G. J. M. Huiskamp, J. Ansems, and A. C. van Huffelen, "Measurement of the conductivity of skull, temporarily removed during epilepsy surgery," *Brain topography*, vol. 16, no. 1, pp. 29–38, 2003.
- [9] M. Akhtari, H. C. Bryant, A. N. Mamelak, E. R. Flynn, L. Heller, J. J. Shih, M. Mandelkern, A. Matlachov, D. M. Ranken, E. D. Best, M. A. DiMauro, R. R. Lee, and W. W. Sutherling, "Conductivities of three-layer live human skull," *Brain topography*, vol. 14, no. 3, pp. 151–167, 2002.
- [10] Z. Akalin Acar, C. E. Acar, and S. Makeig, "Simultaneous head tissue conductivity and EEG source location estimation," *NeuroImage*, vol. 124, pp. 168–180, 2016.
- [11] V. Montes-Restrepo, P. van Mierlo, G. Strobbe, S. Staelens, S. Vandenberghe, and H. Hallez, "Influence of skull modeling approaches on EEG source localization," *Brain topography*, vol. 27, no. 1, pp. 95–111, 2014.
- [12] C. Schmidt, S. Wagner, M. Burger, U. van Rienen, and C. H. Wolters, "Impact of uncertain head tissue conductivity in the optimization of transcranial direct current stimulation for an auditory target," *Journal of Neural Engineering*, vol. 12, no. 4, p. 046028, 2015.
- [13] J. Vorwerk, Ü. Aydın, C. H. Wolters, and C. R. Butson, "Influence of Head Tissue Conductivity Uncertainties on EEG Dipole Reconstruction," *Frontiers in Neuroscience*, vol. 13, p. 531, 2019.
- [14] S. Vallaghe and M. Clerc, "A Global Sensitivity Analysis of Three- and Four-Layer EEG Conductivity Models," *IEEE Transactions on Biomedical Engineering*, vol. 56, no. 4, pp. 988–995, 2009.
- [15] P. Kwan, A. Arzimanoglou, A. T. Berg, M. J. Brodie, W. Allen Hauser, G. Mathern, S. L. Moshé, E. Perucca, S. Wiebe, and J. French, "Definition of drug resistant epilepsy: consensus proposal by the ad hoc Task Force of the ILAE Commission on Therapeutic Strategies," *Epilepsia*, vol. 51, no. 6, pp. 1069–1077, 2010.
- [16] F. Rosenow and H. Lüders, "Presurgical evaluation of epilepsy," *Brain*, vol. 124, no. Pt 9, pp. 1683–1700, 2001.
- [17] H. O. Lüders, I. Najm, D. Nair, P. Widdess-Walsh, and W. Bingman, "The epileptogenic zone: general principles," *Epileptic disorders : international epilepsy journal with videotape*, vol. 8 Suppl 2, pp. S1–9, 2006.

- [18] Ü. Aydın, S. Rampp, A. Wollbrink, H. Kugel, J.-H. Cho, T. R. Knösche, C. Grova, J. Wellmer, and C. H. Wolters, "Zoomed MRI Guided by Combined EEG/MEG Source Analysis: A Multimodal Approach for Optimizing Presurgical Epilepsy Work-up and its Application in a Multi-focal Epilepsy Patient Case Study," *Brain topography*, vol. 30, no. 4, pp. 417–433, 2017.
- [19] C. Kellinghaus and H. O. Lüders, "Frontal lobe epilepsy," *Epileptic disorders : international epilepsy journal with videotape*, vol. 6, no. 4, pp. 223–239, 2004.
- [20] G. G. Regner, P. Pereira, D. T. Leffa, C. de Oliveira, R. Vercelino, F. Fregni, and I. L. S. Torres, "Preclinical to Clinical Translation of Studies of Transcranial Direct-Current Stimulation in the Treatment of Epilepsy: A Systematic Review," *Frontiers in Neuroscience*, vol. 12, p. 189, 2018.
- [21] D. Purves, G. J. Augustine, D. Fitzpatrick, W. C. Hall, A. S. Lamantia, R. D. Mooney, M. L. Platt, and L. E. White, eds., *Neuroscience*. New York: Oxford University Press, sixth edition ed., 2018.
- [22] C. G. Gross, *Neuroscience, Early History of.*, 1987.
- [23] L. Luo, *Principles of neurobiology*. New York: Garland Science, 2016.
- [24] G. Cruccu, M. J. Aminoff, G. Curio, J. M. Guerit, R. Kakigi, F. Mauguiere, P. M. Rossini, R.-D. Treede, and L. Garcia-Larrea, "Recommendations for the clinical use of somatosensory-evoked potentials," *Clinical neurophysiology : official journal of the International Federation of Clinical Neurophysiology*, vol. 119, no. 8, pp. 1705–1719, 2008.
- [25] A. Nakamura, T. Yamada, A. Goto, T. Kato, K. Ito, Y. Abe, T. Kachi, and R. Kakigi, "Somatosensory homunculus as drawn by MEG," *NeuroImage*, vol. 7, no. 4 Pt 1, pp. 377–386, 1998.
- [26] T. Allison, G. McCarthy, C. C. Wood, and S. J. Jones, "Potentials evoked in human and monkey cerebral cortex by stimulation of the median nerve. A review of scalp and intracranial recordings," *Brain*, vol. 114 (Pt 6), pp. 2465–2503, 1991.
- [27] H. Buchner, M. Fuchs, H. A. Wischmann, O. Dössel, I. Ludwig, A. Knepper, and P. Berg, "Source analysis of median nerve and finger stimulated somatosensory evoked potentials: multichannel simultaneous recording of electric and magnetic fields combined with 3D-MR tomography," *Brain topography*, vol. 6, no. 4, pp. 299–310, 1994.
- [28] M. Mertens and B. Lütkenhöner, "Efficient neuromagnetic determination of landmarks in the somatosensory cortex," *Clinical neurophysiology : official journal of the International Federation of Clinical Neurophysiology*, vol. 111, no. 8, pp. 1478–1487, 2000.
- [29] S. Lew, C. H. Wolters, A. Anwender, S. Makeig, and R. S. MacLeod, "Improved EEG source analysis using low-resolution conductivity estimation in a four-compartment finite element head model," *Human brain mapping*, vol. 30, no. 9, pp. 2862–2878, 2009.
- [30] H. Onishi, K. Sugawara, K. Yamashiro, D. Sato, M. Suzuki, H. Kirimoto, H. Tamaki, H. Murakami, and S. Kameyama, "Effect of the number of pins and inter-pin distance on somatosensory evoked magnetic fields following mechanical tactile stimulation," *Brain Research*, vol. 1535, pp. 78–88, 2013.
- [31] W. H. Organization, *Epilepsy: a public health imperative*. Geneva: World Health Organization, 2019.
- [32] M. Baulac, H. de Boer, C. Elger, M. Glynn, R. Kälviäinen, A. Little, J. Mifsud, E. Perucca, A. Pitkänen, and P. Ryvlin, "Epilepsy priorities in Europe: A report of the ILAE-IBE Epilepsy Advocacy Europe Task Force," *Epilepsia*, vol. 56, no. 11, pp. 1687–1695, 2015.
- [33] J. Bowman, F. E. Dudek, and M. Spitz, "Epilepsy," in *Encyclopedia of life sciences*, Chichester, England: Wiley, 2005.
- [34] E. H. Reynolds and M. R. Trimble, "Epilepsy, psychiatry, and neurology," *Epilepsia*, vol. 50 Suppl 3, pp. 50–55, 2009.
- [35] M.-C. Picot, A. Jausse, D. Neveu, P. Kahane, A. Crespel, P. Gelisse, E. Hirsch, P. Derambure, S. Dupont, E. Landré, F. Chassoux, L. Valton, J.-P. Vignal, C. Marchal, C. Lamy, F. Semah, A. Biraben, A. Arzimanoglou, J. Petit, P. Thomas, V. Macioce, P. Dujols, and P. Ryvlin, "Cost-effectiveness analysis of epilepsy surgery in a controlled cohort of adult patients with intractable partial epilepsy: A 5-year follow-up study," *Epilepsia*, vol. 57, no. 10, pp. 1669–1679, 2016.

- [36] S. West, S. J. Nolan, and R. Newton, "Surgery for epilepsy: a systematic review of current evidence," *Epileptic disorders : international epilepsy journal with videotape*, vol. 18, no. 2, pp. 113–121, 2016.
- [37] J. Wellmer, C. M. Quesada, L. Rothe, C. E. Elger, C. G. Bien, and H. Urbach, "Proposal for a magnetic resonance imaging protocol for the detection of epileptogenic lesions at early outpatient stages," *Epilepsia*, vol. 54, no. 11, pp. 1977–1987, 2013.
- [38] T. R. Henry, "Functional neuroimaging with positron emission tomography," *Epilepsia*, vol. 37, no. 12, pp. 1141–1154, 1996.
- [39] S. Rampp, H. Stefan, X. Wu, M. Kaltenhäuser, B. Maess, F. C. Schmitt, C. H. Wolters, H. Hamer, B. S. Kasper, S. Schwab, A. Doerfler, I. Blümcke, K. Rössler, and M. Buchfelder, "Magnetoencephalography for epileptic focus localization in a series of 1000 cases," *Brain*, vol. 142, no. 10, pp. 3059–3071, 2019.
- [40] C. Plummer, A. S. Harvey, and M. Cook, "EEG source localization in focal epilepsy: where are we now?," *Epilepsia*, vol. 49, no. 2, pp. 201–218, 2008.
- [41] L. Duez, H. Tankisi, P. O. Hansen, P. Sidenius, A. Sabers, L. H. Pinborg, M. Fabricius, G. Rásonyi, G. Rubboli, B. Pedersen, A.-M. Leffers, P. Uldall, B. Jespersen, J. Brennum, O. M. Henriksen, A. Fuglsang-Frederiksen, and S. Beniczky, "Electromagnetic source imaging in presurgical workup of patients with epilepsy: A prospective study," *Neurology*, vol. 92, no. 6, pp. e576–e586, 2019.
- [42] G. Dassios, A. S. Fokas, and D. Hadjiloizi, "On the complementarity of electroencephalography and magnetoencephalography," *Inverse Problems*, vol. 23, no. 6, pp. 2541–2549, 2007.
- [43] J. Haueisen, M. Funke, D. Güllmar, and R. Eichardt, "Tangential and radial epileptic spike activity: different sensitivity in EEG and MEG," *Journal of clinical neurophysiology : official publication of the American Electroencephalographic Society*, vol. 29, no. 4, pp. 327–332, 2012.
- [44] Ü. Aydın, J. Vorwerk, P. Küpper, M. Heers, H. Kugel, A. Galka, L. Hamid, J. Wellmer, C. Kellinghaus, S. Rampp, and C. H. Wolters, "Combining EEG and MEG for the Reconstruction of Epileptic Activity Using a Calibrated Realistic Volume Conductor Model," *PLoS ONE*, vol. 9, no. 3, p. e93154, 2014.
- [45] M. Iwasaki, E. Pestana, R. C. Burgess, H. O. Lüders, H. Shamoto, and N. Nakasato, "Detection of epileptiform activity by human interpreters: blinded comparison between electroencephalography and magnetoencephalography," *Epilepsia*, vol. 46, no. 1, pp. 59–68, 2005.
- [46] S. Knake, E. Halgren, H. Shiraishi, K. Hara, H. M. Hamer, P. E. Grant, V. A. Carr, D. Foxe, S. Camposano, E. Busa, T. Witzel, M. S. Hämäläinen, S. P. Ahlfors, E. B. Bromfield, P. M. Black, B. F. Bourgeois, A. J. Cole, G. R. Cosgrove, B. A. Dworetzky, J. R. Madsen, P. G. Larsson, D. L. Schomer, E. A. Thiele, A. M. Dale, B. R. Rosen, and S. M. Stuffelbeam, "The value of multichannel MEG and EEG in the presurgical evaluation of 70 epilepsy patients," *Epilepsy Research*, vol. 69, no. 1, pp. 80–86, 2006.
- [47] Ü. Aydın, J. Vorwerk, M. Dümpelmann, P. Küpper, H. Kugel, M. Heers, J. Wellmer, C. Kellinghaus, J. Haueisen, S. Rampp, H. Stefan, and C. H. Wolters, "Combined EEG/MEG can outperform single modality EEG or MEG source reconstruction in presurgical epilepsy diagnosis," *PLoS ONE*, vol. 10, no. 3, p. e0118753, 2015.
- [48] J. S. Ebersole and M. Wagner, "Relative Yield of MEG and EEG Spikes in Simultaneous Recordings," *Journal of clinical neurophysiology : official publication of the American Electroencephalographic Society*, vol. 35, no. 6, pp. 443–453, 2018.
- [49] C. H. Wolters, R. F. Beckmann, A. Rienäcker, and H. Buchner, "Comparing regularized and non-regularized nonlinear dipole fit methods: a study in a simulated sulcus structure," *Brain topography*, vol. 12, no. 1, pp. 3–18, 1999.
- [50] R. Plonsey and D. B. Heppner, "Considerations of quasi-stationarity in electrophysiological systems," *The Bulletin of mathematical biophysics*, vol. 29, no. 4, pp. 657–664, 1967.
- [51] C. H. Wolters, A. Anwänder, G. Berti, and U. Hartmann, "Geometry-adapted hexahedral meshes improve accuracy of finite-element-method-based EEG source analysis," *IEEE transactions on bio-*

- medical engineering*, vol. 54, no. 8, pp. 1446–1453, 2007.
- [52] J. C. de Munck, C. H. Wolters, and M. Clerc, “EEG and MEG: forward modeling,” in *Handbook of neural activity measurement* (R. Brette and A. Destexhe, eds.), pp. 192–256, Cambridge: Cambridge University Press, 2012.
- [53] E. Cuartas Morales, C. D. Acosta-Medina, G. Castellanos-Dominguez, and D. Mantini, “A Finite-Difference Solution for the EEG Forward Problem in Inhomogeneous Anisotropic Media,” *Brain topography*, vol. 32, no. 2, pp. 229–239, 2019.
- [54] C. H. Wolters, A. Anwander, X. Tricoche, D. Weinstein, M. A. Koch, and R. S. MacLeod, “Influence of tissue conductivity anisotropy on EEG/MEG field and return current computation in a realistic head model: A simulation and visualization study using high-resolution finite element modeling,” *NeuroImage*, vol. 30, no. 3, pp. 813–826, 2006.
- [55] S. Pursiainen, J. Vorwerk, and C. H. Wolters, “Electroencephalography (EEG) forward modeling via H(div) finite element sources with focal interpolation,” *Physics in medicine and biology*, vol. 61, no. 24, pp. 8502–8520, 2016.
- [56] S. Wagner, F. Lucka, J. Vorwerk, C. S. Herrmann, G. Nolte, M. Burger, and C. H. Wolters, “Using reciprocity for relating the simulation of transcranial current stimulation to the EEG forward problem,” *NeuroImage*, vol. 140, pp. 163–173, 2016.
- [57] C. H. Wolters, L. Grasedyck, and W. Hackbusch, “Efficient computation of lead field bases and influence matrix for the FEM-based EEG and MEG inverse problem,” *Inverse Problems*, vol. 20, no. 4, pp. 1099–1116, 2004.
- [58] C. H. Wolters, M. Kuhn, A. Anwander, and S. Reitzinger, “A parallel algebraic multigrid solver for finite element method based source localization in the human brain,” *Computing and Visualization in Science*, vol. 5, no. 3, pp. 165–177, 2002.
- [59] D. L. Camacho, R. H. Hopper, G. M. Lin, and B. S. Myers, “An improved method for finite element mesh generation of geometrically complex structures with application to the skullbase,” *Journal of Biomechanics*, vol. 30, no. 10, pp. 1067–1070, 1997.
- [60] F. Lucka, S. Pursiainen, M. Burger, and C. H. Wolters, “Hierarchical Bayesian inference for the EEG inverse problem using realistic FE head models: Depth localization and source separation for focal primary currents,” *NeuroImage*, vol. 61, no. 4, pp. 1364–1382, 2012.
- [61] C. M. Michel and B. He, “EEG source localization,” *Handbook of clinical neurology*, vol. 160, pp. 85–101, 2019.
- [62] J. C. Mosher, P. S. Lewis, and R. M. Leahy, “Multiple dipole modeling and localization from spatio-temporal MEG data,” *IEEE transactions on bio-medical engineering*, vol. 39, no. 6, pp. 541–557, 1992.
- [63] M. Huang, C. Aine, S. Supek, E. Best, D. Ranken, and E. Flynn, “Multi-start downhill simplex method for spatio-temporal source localization in magnetoencephalography,” *Electroencephalography and Clinical Neurophysiology/Evoked Potentials Section*, vol. 108, no. 1, pp. 32–44, 1998.
- [64] C. M. Michel, M. M. Murray, G. Lantz, S. Gonzalez, L. Spinelli, and R. Grave de Peralta, “EEG source imaging,” *Clinical neurophysiology : official journal of the International Federation of Clinical Neurophysiology*, vol. 115, no. 10, pp. 2195–2222, 2004.
- [65] J. C. Mosher and R. M. Leahy, “Recursive MUSIC: a framework for EEG and MEG source localization,” *IEEE transactions on bio-medical engineering*, vol. 45, no. 11, pp. 1342–1354, 1998.
- [66] F.-H. Lin, T. Witzel, S. P. Ahlfors, S. M. Stufflebeam, J. W. Belliveau, and M. S. Hämaläinen, “Assessing and improving the spatial accuracy in MEG source localization by depth-weighted minimum-norm estimates,” *NeuroImage*, vol. 31, no. 1, pp. 160–171, 2006.
- [67] R. D. Pascual-Marqui, C. M. Michel, and D. Lehmann, “Low resolution electromagnetic tomography: a new method for localizing electrical activity in the brain,” *International journal of psychophysiology : official journal of the International Organization of Psychophysiology*, vol. 18, no. 1, pp. 49–65, 1994.

- [68] R. D. Pascual-Marqui, "Standardized low-resolution brain electromagnetic tomography (sLORETA): technical details," *Methods and findings in experimental and clinical pharmacology*, vol. 24 Suppl D, pp. 5–12, 2002.
- [69] R. D. Pascual-Marqui, "Discrete, 3D distributed linear imaging methods of electric neuronal activity. Part 1: exact, zero error localization," *arXiv*, 2007.
- [70] K. Sekihara, S. S. Nagarajan, D. Poeppel, A. Marantz, and Y. Miyashita, "Reconstructing spatio-temporal activities of neural sources using an MEG vector beamformer technique," *IEEE transactions on bio-medical engineering*, vol. 48, no. 7, pp. 760–771, 2001.
- [71] J. Gross, J. Kujala, M. Hamalainen, L. Timmermann, A. Schnitzler, and R. Salmelin, "Dynamic imaging of coherent sources: Studying neural interactions in the human brain," *Proceedings of the National Academy of Sciences of the United States of America*, vol. 98, no. 2, pp. 694–699, 2001.
- [72] T. Bast, T. Boppel, A. Rupp, I. Harting, K. Hoehstetter, S. Fauser, A. Schulze-Bonhage, D. Rating, and M. Scherg, "Noninvasive source localization of interictal EEG spikes: effects of signal-to-noise ratio and averaging," *Journal of clinical neurophysiology : official publication of the American Electroencephalographic Society*, vol. 23, no. 6, pp. 487–497, 2006.
- [73] J. Haueisen, C. Ramon, M. Eiselt, H. Brauer, and H. Nowak, "Influence of tissue resistivities on neuromagnetic fields and electric potentials studied with a finite element model of the head," *IEEE transactions on bio-medical engineering*, vol. 44, no. 8, pp. 727–735, 1997.
- [74] D. S. Tuch, V. J. Wedeen, A. M. Dale, J. S. George, and J. W. Belliveau, "Conductivity tensor mapping of the human brain using diffusion tensor MRI," *Proceedings of the National Academy of Sciences of the United States of America*, vol. 98, no. 20, pp. 11697–11701, 2001.
- [75] L. Ruthotto, H. Kugel, J. Olesch, B. Fischer, J. Modersitzki, M. Burger, and C. H. Wolters, "Diffeomorphic susceptibility artifact correction of diffusion-weighted magnetic resonance images," *Physics in medicine and biology*, vol. 57, no. 18, pp. 5715–5731, 2012.
- [76] S. Lew, D. D. Sliva, M.-s. Choe, P. E. Grant, Y. Okada, C. H. Wolters, and M. S. Hämäläinen, "Effects of sutures and fontanels on MEG and EEG source analysis in a realistic infant head model," *NeuroImage*, vol. 76, pp. 282–293, 2013.
- [77] H. Azizollahi, A. Aarabi, and F. Wallois, "Effects of uncertainty in head tissue conductivity and complexity on EEG forward modeling in neonates," *Human Brain Mapping*, vol. 37, no. 10, pp. 3604–3622, 2016.
- [78] N. Lynnerup, J. G. Astrup, and B. Sejrsen, "Thickness of the human cranial diploe in relation to age, sex and general body build," *Head & Face Medicine*, vol. 1, no. 1, 2005.
- [79] M. Dannhauer, B. Lanfer, C. H. Wolters, and T. R. Knösche, "Modeling of the human skull in EEG source analysis," *Human Brain Mapping*, vol. 32, no. 9, pp. 1383–1399, 2011.
- [80] B. Lanfer, M. Scherg, M. Dannhauer, T. R. Knösche, M. Burger, and C. H. Wolters, "Influences of skull segmentation inaccuracies on EEG source analysis," *NeuroImage*, vol. 62, no. 1, pp. 418–431, 2012.
- [81] R. J. Sadleir, T. D. Vannorsdall, D. J. Schretlen, and B. Gordon, "Target Optimization in Transcranial Direct Current Stimulation," *Frontiers in Psychiatry*, vol. 3, 2012.
- [82] M. Fernández-Corazza, S. Turovets, P. Luu, N. Price, C. H. Muravchik, and D. Tucker, "Skull Modeling Effects in Conductivity Estimates Using Parametric Electrical Impedance Tomography," *IEEE transactions on bio-medical engineering*, vol. 65, no. 8, pp. 1785–1797, 2018.
- [83] S. I. Goncalves, J. C. de Munck, J. Verbunt, F. Bijma, R. M. Heethaar, and F. Lopes da Silva, "In vivo measurement of the brain and skull resistivities using an eit-based method and realistic models for the head," *IEEE Transactions on Biomedical Engineering*, vol. 50, no. 6, pp. 754–767, 2003.
- [84] N. Gao, S. A. Zhu, and B. He, "A new magnetic resonance electrical impedance tomography (MREIT) algorithm: the RSM-MREIT algorithm with applications to estimation of human head conductivity," *Physics in Medicine and Biology*, vol. 51, no. 12, pp. 3067–3083, 2006.
- [85] X. Li, K. Yu, and B. He, "Magnetoacoustic tomography with magnetic induction (MAT-MI) for

- imaging electrical conductivity of biological tissue: a tutorial review," *Physics in medicine and biology*, vol. 61, no. 18, pp. R249–R270, 2016.
- [86] C. H. Wolters, S. Lew, R. S. MacLeod, and M. S. Hämäläinen, "Combined EEG/MEG source analysis using calibrated finite element head models," *Biomedical Technology*, vol. 55, no. (Suppl.1), pp. 64–67, 2010.
- [87] C. Tang, F. You, G. Cheng, D. Gao, F. Fu, G. Yang, and X. Dong, "Correlation Between Structure and Resistivity Variations of the Live Human Skull," *IEEE Transactions on Biomedical Engineering*, vol. 55, no. 9, pp. 2286–2292, 2008.
- [88] K. Wendel, J. Väisänen, G. Seemann, J. Hyttinen, and J. Malmivuo, "The Influence of Age and Skull Conductivity on Surface and Subdermal Bipolar EEG Leads," *Computational Intelligence and Neuroscience*, vol. 2010, no. 2, pp. 1–7, 2010.
- [89] H. Azizollahi, M. Darbas, M. M. Diallo, A. El Badia, and S. Lohrengel, "EEG in neonates: Forward modeling and sensitivity analysis with respect to variations of the conductivity," *Mathematical Biosciences & Engineering*, vol. 15, no. 4, pp. 905–932, 2018.
- [90] E. M. E. Arumugam, S. Turovets, N. Price, D. Rech, P. Luu, and D. M. Tucker, eds., *In vivo estimation of scalp and skull conductivity using bEIT for non-invasive neuroimaging and stimulation*, 2017.
- [91] H. H. de Boer, A. E. van der Merwe, and V. Soerdjbalie-Maikoe, "Human cranial vault thickness in a contemporary sample of 1097 autopsy cases: relation to body weight, stature, age, sex and ancestry," *International Journal of Legal Medicine*, vol. 130, no. 5, pp. 1371–1377, 2016.
- [92] E. M. Lillie, J. E. Urban, S. K. Lynch, A. A. Weaver, and J. D. Stitzel, "Evaluation of Skull Cortical Thickness Changes With Age and Sex From Computed Tomography Scans," *Journal of Bone and Mineral Research*, vol. 31, no. 2, pp. 299–307, 2016.
- [93] M. Pellegrini, M. Zoghi, and S. Jaberzadeh, "Biological and anatomical factors influencing interindividual variability to noninvasive brain stimulation of the primary motor cortex: a systematic review and meta-analysis," *Reviews in the neurosciences*, vol. 29, no. 2, pp. 199–222, 2018.
- [94] P. L. Nunez and R. Srinivasan, *Electric fields of the brain: The neurophysics of EEG*. Oxford: Oxford Univ. Press, 2. ed. ed., 2006.
- [95] J. Pernier, F. Perrin, and O. Bertrand, "Scalp current density fields: concept and properties," *Electroencephalography and clinical neurophysiology*, vol. 69, no. 4, pp. 385–389, 1988.
- [96] S. B. Baumann, D. R. Wozny, S. K. Kelly, and F. M. Meno, "The electrical conductivity of human cerebrospinal fluid at body temperature," *IEEE Transactions on Biomedical Engineering*, vol. 44, no. 3, pp. 220–223, 1997.
- [97] M. Antonakakis, S. Schrader, A. Wollbrink, R. Oostenfeld, S. Rampp, J. Haueisen, and C. H. Wolters, "The effect of stimulation type, head modeling, and combined EEG and MEG on the source reconstruction of the somatosensory P20/N20 component," *Human Brain Mapping*, vol. 40, no. 17, pp. 5011–5028, 2019.
- [98] K. A. Salayev, N. Nakasato, M. Ishitobi, H. Shamoto, A. Kanno, and K. Iinuma, "Spike orientation may predict epileptogenic side across cerebral sulci containing the estimated equivalent dipole," *Clinical neurophysiology : official journal of the International Federation of Clinical Neurophysiology*, vol. 117, no. 8, pp. 1836–1843, 2006.
- [99] M. Rullmann, A. Anwander, M. Dannhauer, S. K. Warfield, F. H. Duffy, and C. H. Wolters, "EEG source analysis of epileptiform activity using a 1 mm anisotropic hexahedra finite element head model," *NeuroImage*, vol. 44, no. 2, pp. 399–410, 2009.
- [100] R. W. Brown, Y.-C. N. Cheng, E. M. Haacke, M. R. Thompson, and R. Venkatesan, *Magnetic resonance imaging: Physical principles and sequence design*. Hoboken, New Jersey: John Wiley & Sons, Inc, second edition ed., 2014.
- [101] M. A. Nitsche and W. Paulus, "Excitability changes induced in the human motor cortex by weak transcranial direct current stimulation," *The Journal of physiology*, vol. 527 Pt 3, pp. 633–639, 2000.

- [102] A. Baltus, S. Wagner, C. H. Wolters, and C. S. Herrmann, "Optimized auditory transcranial alternating current stimulation improves individual auditory temporal resolution," *Brain stimulation*, vol. 11, no. 1, pp. 118–124, 2018.
- [103] J. P. Dmochowski, A. Datta, M. Bikson, Y. Su, and L. C. Parra, "Optimized multi-electrode stimulation increases focality and intensity at target," *Journal of Neural Engineering*, vol. 8, no. 4, p. 046011, 2011.
- [104] S. Wagner, S. M. Rampersad, Ü. Aydin, J. Vorwerk, T. F. Oostendorp, T. Neuling, C. S. Herrmann, D. F. Stegeman, and C. H. Wolters, "Investigation of tDCS volume conduction effects in a highly realistic head model," *Journal of Neural Engineering*, vol. 11, no. 1, p. 016002, 2014.
- [105] F. H. Kasten, K. Duecker, M. C. Maack, A. Meiser, and C. S. Herrmann, "Integrating electric field modeling and neuroimaging to explain inter-individual variability of tACS effects," *Nature communications*, vol. 10, no. 1, p. 5427, 2019.
- [106] J. P. Dmochowski, L. Koessler, A. M. Norcia, M. Bikson, and L. C. Parra, "Optimal use of EEG recordings to target active brain areas with transcranial electrical stimulation," *NeuroImage*, vol. 157, pp. 69–80, 2017.
- [107] A. Antal, I. Alekseichuk, and M. e. a. Bikson, "Low intensity transcranial electric stimulation: Safety, ethical, legal regulatory and application guidelines," *Clinical neurophysiology : official journal of the International Federation of Clinical Neurophysiology*, vol. 128, no. 9, pp. 1774–1809, 2017.
- [108] G. B. Saturnino, H. R. Siebner, A. Thielscher, and K. H. Madsen, "Accessibility of cortical regions to focal TES: Dependence on spatial position, safety, and practical constraints," *NeuroImage*, vol. 203, p. 116183, 2019.
- [109] J. K. Rice, C. Rorden, J. S. Little, and L. C. Parra, "Subject position affects EEG magnitudes," *NeuroImage*, vol. 64, pp. 476–484, 2013.
- [110] R. Oostenveld, P. Fries, E. Maris, and J.-M. Schoffelen, "FieldTrip: Open source software for advanced analysis of MEG, EEG, and invasive electrophysiological data," *Computational intelligence and neuroscience*, vol. 2011, p. 156869, 2011.
- [111] N. Otsu, "A Threshold Selection Method from Gray-Level Histograms," *IEEE Transactions on Systems, Man, and Cybernetics*, vol. 9, no. 1, pp. 62–66, 1979.
- [112] C. Ramon, P. H. Schimpf, and J. Haueisen, "Effect of model complexity on EEG source localizations," *Neurology & clinical neurophysiology : NCV*, vol. 2004, p. 81, 2004.
- [113] S. Homma, T. Musha, Y. Nakajima, Y. Okamoto, S. Blom, R. Flink, and K. E. Hagbarth, "Conductivity ratios of the scalp-skull-brain head model in estimating equivalent dipole sources in human brain," *Neuroscience research*, vol. 22, no. 1, pp. 51–55, 1995.
- [114] T. R. Knösche, *Solutions of the neuroelectromagnetic inverse problem: An evaluation study*. [S.l.: s.n.], 1997.
- [115] R. Hari, J. Karhu, M. Hämäläinen, J. Knuutila, O. Salonen, M. Sams, and V. Vilkmán, "Functional organization of the human first and second somatosensory cortices: a neuromagnetic study," *The European journal of neuroscience*, vol. 5, no. 6, pp. 724–734, 1993.
- [116] S. Pursiainen, A. Sorrentino, C. Campi, and M. Piana, "Forward simulation and inverse dipole localization with the lowest order Raviart–Thomas elements for electroencephalography," *Inverse Problems*, vol. 27, no. 4, p. 045003, 2011.
- [117] T. Medani, D. Lautru, D. Schwartz, Z. Ren, and G. Sou, "Fem Method for the EEG Forward Problem and Improvement based on Modification of the Saint Venant's Method," *Progress In Electromagnetics Research*, vol. 153, pp. 11–22, 2015.
- [118] L. Beltrachini, "Sensitivity of the Projected Subtraction Approach to Mesh Degeneracies and Its Impact on the Forward Problem in EEG," *IEEE Transactions on Biomedical Engineering*, vol. 66, no. 1, pp. 273–282, 2019.
- [119] M. Bauer, S. Pursiainen, J. Vorwerk, H. Kostler, and C. H. Wolters, "Comparison Study for Whitney (Raviart–Thomas)-Type Source Models in Finite-Element-Method-Based EEG Forward Modeling,"

- IEEE Transactions on Biomedical Engineering*, vol. 62, no. 11, pp. 2648–2656, 2015.
- [120] J. Vorwerk, R. Oostenveld, M. C. Piastra, L. Magyari, and C. H. Wolters, “The FieldTrip-SimBio pipeline for EEG forward solutions,” *BioMedical Engineering OnLine*, vol. 17, no. 1, p. 37, 2018.
- [121] S. Lew, C. H. Wolters, T. Dierkes, C. Röer, and R. S. MacLeod, “Accuracy and run-time comparison for different potential approaches and iterative solvers in finite element method based EEG source analysis,” *Applied numerical mathematics : transactions of IMACS*, vol. 59, no. 8, pp. 1970–1988, 2009.
- [122] C. H. Wolters, *Influence of tissue conductivity inhomogeneity and anisotropy on EEG/MEG based source localization in the human brain: Zugl.: Leipzig, Univ., Diss., 2003*, vol. 39 of *MPI series in cognitive neuroscience*. Leipzig: Max-Planck-Inst. of Cognitive Neuroscience, 2003.
- [123] A. Khan, M. Antonakakis, N. Vagenauer, A. Wollbrink, S. Suntrup-Krueger, R. T. Schneider, S. H. Herrmann, Nitsche. M., P. Walter, J. Haueisen, and C. H. Wolters, eds., *Constrained maximum intensity optimized multi-electrode tDCS targeting of human somatosensory network*, 2019.
- [124] N. G. Gençer and C. E. Acar, “Sensitivity of EEG and MEG measurements to tissue conductivity,” *Inverse Problems*, vol. 49, no. 5, pp. 701–717, 2004.
- [125] D. Güllmar, J. Haueisen, and J. R. Reichenbach, “Influence of anisotropic electrical conductivity in white matter tissue on the EEG/MEG forward and inverse solution. A high-resolution whole head simulation study,” *NeuroImage*, vol. 51, no. 1, pp. 145–163, 2010.
- [126] J. C. de Munck, B. W. van Dijk, and H. Spekreijse, “Mathematical dipoles are adequate to describe realistic generators of human brain activity,” *IEEE transactions on bio-medical engineering*, vol. 35, no. 11, pp. 960–966, 1988.
- [127] S. Wagner, M. Burger, and C. H. Wolters, “An Optimization Approach for Well-Targeted Transcranial Direct Current Stimulation,” *SIAM Journal on Applied Mathematics*, vol. 76, no. 6, pp. 2154–2174, 2016.
- [128] C. R. Pernet, R. Wilcox, and G. A. Rousselet, “Robust Correlation Analyses: False Positive and Power Validation Using a New Open Source Matlab Toolbox,” *Frontiers in Psychology*, vol. 3, 2013.
- [129] Y. Benjamini and Y. Hochberg, “Controlling the False Discovery Rate: A Practical and Powerful Approach to Multiple Testing,” *Journal of the Royal Statistical Society. Series B (Methodological)*, vol. 57, no. 1, pp. 289–300, 1995.
- [130] F. J. Massey, “The Kolmogorov-Smirnov Test for Goodness of Fit,” *Journal American Statistical Association*, vol. 46, no. (253), pp. 68–78, 1951.
- [131] H. B. Mann and D. R. Whitney, “On a Test of Whether one of Two Random Variables is Stochastically Larger than the Other,” *The Annals of Mathematical Statistics*, vol. 18, no. 1, pp. 50–60, 1947.
- [132] G. B. Saturnino, A. Thielscher, K. H. Madsen, T. R. Knösche, and K. Weise, “A principled approach to conductivity uncertainty analysis in electric field calculations,” *NeuroImage*, vol. 188, pp. 821–834, 2019.
- [133] C. Gabriel, S. Gabriel, and E. Corthout, “The dielectric properties of biological tissues: I. Literature survey,” *Inverse Problems*, vol. 41, no. 11, pp. 2231–2249, 1996.
- [134] J. G. Stinstra and M. J. Peters, “The volume conductor may act as a temporal filter on the ECG and EEG,” *Medical & Biological Engineering & Computing*, vol. 36, no. 6, pp. 711–716, 1998.
- [135] U. u. Baysal and J. Haueisen, “Use of a priori information in estimating tissue resistivities—application to human data in vivo,” *Physiological Measurement*, vol. 25, no. 3, pp. 737–748, 2004.
- [136] D. M. Goldenholz, S. P. Ahlfors, M. S. Hämäläinen, D. Sharon, M. Ishitobi, L. M. Vaina, and S. M. Stuffelbeam, “Mapping the signal-to-noise-ratios of cortical sources in magnetoencephalography and electroencephalography,” *Human Brain Mapping*, vol. 30, no. 4, pp. 1077–1086, 2009.
- [137] T. Götz, R. Huonker, O. W. Witte, and J. Haueisen, “Thalamocortical Impulse Propagation and Information Transfer in EEG and MEG,” *Journal of Clinical Neurophysiology*, vol. 31, no. 3, pp. 253–260, 2014.
- [138] A. Peyman, S. J. Holden, S. Watts, R. Perrott, and C. Gabriel, “Dielectric properties of porcine

- cerebrospinal tissues at microwave frequencies: in vivo , in vitro and systematic variation with age," *Inverse Problems*, vol. 52, no. 8, pp. 2229–2245, 2007.
- [139] H. Delye, T. Clijmans, M. Y. Mommaerts, J. V. Sloten, and J. Goffin, "Creating a normative database of age-specific 3D geometrical data, bone density, and bone thickness of the developing skull: a pilot study," *Journal of Neurosurgery: Pediatrics*, vol. 16, no. 6, pp. 687–702, 2015.
- [140] T. J. Aspray and T. R. Hill, "Osteoporosis and the Ageing Skeleton," *Sub-cellular biochemistry*, vol. 91, pp. 453–476, 2019.
- [141] E. R. Sowell, B. S. Peterson, E. Kan, R. P. Woods, J. Yoshii, R. Bansal, D. Xu, H. Zhu, P. M. Thompson, and A. W. Toga, "Sex differences in cortical thickness mapped in 176 healthy individuals between 7 and 87 years of age," *Cerebral cortex (New York, N.Y. : 1991)*, vol. 17, no. 7, pp. 1550–1560, 2007.
- [142] A. Fjell, K. Walhovd, C. Fennema-Notestine, L. McEvoy, D. Hagler, D. Holland, K. Blennow, J. Brewer, A. Dale, and A. D. N. Initiative, "Brain atrophy in healthy aging is related to CSF levels of $A\beta_{1-42}$," *Cerebral cortex*, vol. 20, no. 9, pp. 2069–2079, 2010.
- [143] T. Allison, C. C. Wood, and W. R. Goff, "Brain stem auditory, pattern-reversal visual, and short-latency somatosensory evoked potentials: latencies in relation to age, sex, and brain and body size," *Electroencephalography and clinical neurophysiology*, vol. 55, no. 6, pp. 619–636, 1983.
- [144] J. Huttunen, H. Tolvanen, E. Heinonen, J. Voipio, H. Wikström, R. J. Ilmoniemi, R. Hari, and K. Kaila, "Effects of voluntary hyperventilation on cortical sensory responses," *Experimental brain research*, vol. 125, no. 3, pp. 248–254, 1999.
- [145] C. Engwer, J. Vorwerk, J. Ludewig, and C. H. Wolters, "A Discontinuous Galerkin Method to Solve the EEG Forward Problem Using the Subtraction Approach," *SIAM Journal on Scientific Computing*, vol. 39, no. 1, pp. B138–B164, 2017.
- [146] M. C. Piastra, A. Nüßing, J. Vorwerk, H. Bornfleth, R. Oostenveld, C. Engwer, and C. H. Wolters, "The Discontinuous Galerkin Finite Element Method for Solving the MEG and the Combined MEG/EEG Forward Problem," *Frontiers in Neuroscience*, vol. 12, p. 30, 2018.
- [147] A. Nussing, C. H. Wolters, H. Brinck, and C. Engwer, "The Unfitted Discontinuous Galerkin Method for Solving the EEG Forward Problem," *IEEE Transactions on Biomedical Engineering*, vol. 63, no. 12, pp. 2564–2575, 2016.
- [148] C. Ramon, P. Garguilo, E. A. Fridgeirsson, and J. Haueisen, "Changes in scalp potentials and spatial smoothing effects of inclusion of dura layer in human head models for EEG simulations," *Frontiers in Neuroengineering*, vol. 7, p. 1383, 2014.
- [149] L. Fiederer, J. Vorwerk, F. Lucka, M. Dannhauer, S. Yang, M. Dümpelmann, A. Schulze-Bonhage, A. Aertsen, O. Speck, C. H. Wolters, and T. Ball, "The role of blood vessels in high-resolution volume conductor head modeling of EEG," *NeuroImage*, vol. 128, pp. 193–208, 2016.
- [150] H.-J. Huppertz, C. Grimm, S. Fauser, J. Kassubek, I. Mader, A. Hochmuth, J. Spreer, and A. Schulze-Bonhage, "Enhanced visualization of blurred gray-white matter junctions in focal cortical dysplasia by voxel-based 3D MRI analysis," *Epilepsy Research*, vol. 67, no. 1-2, pp. 35–50, 2005.
- [151] R. Köhling, J. M. Höhling, H. Straub, D. Kuhlmann, U. Kuhnt, I. Tuxhorn, A. Ebner, P. Wolf, H. W. Pannek, A. Gorji, and E. J. Speckmann, "Optical monitoring of neuronal activity during spontaneous sharp waves in chronically epileptic human neocortical tissue," *Journal of neurophysiology*, vol. 84, no. 4, pp. 2161–2165, 2000.
- [152] C. Plummer, S. J. Vogrin, W. P. Woods, M. A. Murphy, M. J. Cook, and D. T. J. Liley, "Interictal and ictal source localization for epilepsy surgery using high-density EEG with MEG: a prospective long-term study," *Brain*, vol. 142, no. 4, pp. 932–951, 2019.
- [153] S. Lau, D. Güllmar, L. Flemming, D. B. Grayden, M. J. Cook, C. H. Wolters, and J. Haueisen, "Skull Defects in Finite Element Head Models for Source Reconstruction from Magnetoencephalography Signals," *Frontiers in Neuroscience*, vol. 10, p. 151, 2016.

-
- [154] Y. Huang, A. A. Liu, B. Lafon, D. Friedman, M. Dayan, X. Wang, M. Bikson, W. K. Doyle, O. Devinsky, and L. C. Parra, "Measurements and models of electric fields in the in vivo human brain during transcranial electric stimulation," *eLife*, vol. 6, p. 258, 2017.
- [155] V. S. Dimakopoulos, M. Antonakakis, G. Moeddel, J. Wellmer, S. Rampp, M. Zervakis, and C. H. Wolters, "Combined EEG/MEG Source Reconstruction of Epileptic Activity using a Two-Phase Spike Clustering Approach," in *2019 IEEE 19th International Conference on Bioinformatics and Bioengineering*, (Los Alamitos, CA), pp. 877–881, IEEE Computer Society, Conference Publishing Services, 2019.
- [156] M. Antonakakis, G. Giannakakis, M. Tsiknakis, S. Micheloyannis, and M. Zervakis, "Synchronization coupling investigation using ICA cluster analysis in resting MEG signals in reading difficulties," in *IEEE 13th International Conference on Bioinformatics and Bioengineering (BIBE), 2013*, (Piscataway, NJ), pp. 1–5, IEEE, 2013.
- [157] G. Lantz, L. Spinelli, M. Seeck, R. G. de Peralta Menendez, C. C. Sottas, and C. M. Michel, "Propagation of interictal epileptiform activity can lead to erroneous source localizations: a 128-channel EEG mapping study," *Journal of clinical neurophysiology : official publication of the American Electroencephalographic Society*, vol. 20, no. 5, pp. 311–319, 2003.
- [158] A. Nussing, M. C. Piastra, S. Schrader, M. Miinalainen, S. Pursiainen, H. Brinck, C. H. Wolters, and C. Engwer, "duneuro - A software toolbox for forward modeling in neuroscience," *arXiv*, p. 1901.02874, 2019.

Scientific Contributions

Journal Publications

1. **Antonakakis, M.**, Schrader, S., Wollbrink, A., Oostenfeld, R., Rampp, S., Haueisen, J., Wolters, C.H. (2019). The effect of stimulation type, head modeling, and combined EEG and MEG on the source reconstruction of the somatosensory P20/N20 component. *Human Brain Mapping*, 1-18. <https://doi.org/10.1002/hbm.24754>.
2. **Antonakakis, M.**, Schrader, S., Aydin, Ü., Khan, A., Gross, J., Zervakis, M., Rampp, S., Wolters, C.H. (2020). The effect of stimulation type, head modeling, and combined EEG and MEG on the source reconstruction of the somatosensory P20/N20 component. *Neuroimage*, 223. <https://doi.org/10.1016/j.neuroimage.2020.117353>.
3. Rezaei, A., **Antonakakis, M.**, Piastra, M.C., Wolters, C. H., Pursiainen, S. (2020). Parametrizing the Conditionally Gaussian Prior Model for Source Localization with Reference to the P20-N20 Component of Median Nerve SEP/SEF. *Brain Sciences*, 10(934). <https://doi.org/10.3390/brainsci10120934>.
4. Schrader, S., **Antonakakis, M.**, Rampp, S., Engwer, C., and Wolters, C.H. (2020). A novel method for calibrating head models to account for variability in conductivity and its evaluation in a sphere model. *Physics in Medicine and Biology*, 65(24). <https://doi.org/10.1088/1361-6560/abc5aa>.
5. Rezaei, A., **Antonakakis, M.**, Piastra, M.C., Alexandra Koulouri, Wolters, C. H., Pursiainen, S. (2021). Reconstructing Sequential Sub-Cortical and Cortical Median Nerve SEP Activity via the RAMUS Technique using Experimental Data. *NeuroImage (Under revision)*.
6. Khan, A., **Antonakakis, M.**, Vogenauer, N., Haueisen, J., Wolters, C.H. (2021). Constrained maximum intensity multi-channel tDCS optimization for an individualized stimulation of the somatosensory cortex. *Journal of Neuronal Engineering (Under revision)*.

Peer-reviewed proceedings

1. **Antonakakis, M.**, Schrader, S., Haueisen, J. and Wolters, C.H. (2017). Combined EEG/MEG source reconstruction of electric, hapto-tactile and pneumato-tactile somatosensory stimulation using realistic head volume conductor modelling. *International Conference on Basic and Clinical Multimodal Imaging*.
2. **Antonakakis, M.**, Schrader, S., Khan, A., Haueisen, J., Oostenveld, R., Wolters, C.H. (2018). Age-related skull conductivity determined by a calibration procedure using com-

- bined somatosensory evoked potentials and fields and a realistic head model. Biosignale, Erfurt, Germany.
3. **Antonakakis, M.**, Wollbrink, A., Khan, A., Zervakis, M., Paulus, W., Nitsche, M., Lencer, R., Suntrup-Krueger, S., Schneider, T., Herrmann, C.S. Haueisen, J., Wolters, C.H. (2019). Individual targeting and optimization of multi-channel transcranial electric stimulation of the human primary somatosensory cortex. 41th Annual International Conference of the IEEE Engineering in Medicine and Biology Society, Berlin, Germany.
 4. Khan, A., **Antonakakis, M.**, Vogenauer, N., Wollbrink, A., Suntrup-Krueger, S., Schneider, T.R., Herrmann, C.H., Nitsche, M., Paulus, W., Haueisen, J., Wolters, C.H. (2019). Constrained maximum intensity optimized multi-electrode tDCS targeting of human somatosensory network. 41th Annual International Conference of the IEEE Engineering in Medicine and Biology Society, Berlin, Germany.
 5. **Antonakakis, M.**, Rampp, S., Kellinghaus, C., Wolters, C.H., Moeddel, G. (2019). Individualized targeting and optimization of multi-channel transcranial direct current stimulation in drug-resistant epilepsy. 19th International Conference of the IEEE in Bioinformatics and Bioengineering, Athens, Greece.
 6. Politof, K., **Antonakakis, M.**, Wollbrink, A., Zervakis, M., Wolters, C.H. (2019). Effective Connectivity in the Primary Somatosensory Network using Combined EEG and MEG. 19th International Conference of the IEEE in Bioinformatics and Bioengineering, Athens, Greece.
 7. Dimakopoulos, V.S., **Antonakakis, M.**, Moeddel, G., Wellmer, J., Rampp, S., Zervakis, M., Wolters, C.H. (2019). Combined EEG/MEG Source Reconstruction of Epileptic Activity using a Two-Phase Spike Clustering Approach. 19th International Conference of the IEEE in Bioinformatics and Bioengineering, Athens, Greece.
 8. Khan, A., **Antonakakis, M.**, Schneider, T. R., Carsten, H. W. (2020). P120 Combined EEG/MEG targeting and multi-electrode individually optimized tDCS stimulation of the human somatosensory network. *Clinical Neurophysiology* 131(4):e79-e80.
 9. Dimakopoulos, V., **Antonakakis, M.**, Wolters, C. H., Zervakis, M. (2020). P69 Combined EEG & MEG Source Analysis coupled with a Two - Phase Spike Clustering Approach: A multifocal epilepsy case. *Clinical Neurophysiology* 131(4):e212-e213.
 10. Sdoukopoulou, G., **Antonakakis, M.**, Wolters, C. H., and Zervakis, M. (2020). Preprocessing Techniques on Combined EEG and MEG Data of a Drug-Resistant Epilepsy Case. Society of Applied Neuroscience (SAN2020), Thessaloniki, Greece.

Invited talks

1. Multimodal analysis of combined EEG/MEG using priors from MRI. Centre for Interdisciplinary Brain Research (CIBR), Jyväskylä, Finland (2017).

2. Brain Source Reconstruction of Epileptic Activity Using Combined EEG and MEG on a Calibrated Realistic Head Model. Scientific Symposium: From the desk for epilepsy surgery: New source localization methods in clinical practice. Deutschen Gesellschaft für Epileptologie, Fürth, Germany (2018).
3. Connectivity analysis in epilepsy networks using combined EEG/MEG source analysis and zoomed MRI. Scientific Workshop: Connectivity analysis in epilepsy. Summer School on Imaging in Epilepsy, Epilepsy Surgery and Epilepsy Research, Bochum, Germany (2018).
4. Combined EEG/MEG source analysis for presurgical epilepsy diagnosis using calibrated realistic volume conductor model. Scientific Symposium: Advanced MEG/EEG source analysis in epilepsy. 21st International Conference on Biomagnetism (Biomag2018), Philadelphia, Pennsylvania, USA (2018).
5. Combined EEG / MEG to individualize head modeling and its application to presurgical epilepsy diagnosis. Scientific Symposium on EEG and MEG source analysis methods. Summer School on Imaging in Epilepsy, Epilepsy Surgery and Epilepsy Research, Bochum, Germany (2019).
6. Individual targeting effects and optimization of multi-channel transcranial electric stimulation of the human primary somatosensory cortex. Scientific Workshop: New methods and experimental results for optimized multi-channel TES. International Conference on Complex Medical Engineering, Dortmund, Germany (2019). **Prized as best presentation with Young investigator award.**
7. Individualized targeting and multi-channel transcranial stimulation in epileptology. Scientific Symposium on E/MSI in Epileptology. Virtual Summer School on Imaging in Epilepsy, Epilepsy Surgery and Epilepsy Research, Bochum, Germany (2020).

Organized Workshops

1. Piastra, M.C., **Antonakakis, M.**, Homoelle, S. (2017). FieldTrip workshop, Pre-conference training courses at the BACI2017 conference in Bern, Switzerland.
2. Giannakakis, G., and **Antonakakis, M.** (2019). Spatiotemporal computational neuroimaging methods (EEG, MEG, MRI, etc) in epilepsy. 19th International Conference of the IEEE in Bioinformatics and Bioengineering, Athens, Greece.

Poster presentations on conferences

1. **Antonakakis, M.**, Oostenveld, R., Wellmer, J., Moeddel, G., Haueisen, J., Rampp, S., Wolters, C.H. (2018). Age-related skull conductivity estimated by a calibration procedure using combined somatosensory evoked potentials and fields on realistic head models. 50 years of MEG, Poros, Greece. **Prized as best poster (3rd place).**

2. **Antonakakis, M.**, Wollbrink, A., Khan, A., Zervakis, M., Paulus, W., Nitsche, M., Lencer, R., Suntrup-Krueger, S., Haueisen, J., Wolters, C.H. (2018). Individual targeting and optimization of multi-channel transcranial electric stimulation of the human primary somatosensory cortex. 21st International Conference on Biomagnetism (Biomag2018), Philadelphia, Pennsylvania, USA.
3. **Antonakakis, M.**, Rampp, S., Wellmer, J., Wolters, C.H. (2019). Combined EEG/MEG Connectivity Analysis in presurgical epilepsy diagnosis. Summer School on Imaging in Epilepsy, Epilepsy Surgery and Epilepsy Research, Bochum, Germany.

Erklärung

Ich versichere, dass ich die vorliegende Arbeit ohne unzulässige Hilfe Dritter und ohne Benutzung anderer als der angegebenen Hilfsmittel angefertigt habe. Die aus anderen Quellen direkt oder indirekt übernommenen Daten und Konzepte sind unter Angabe der Quelle gekennzeichnet.

Weitere Personen waren an der inhaltlich-materiellen Erstellung der vorliegenden Arbeit nicht beteiligt. Insbesondere habe ich hierfür nicht die entgeltliche Hilfe von Vermittlungs- bzw. Beratungsdiensten (Promotionsberater oder anderer Personen) in Anspruch genommen. Niemand hat von mir unmittelbar oder mittelbar geldwerte Leistungen für Arbeiten erhalten, die im Zusammenhang mit dem Inhalt der vorgelegten Dissertation stehen.

Die Arbeit wurde bisher weder im In- noch im Ausland in gleicher oder ähnlicher Form einer Prüfungsbehörde vorgelegt.

Ich bin darauf hingewiesen worden, dass die Unrichtigkeit der vorstehenden Erklärung als Täuschungsversuch bewertet wird und gemäß § 7 Abs. 10 der Promotionsordnung den Abbruch des Promotionsverfahrens zur Folge hat.

Ilmenau, den 07/04/2021

Marios Antonakakis